DOT/FAA/TC-24/5

Federal Aviation Administration
William J. Hughes Technical Center
Aviation Research Division
Atlantic City International Airport
New Jersey 08405

Investigating the Potential to Use Phase Change Materials to Store Heat in Concrete Pavement to Reduce the Need for Anti-Icing

March 2024

Final Report

U.S. Department of Transportation
Federal Aviation Administration

NOTICE

Technical Report Documentation Page

1. Report No.	2. Government Accession No.	3. Recipient's Catalog No.
DOT/FAA/TC-24/5		

4. Title and Subtitle	5. Report Date
INVESTIGATING THE POTENTIAL TO USE PHASE CHANGE MATERIALS TO STORE HEAT IN CONCRETE PAVEMENT TO REDUCE THE NEED FOR ANTI-ICING	March 2024
	6. Performing Organization Code

7. Author(s)	8. Performing Organization Report No.
Y. Farnam, H. S. Esmaeeli, L. Liston, M Krafcik, P. Zavattieri, B. Tao, K. Erk, J. Haddock, and J. Weiss	

9. Performing Organization Name and Address	10. Work Unit No. (TRAIS)
Purdue University – Lyles School of Civil Engineering 550 W Stadium Ave West Lafayette, IN 47907	
	11. Contract or Grant No. PEGASAS—Project No. 1: Heated Airport Pavement

12. Sponsoring Agency Name and Address	13. Type of Report and Period Covered
Federal Aviation Administration Aviation Research Division Center of Excellence (COE) for the Partnership to Enhance General Aviation Safety, Accessibility, and Sustainability (PEGASAS) 701 W. Stadium Ave. West Lafayette, IN 47907-2045	Final Report
	14. Sponsoring Agency Code ANG-E262

15. Supplementary Notes

The Federal Aviation Administration Aviation Research Division COR is Matthew Brynick.

16. Abstract

This report examines the potential use of phase change materials (PCMs) in airfield concrete pavements to store heat, which can be used to reduce ice formation and snow accumulation on the surface of the concrete pavement. This work mainly attempts to (1) determine the most beneficial properties of the PCM-concrete composite, (2) determine which PCMs to use and how they can be manufactured, and (3) evaluate the performance of pavements containing PCMs.

The research discussed in this report aims to improve understanding of how to incorporate PCMs into concrete pavement to revolutionize anti-icing/snow-removal practices in airfield concrete pavement technologies. This study shows that using PCMs in concrete pavement applications can melt ice and snow effectively, thereby decreasing the need for traditional snow/ice removal methods, such as snow plowing or deicing salt treatment, which can be costly and environmentally hazardous.

This research (1) identifies desirable PCMs for low-temperature applications, (2) characterizes potentially desirable PCMs for snow/ice melting applications in concrete pavement, (3) evaluates approaches to incorporate PCMs in concrete, (4) assesses thermal and durability behaviors of the cementitious materials containing PCMs, (5) examines using PCM in large-scale concrete slabs to evaluate heat release during cooling/snowing events to melt snow/ice, and (6) develops a numerical finite difference model to predict PCM performance in concrete pavement.

17. Key Words	18. Distribution Statement
Phase change material, Snow and ice removal, Pavement	This document is available to the U.S. public through the National Technical Information Service (NTIS), Springfield, Virginia 22161. This document is also available from the Federal Aviation Administration William J. Hughes Technical Center at actlibrary.tc.faa.gov.

19. Security Classif. (of this report)	20. Security Classif. (of this page)	21. No. of Pages	22. Price
Unclassified	Unclassified	146	

ACKNOWLEDGEMENTS

This work was supported by the Federal Aviation Administration (FAA) through the Center of Excellence (COE) for the Partnership to Enhance General Aviation Safety, Accessibility, and Sustainability (PEGASAS) Project and Joint Transportation Research Program (JTRP) administered by the Indiana Department of Transportation (SPR-3864). The authors would like to acknowledge the support that has made this work possible.

.

TABLE OF CONTENTS

LIST OF FIGURES

LIST OF TABLES

LIST OF SYMBOLS AND ACRONYMS

Ca^{++}	Ionized calcium
$CaCl_2$	Calcium chloride
Cl^-	Chloride anion
He	Helium
K^+	Ionized potassium
$MgCl_2$	Magnesium chloride
mm Hg	millimeter of Mercury (unit of pressure)
Na^+	Ionized sodium
NaCl	Sodium chloride
OH^-	Hydroxide anion
DSC	Differential scanning calorimeter
EMT	Effective Medium Theory
FAA	Federal Aviation Administration
FAME	Fatty acid methyl esters
FID	Flame ionization detector
GC	Gas chromatograph
J/g	Joules per gram
J/kg	Joules per kilogram
kg/m^3	Kilograms per cubic meter
LGCC	Longitudinal guarded comparative calorimeter
LT-DSC	Low-temperature differential scanning calorimeter
LWA	Lightweight aggregate
nm	nanometers
OPC	Ordinary Portland cement
PCM	Phase change material
PEGASAS	Partnership to Enhance General Aviation Safety, Accessibility, and Sustainability
PTV	Programmable temperature vaporizing injector
SSD	Saturated-surface-dry
TAG	Triglycerides
w/*c*	Water-to-cement ratio
µm	micron

EXECUTIVE SUMMARY

Extreme temperatures and weather events can cause thermal distresses, such as freeze-thaw damage and cracking, to airfield pavement. Snow and ice on airfield pavement can also cause hazardous conditions for aircraft and operators. Traditional snow- and ice-removal methods, such as snow plowing or deicing salt treatment, can be costly, time consuming, and environmentally hazardous. The Federal Aviation Administration (FAA) is researching alternatives for more effective methods to keep airfield pavement clear and reduce distresses. This research study aims to improve understanding of how phase change materials (PCMs) can be incorporated in concrete pavement to improve anti-icing/snow-removal practices in airfield concrete pavement technologies.

This research study examined how PCMs can be used in airfield concrete pavements to store heat to reduce ice formation and snow accumulation on the surface of the concrete pavement. The main objectives were to: (1) determine the most beneficial properties of the PCM-concrete composite, (2) assess which PCMs to use and determine how to manufacture them, and (3) evaluate the performance of pavements containing PCM. Incorporating PCMs into concrete pavement was found to be effective in releasing a considerable amount of heat during phase transformation to melt ice and snow on the surface of the concrete pavement, thereby decreasing the need to use traditional snow- and ice-removal methods, such as snow plowing or deicing salt treatment.

Several types of PCMs were examined, including vegetable-based (fatty acid methyl esters) and petroleum-based (paraffin oil) PCMs. The thermal properties of PCMs were evaluated, the temperature of the liquid-solid phase transition was determined, and the latent heat absorbed or released during the phase change was measured. The thermal properties of PCMs can be changed by altering the compositions to keep them in the desired temperature range for concrete pavement anti-icing applications.

Binary mixtures of fatty acid methyl esters and paraffin oil were found to provide desirable thermal properties for use as low-temperature PCMs, which can improve anti-icing practices. Phase diagrams were developed for binary mixtures of fatty acid methyl esters that can provide valuable information about the thermal properties at a range of methyl ester compositions. This information can be used in mathematical model development for simulating the anti-icing behaviors of these PCMs in concrete.

Different approaches were evaluated to determine the most effective use of PCM in concrete to reduce ice and snow without damaging the concrete pavement. This study used two methods: (1) placing the PCM in lightweight aggregates (LWAs) and using the LWA containing PCM to make the concrete slab, and (2) placing the PCMs in embedded pipes that were fabricated inside the concrete slabs during concrete casting. The embedded pipes seemed to be less practical in real application because of their complexity. However, for proof of concept, embedded pipes allow the PCM to be more easily incorporated into the pavement materials in the laboratory. Both LWA and embedded pipes were found to be effective in incorporating PCM and storing energy in concrete to melt ice and snow.

LWAs can be used to incorporate PCMs in concrete pavement. Several LWAs were examined, including calcined shale, slate, and clay. Each LWA chosen can first be soaked to absorb sufficient amounts of PCM; the PCM-impregnated LWA can then be used as aggregate to make concrete. Because this method can be done during concrete production, it is more practical compared to using embedded pipes, so long as the LWA-PCM combination works properly. Conversely, embedding pipes during concrete construction can be time consuming and expensive. Further research is needed to compare the economic aspects of using different methods to incorporate PCM in the concrete pavement.

Chemical and physical durability aspects of incorporating PCMs in concrete were also assessed. When the PCM was stored in LWA and placed in the concrete, some PCMs (e.g., methyl laurate) reacted with cementitious materials creating cracking and damage to the concrete. Embedded pipes were found to be more effective than LWAs in preventing concrete-PCM interactions.

Both methods of using PCMs showed potential to melt snow/ice on the surface of the concrete slabs. However, the capability of snow melting on the slabs with embedded pipes containing PCM substantially decreased when the concrete slab was exposed to an ambient temperature near or below the freezing temperature of PCM before it snowed. When the PCMs were placed in the LWAs compared to placing PCM in pipes, heat released more gradually (due to pore size), therefore the snow melting capability remained more beneficial.

A one-dimensional finite difference numerical model was developed to predict the macroscopic freeze-thaw behavior in concrete. The thermal response of the concrete was estimated using this model and was used to predict the thermal behavior (i.e., temperature profile and heat flow) of concrete exposed to cooling and heating thermal cycles. The computational results were compared to and verified with the experimental ones. This model can be used to simulate PCM incorporation in concrete pavement applications.

Using the developed model, the thermal response of concrete pavements containing PCMs was simulated at four U.S. airports (Minneapolis-St. Paul International, Indianapolis International, Atlantic City International, and Portland International) to determine the optimum performance of PCMs in various weather conditions (i.e., temperature). Incorporating PCMs in concrete pavement was found to be very effective in reducing the number of freezing events in concrete pavement.

In general, this study: (1) determined the most suitable properties of the PCM-concrete composite, (2) determined the PCM materials to use and how these PCMs can be manufactured, (3) determined the methodology that can be used to incorporate PCMs into concrete pavement, (4) evaluated the performance of pavements containing PCMs, and (5) predicted and optimized the thermal behavior of concrete pavement containing PCMs in different environmental conditions using the developed numerical model. This study also shows that PCMs can be used to melt snow/ice on pavement, thereby decreasing the need to use traditional snow- and ice-removal methods. Other factors, such as concrete pavement durability, skid resistance for transportation safety, and long-term stability of PCMs in concrete pavements should also be investigated on a large scale to further understand the effects of using PCMs in concrete to melt snow and ice on concrete performance.

1. INTRODUCTION

Extreme temperatures and weather events can cause thermal distresses, such as freeze-thaw damage and cracking, to airfield pavement. Snow and ice on airfield pavement can also cause hazardous conditions for aircraft and operators. Traditional snow- and ice-removal methods, such as snow plowing or deicing salt treatment, can be costly, time consuming, and environmentally hazardous. The Federal Aviation Administration (FAA) is researching alternatives for more effective methods to keep airfield pavement clear and reduce distresses. As a part of an FAA study through the Partnership to Enhance General Aviation Safety, Accessibility, and Sustainability (PEGASAS) Center of Excellence for General Aviation, the research team initiated an investigation into the potential use of PCMs in concrete pavements to reduce ice formation and snow accumulation on concrete pavements.

Phase change materials (PCMs) are frequently used to store thermal energy. This research study examined the potential for PCMs to be used in airfield pavements to improve anti-icing practices. PCMs are organic, inorganic, or eutectic materials that can produce a considerable amount of energy/heat during their phase transformation from liquid to solid. PCMs can store energy from ambient, applied, or solar sources. Due to their high heat of fusion, the stored energy can be released during cooling (i.e., during a freezing/icing event), thereby melting snow and delaying or preventing ice formation.

Heat is absorbed by PCMs when the material changes from solid to liquid and is released during the change from liquid to solid. In the construction industry, PCMs have historically focused on storing energy in buildings to reduce heating and cooling loads. However, the work reported herein focuses on investigating the extension of PCM use in concrete pavements, enabling them to be used for anti-icing.

PCMs have previously been investigated for use in concrete and pavement. Bo et al. (2011) examined the use of PCM in pavements as a method to reduce the heat island effect. Sakulich & Bentz (2012a) investigated the potential for PCM to be used in U.S. locations as a method to reduce the number of freeze-thaw cycles in concrete bridge decks. Cocu et al. (2013) examined the use of PCM in grouted asphalt and in concrete where the PCM replaced a portion of the fine aggregate. Cocu et al. (2013) concluded that while "the results of the preliminary study are encouraging" one needs to "continue investigating any technical solution that makes it possible to increase the amount of PCM in pavement." Stoll et al. (1996) examined the use of PCM to reduce overnight freezing in bridge decks and concluded that PCMs can "significantly reduce the hazard of early bridge freezing; however, there are design issues that must be addressed before a final design and demonstration can be completed." While several approaches have investigated the concept of PCM in pavements and bridge decks, this study's goals are to: (1) determine the most desirable properties of the PCM-concrete composite, (2) determine the PCM materials to use and how these PCMs can be manufactured, and (3) evaluate the performance of pavements.

The main objective of this research is to examine the role that PCMs could have in storing heat in pavements to delay and reduce the decrease in surface temperature and to melt ice or snow on the surface of the concrete pavement. This work includes several main topics that are documented in the current report in the following sections.

Section 1 presents the introduction, motivations, and objectives for this study. The structure and organization of the report are also discussed in the first section.

Section 2 focuses on identifying the most promising phase change materials and delivery techniques. PCMs can be formed from salt hydrates, esters, paraffins, and triglycerides (TAG) (fats). This section examines the thermal properties of PCMs made of fatty acids and methyl esters by using a low-temperature differential scanning calorimeter (LT-DSC). The temperature of the liquid-solid phase transition is determined, and the latent heat absorbed or released during the phase change is measured using the LT-DSC for each PCM. This work discusses how the thermal properties can be changed by altering the compositions to remain in the desired temperature range above the freezing temperature of present solution inside the pores.

In the search for a suitable PCM, section 3 examines the use of low-melting organic materials. Fatty acid methyl esters (FAME) show solid-liquid phase transitions with desirable thermal properties within a narrow temperature range. FAME mixtures can be tailored to include a desired phase transition temperature for low-temperature pavement applications. They are commercially available and are sustainably derived from common vegetable and animal oils providing renewable supply without depending on petroleum. In this section, the thermal properties of two binary mixtures that can provide the required thermal characteristics to melt snow and ice, methyl laurate + methyl myristate (C12-C14) and methyl laurate + methyl palmitate (C12-C16), were investigated. Additionally, solid-liquid phase diagrams for each of the binary mixtures were developed providing information on the *liquidus* line and transitions below the *liquidus* line are reported in the present study. This section provides information on the binary mixtures of FAME that can be used to select a desired PCM for a concrete pavement based on the local environmental condition.

Section 4 discusses the approaches that can be used to incorporate PCMs in concrete and the thermal properties of concrete containing PCMs. This section examines an advanced calorimetry technique (i.e., longitudinal guarded comparative calorimetry [LGCC]) to characterize the thermal response of an entire mortar-PCM system to melt ice and snow and evaluates the physical and durability performance of mortar containing PCMs. The main objective of this section is to determine whether PCMs are effective enough on ice and snow melting when they are used inside cementitious material. It is essential that potential PCMs for deicing applications also show promising performance when they are used in concrete in terms of released heat, desired phase transformation temperature, chemical and physical stability, and concrete durability.

In previous sections, this report focused on how to: (1) fabricate and characterize desirable PCMs for snow/ice melting applications in concrete pavement, (2) evaluate approaches to incorporate the desired PCMs in concrete, and (3) assess thermal and durability behaviors of concrete containing PCMs. Section 5 addresses how to incorporate PCMs in a large-scale concrete slab and evaluate their thermal potential to release heat during cooling/snowing events to melt snow/ice. Large-scale concrete slabs were prepared to simulate concrete pavements, and PCMs were incorporated in the slabs using different approaches. The slabs were then tested in a cooling-heating chamber, and an artificial snow melting experiment was performed.

Section 6 discusses developing a model that can be used to simulate phase transformations (i.e., freezing and thawing) in concrete. This section presents a one-dimensional finite difference model that is developed to describe the freeze-thaw behavior of an air-entrained mortar containing deicing salt solution. A phenomenological model is used to predict the temperature and the heat flow for mortar specimens during cooling and heating. Phase transformations associated with the freezing/melting of water/ice or transition of the eutectic solution from liquid to solid are included in this phenomenological model.

Section 7 contributes to the existing knowledge of how to use PCMs in airport concrete pavement by simulating the thermal behavior of two sets of experiments using the one-dimensional finite difference method. The thermal responses of two experiments with different scales (that were discussed in sections 5 and 6) are compared with the numerical results (that are developed in sections 6 and 7) during the freeze-thaw thermal cycles to assess the validity of the model on application of PCMs in concrete. In this section, real-scale concrete pavements at four different locations are also investigated to evaluate the efficiency of using PCMs during cold seasons where the temperature of pavement drops below 0 °C. This section reveals how incorporating PCMs can improve anti-icing practices in airfield pavements.

Section 8 summarizes all the results/outcomes and presents the conclusions of the current this research.

2. THE USE OF PCMs IN CONCRETE PAVEMENTS: EVALUATION OF THERMAL PROPERTIES OF PCMs

PCMs have the potential to be used to store thermal energy from ambient, solar, or applied sources. PCMs have been conventionally used in solar water-heating systems, greenhouses, building walls and floors, and even window shutters (Regin, Solanki, & Saini, 2008; Sharma, Tyagi, Chen, & Buddhi, 2009; Abhat, 1983). PCMs may also be used in the concrete infrastructure to alter anti-icing practices in concrete pavements (Sakulich & Bentz, 2012a; Bentz & Turpin, 2007; Sakulich & Bentz, 2012b; Ling & Poon, 2013). Due to the PCMs' high heat of fusion, the stored energy can be released during cooling (i.e., during a snow/ice event), thereby delaying or preventing ice formation. This can help to eliminate or decrease the deicing salt demand to melt ice or snow on the surface of concrete pavements. Deicing salts can cause premature deterioration (e.g., physical or chemical damage) in concrete pavement (Farnam, Bentz, Hampton, & Weiss, 2014; Farnam, Bentz, Sakulich, Flynn, & Weiss, 2014). Figure 1 shows schematic of using PCM in concrete pavement to melt ice and snow using a lightweight aggregate (LWA) (Sakulich & Bentz, 2012a; Sakulich & Bentz, 2012b).

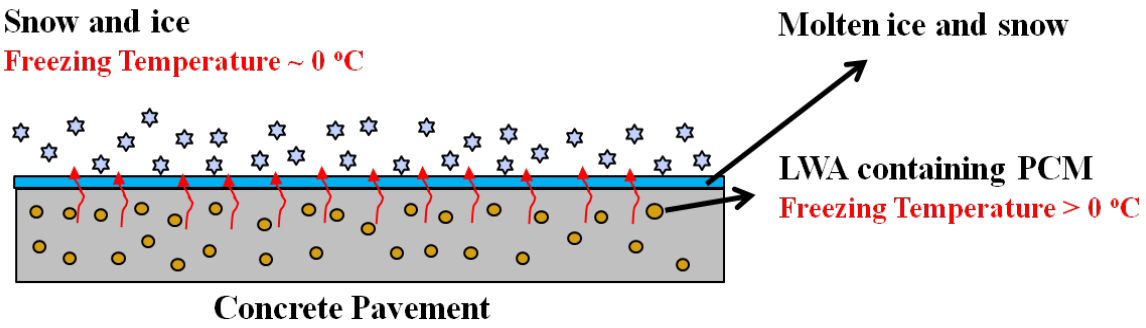

Figure 1. Using PCM in Concrete Pavement to Melt Ice and Snow

Using PCMs in the concrete infrastructure requires specific thermodynamic, physical, and chemical properties that are compatible with the concrete. The desirable thermal properties needed for successful use in concrete to melt ice include a phase transition temperature near 0 °C, high latent heat of fusion, high specific heat (heat capacity), and high thermal conductivity (Sakulich & Bentz, 2012a; Bentz & Turpin, 2007; Sakulich & Bentz, 2012b; Ling & Poon, 2013). The PCM's physical properties should include high density, small volume change between phases, and low vapor pressure. PCM's chemical properties should include stability and compatibility with concrete, and they should be non-toxic and non-flammable. PCMs that are economical, commercially available, and environmentally friendly are also important.

Further, the PCMs should be able to be added to the concrete without extensive changes to the construction practice. Different methods have been proposed to use PCM in concrete elements (Bentz & Turpin, 2007; Hawes, Banu, & Feldman, 1992; Hawes & Feldman, 1992). Figure 2 illustrates schematics of three methods of incorporating a PCM into concrete. Figure 2(a) indicates filling steel tubes with liquid paraffin wax to raise the latent heat of the concrete-steel tube system, thereby preventing freezing of bridge layers. Figure 2(b) illustrates incorporating the PCM directly within LWA in the concrete slab (Bentz & Turpin, 2007). Figure 2 (c) depicts the inclusion of PCM within the concrete pores and voids on the surface of the pavement; this method has also been used for applying sealants to pavement surface (Jones et al., 2013). The second two methods are likely simpler.

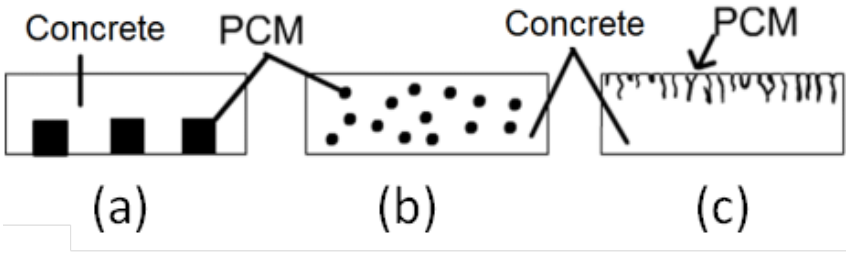

Figure 2. Three Methods to Incorporate PCM Into Concrete: (a) Using Pipes of PCM, (b) Using Particles Containing PCM, and (c) Filling Concrete Surface Voids with PCM

Thermal properties of PCMs made of fatty acids and methyl esters are evaluated by using an LT-DSC. The temperature of the liquid-solid phase transition is determined, and the latent heat

absorbed or released during the phase change is measured using the LT-DSC for each PCM. How the thermal properties can be changed by altering the compositions to remain in the desired temperature range is discussed in the following sections.

2.1 MATERIALS AND COMPOSITION

Through transesterification, the methyl esters used in this work were derived from high-oleic soybean oil, canola oil, and corn oil. TAG is mixed with methanol and then catalytically converted into glycerol and FAME. FAME have lower melting points than both the TAG and fatty acids from which they were derived. Unsaturated FAME (double bonds in the hydrocarbon chain) have lower melting points and less dense crystal structure than saturated FAME with the same number of carbons in the hydrocarbon chain (Voet, Voet, & Pratt, 2013; Gunstone, 2008). Figure 3 shows the transesterification process. The properties of each pure methyl ester is indicated in Table 1. Unsaturated FAME form less dense crystal structures because the double bonds found in the hydrocarbon chain can prevent simple compact stacking between molecules. The terminal carboxylate at the end of the FAME molecule sigificantly changes their physical, chemical, and biological properties versus analogous length petroleum hydrocarbons (see http://www.indianasoybean.com). Most importantly, this caroxylate strengthens the intramolecular forces between the FAME molecules lowering vapor pressure and making them more chemically stable.

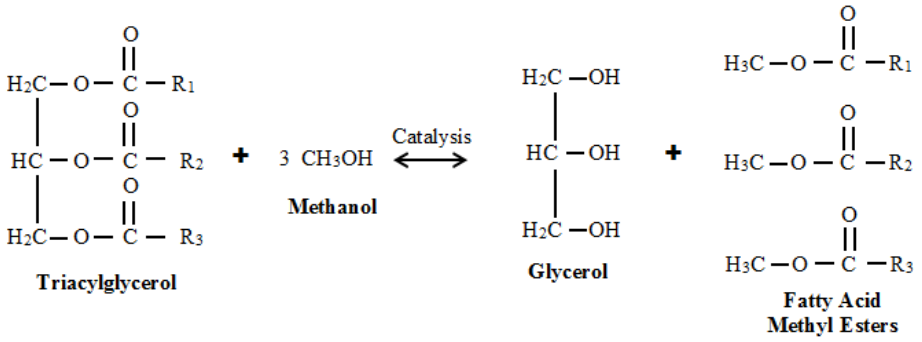

Figure 3. Transesterification Process

Table 1. Individual Pure Methyl Esters Derived by Transesterification and Their Thermal Properties (Haynes, 2013; Dunn, 2012)

Methyl Esters*	Molecular Formula	Enthalpy of Fusion (J/g)	Melting Point (°C)
Methyl Palmitate (C16:0)	$C_{17}H_{34}O_2$	222	29.6
Methyl Palmitoleate (C16:1)	$C_{17}H_{32}O_2$	–	-33.7
Methyl Stearate (C18:0)	$C_{19}H_{38}O_2$	237	38.7
Methyl Oleate (C18:1)	$C_{19}H_{36}O_2$	133	-19.4
Methyl Linoleate (C18:2)	$C_{19}H_{34}O_2$	121	-36.6
Methyl Linolenate (C18:3)	$C_{19}H_{32}O_2$	–	-49.0
Methyl Arachidate (C20:0)	$C_{21}H_{42}O_2$	–	46.4

Methyl Esters*	Molecular Formula	Enthalpy of Fusion (J/g)	Melting Point (°C)
Methyl Gadoleate (C20:1)	$C_{21}H_{40}O_2$	–	-34.0
Methyl Behenate (C22:0)	$C_{23}H_{46}O_2$	–	53.3
Methyl Erucate (C22:1)	$C_{23}H_{44}O_2$	–	-1.1

*(C##: #): The first number represents the number of carbons in the hydrocarbon chain and the number after the colon represents the number of double bonds in the chain (the unsaturated methyl esters). The enthalpy of fusion is not available for all methyl esters.

High-oleic soybean oil, canola oil, and corn oil were used to derive methyl esters (methoxylated long chain fatty acids). The compositions of high-oleic soybean methyl esters, canola methyl esters, corn methyl esters, and generated methyl esters mixtures were determined using a Thermo Scientific TRACE™ Ultra Gas Chromatograph (GC) equipped with a variable split-flow programmable temperature vaporizing (PTV) injector, temperature programmable oven, and a flame ionization detector (FID). The GC operating conditions were configured to follow the standard method, BS EN 14103-2011 (British Standards Institution, 2011). The analytical capillary column used is a polar EC™-WAX, 30-m length × 0.25-mm inner diameter × 0.25-micron (µm) film thickness, and 1 µL of the sample diluted in hexane was injected with a carrier gas (helium [He]) of 1.4 mL/min. The PTV injector was at 250 °C with a split flow of 70 mL/min of helium (50:1 ratio). The oven was programmed initially to start at 110 °C, held for 0.5 min; a ramp of 20 °C/min to 130 °C, held for 0.5 min; a ramp of 30 °C/min to 220 °C, held for 1 min; and ramp of 10 °C/min to 250 °C held for 7 minutes. The FID was set at 275 °C with air flow of 300 mL/min, hydrogen of 30 mL/min, and make-up flow (He) of 30 mL/min.

A potential PCM with desired thermal properties can be obtained by combining different mixtures of fatty acids, methyl esters, and TAG to be used in concrete pavement. Samples with different amounts of individual methyl esters (Table 2) were prepared to obtain a PCM with desired thermal properties. The compositions of all samples studied so far in this work are summarized in Table 2 and Figure 4.

Table 2. Composition of Methyl Ester Samples (% by mass)

Samples	C16:0	C18:0	C18:1	C18:2	C18:3	Other[1]	Total Saturates[2]
ME1	8.3	4.3	72.6	9.9	2.6	2.4	14.4
ME2	11.3	2.3	28.8	55.9	0.9	0.9	14.3
ME3	4.6	2.2	62.5	20.2	8.3	2.3	8.0
ME3 Sat	9.8	5.5	61.4	14.0	5.0	4.3	17.7
ME3 Unsat	1.4	0.3	62.9	24.2	10.0	1.2	2.8
Mixture 1	15.7	4.1	69.2	7.2	2.3	1.5	20.8
Mixture 2	25.8	3.7	60.3	6.8	2.0	1.5	30.4
Mixture 3	35.9	3.2	52.1	5.8	1.8	1.3	39.9
Mixture 4	5.1	14.0	68.0	8.8	2.3	1.9	20.5
Mixture 5	4.4	24.7	59.5	7.7	2.0	1.7	2.8
Mixture 6	3.8	35.5	51.0	6.6	1.7	1.4	40.4
Mixture 7	20.1	-	79.9	-	-	-	20.1

Samples	C16:0	C18:0	C18:1	C18:2	C18:3	Other[1]	Total Saturates[2]
Mixture 8	-	20.7	79.3	-	-	-	20.7
Mixture 9	10.0	10.0	80.0	-	-	-	20.0
Mixture 10	30.0	-	70.0	-	-	-	30.0
Mixture 11	-	30.0	70.0	-	-	-	30.0
Mixture 12	17.1	2.2	26.9	52.1	0.8	0.9	20.0
Mixture 13	27.2	2.0	23.7	45.5	0.7	0.9	30.0
Mixture 14	37.4	1.9	20.4	38.8	0.6	0.9	40.0
Mixture 15	16.9	2.0	54.2	17.6	7.1	2.1	20.0
Mixture 16	27.1	1.9	47.4	15.5	6.2	2.0	30.0
Mixture 17	37.3	1.7	40.5	13.4	5.3	1.8	40.0

[1]Other includes methyl esters of either C16:1, C20:0, C22:0, or C22:1.
[2]Total Saturates includes any of C16:0, C18:0, or C20:0 methyl esters.
ME1: high oleic soybean methyl esters, **ME2:** corn methyl esters, **ME3:** canola methyl esters, **ME3 Sat:** fractionated canola methyl esters containing majority of the saturates, **ME3 Unsat:** fractionated canola methyl esters with a majority of the saturates removed, **Mixture 1:** ME1 + C16:0 for a total of 20% saturates, **Mixture 2:** ME1 + C16:0 for a total of 30% saturates, **Mixture 3:** ME1 + C16:0 for a total of 40% saturates, **Mixture 4:** ME1 + C18:0 for a total of 20% saturates, **Mixture 5:** ME1 + C18:0 for a total of 30% saturates, **Mixture 6:** ME1 + C18:0 for a total of 40% saturates, **Mixture 7:** "Pure" C16:0 20% + C18:1 80%, **Mixture 8:** "Pure" C18:0 20% + C18:1 80%, **Mixture 9:** "Pure" C16:0 10% + C18:0 20% + C18:1 80%, **Mixture 10:** "Pure" C16:0 30% + C18:1 70%, **Mixture 11:** "Pure" C18:0 30% + C18:1 70%, **Mixture 12:** ME2 + C16:0 for a total of 20% saturates, **Mixture 13:** ME2 + C16:0 for a total of 30% saturates, **Mixture 14:** ME2 + C16:0 for a total of 40% saturates, **Mixture 15:** ME3 + C16:0 for a total of 20% saturates, **Mixture 16:** ME3 + C16:0 for a total of 30% saturates, **Mixture 17:** ME3 + C16:0 for a total of 40% saturates

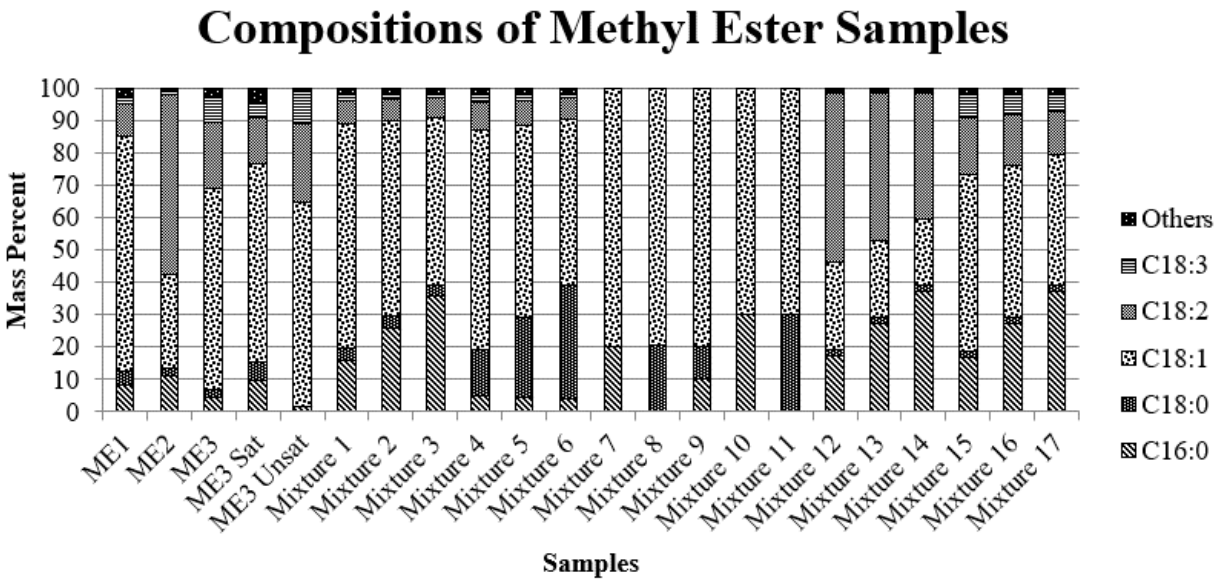

Figure 4. Compositions of Methyl Esters

Two types of LWAs were used in this study: LWA #1 (Buildex, Marquette) and LWA #2 (Haydite® AX). These are common LWAs used in the Midwest. The properties of these LWAs are described in (Castro, Keiser, Golias, & Weiss, 2011).

2.2 TESTING PROCEDURE

Low-temperature calorimetry studies were performed to understand the thermal behavior of PCMs. The absorption of water and of PCM into LWA were also studied.

2.2.1 Low-Temperature Differential Scanning Calorimetry

To determine the thermal properties of the potential PCM samples, a TA Q2000 LT-DSC instrument was used. The heat flow and temperature associated with phase transitions in materials was obtained. Tzero aluminum pans with hermetic lids were used to contain the samples. The initial temperature of the test was set to equilibrate at 40 °C. After the initial temperature became stable, the LT-DSC cell was cooled to -80 °C at a cooling rate of 5 °C/min. The temperature of the specimen was then increased to 40 °C at a rate of 5° C/min. The mass of sample was 11 mg ±2 mg.

2.2.2 Absorption of Water into LWA

The absorption capacity of water for the LWA was tested using a vacuum procedure (Castro, Keiser, Golias, & Weiss, 2011). To saturate the LWA specimens, they were placed in a desiccator and evacuated to a pressure of 10 mm Hg ±5 mm Hg for 3 hours. After evacuation and while still under vacuum, deaerated water (deaerated by vacuuming the solution for 15 minutes) was introduced into the desiccator to cover the specimens for 1 hour. The LWA specimens were maintained in a condition where they were submerged below water for 18 hours. The water was removed from the surface of aggregate using a centrifuge (Miller et al., 2014). The saturated-surface-dry (SSD) samples were then placed in a 105 °C oven for a day, and the water absorption calculated. The mass percent absorbed was calculated using Equation 1.

$$Mass\ \% = \frac{LWA_{SSD} - LWA_{Dry}}{LWA_{Dry}} \times 100 \quad (1)$$

2.2.3 Absorption of PCM into LWA

The absorption of PCM into LWA was evaluated using two different conditions: ambient and vacuum pressure. Under ambient conditions, the LWA samples were weighed into flasks and covered with methyl esters (ME2). Methyl esters were allowed to penetrate the pores for 24 hours before being towel-dried (SSD condition) and weighed. The mass percent absorbed was calculated using Equation 1.

For vacuum pressure absorption, LWA was weighed and placed into a flask. The flask was exposed to vacuum pressure of approximately 80.5 kPa for 45 minutes. Methyl esters (ME1) were then introduced into the flask to completely submerge the aggregate. Operation of the vacuum was stopped, and air was allowed back into the flask to drive the methyl esters into the pores of the aggregate for 30 minutes (Zhang, Li, Zhou, & Wu, 2004). The aggregate with methyl esters were towel-dried (SSD condition) and weighed to calculate the absorbed percentage, using Equation 1. The setup for the vacuum absorption experiment is shown in Figure 5.

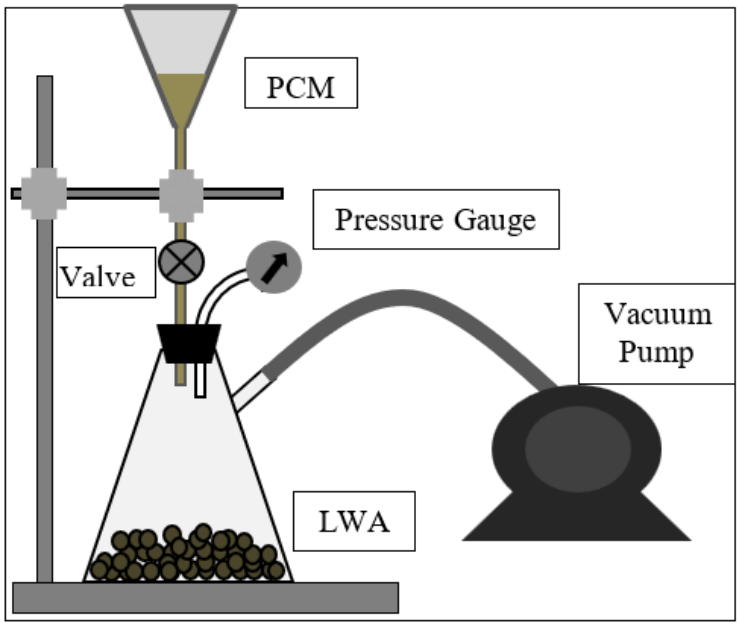

Figure 5. Vacuum Absorption Experiment

2.3 RESULTS

2.3.1 Thermal Response of PCMs

Figure 6shows a typical differential scanning calorimeter (DSC) result of a test performed on a methyl ester mixture. The most important feature of methyl esters is the type of bonds and number of carbons in the hydrocarbon chain. The mixtures used in testing contained a majority of C16:0 (methyl stearate), C18:0 (methyl palmitate), C18:1 (methyl oleate), C18:2 (methyl linoleate), and C18:3 (methyl linolenate); and approximately 3% of other methyl esters.

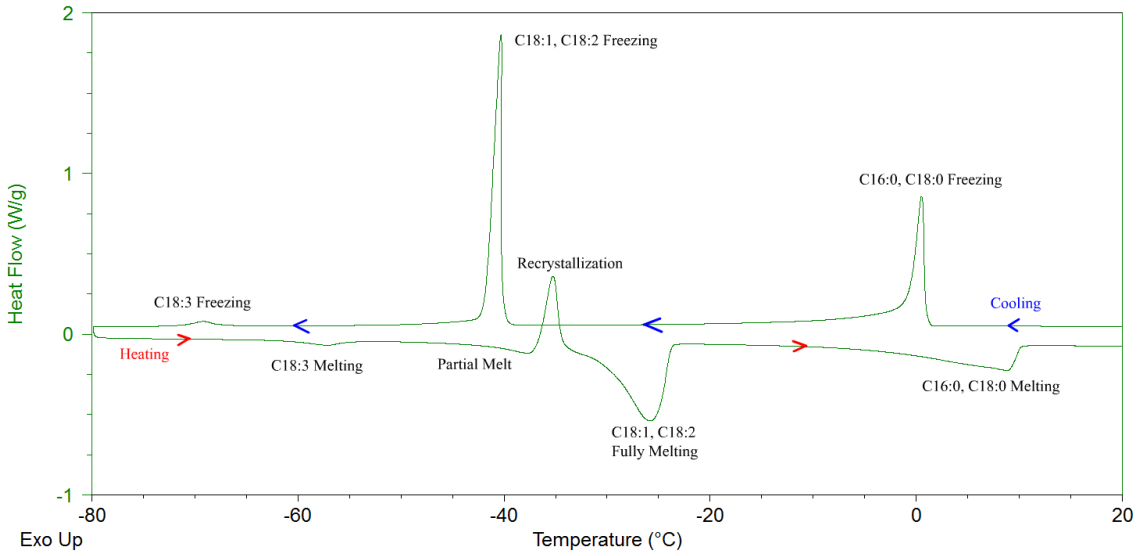

Figure 6. Typical DSC Response During Cooling and Heating

The first exothermic peak that occurs in Figure 6 indicates the freezing of saturated methyl esters (C16:0 and/or C18:0), and the latter exothermic peaks are associated with the freezing of increasingly unsaturated methyl esters (i.e., more double bonds). These unsaturated methyl esters are the first to melt during the heating cycle. Recrystallization events occur during the heating cycle, illustrating the complex nature of TAG and their derivatives. This behavior is a consequence of polymorphism, the ability to crystallize in multiple crystallographic patterns (Marangoni, 2011). The melting of one type of methyl ester triggers the recrystallization of another type, which in turn causes both types to melt (Foon et al., 2006). Because the melting temperature of the saturated methyl esters is much higher than their freezing temperature, they can demonstrate supercooling. There are two possible reasons for supercooling: (1) nucleation difficulties, and (2) the unsaturated methyl esters prevent the saturated methyl esters from freezing in a solute/solvent interaction, governed by the freezing point depression theory (Dunn, 2008). Although the enthalpy of the unsaturated methyl esters during freezing does not appear to be useful for melting ice (because its freezing point is significantly lower than the melting point for ice), their presence is necessary to make the saturated methyl esters behave in a desirable manner. The heating curves may be a better representation of the thermal behavior of PCMs because no supercooling appears in the heating part of the DSC results.

Figure 7(a) shows the melting curves for high oleic soybean methyl esters, corn methyl esters, canola methyl esters, fractionated canola methyl with a majority of the saturated methyl esters removed, and fractionated canola methyl esters containing the majority of the saturates. The differences between ME1, ME2, and ME3 are attributed to the composition differences. Both ME1 and ME3 display the first small peak which is composed of C18:3 melting; ME2 does not display this peak because of the lack of C18:3 in its composition. The temperature for second peak (C18:1 and C18:2 behavior) for ME2 occurs at a significantly lower temperature than both ME1 and ME3 because ME2 contains a greater amount of C18:2 (C18:2 has a lower crystallization point than C18:1).

When comparing the canola methyl ester sample (ME3) to the fractionated canola methyl ester samples (ME3-Sat and ME3-Unsat), the DSC result shows changes in the desired peak (near 0 °C). In ME3-Unsat, the desired peak is no longer present, due to the removal of the saturated methyl esters. In ME3-Sat, the saturated methyl ester peak increases because it contains the majority of the saturated methyl esters that were removed from original sample. This result further emphasizes that saturated methyl esters are needed in the PCMs to have an energy release at the desired temperature range.

Figure 7(b) demonstrates that with the same percentage of C16:0 or C18:0 added to C18:1, the enthalpy will be lower and the melting point will be higher with the addition of C18:0 compared to C16:0. The comparison between 20% C16:0 versus C18:0 is seen in Mixture 7 and Mixture 8, and the comparison between 30% C16:0 versus C18:0 is seen in Mixture 9 and Mixture 10, respectively. Therefore, C16:0 may be chosen as the desired saturated methyl ester used in generating PCMs since the enthalpy needs to be as high as possible to increase the amount of ice melting on concrete pavement. It should also be mentioned that the amount and type of unsaturated methyl esters plays an important role in depressing the saturated methyl ester's freezing temperature.

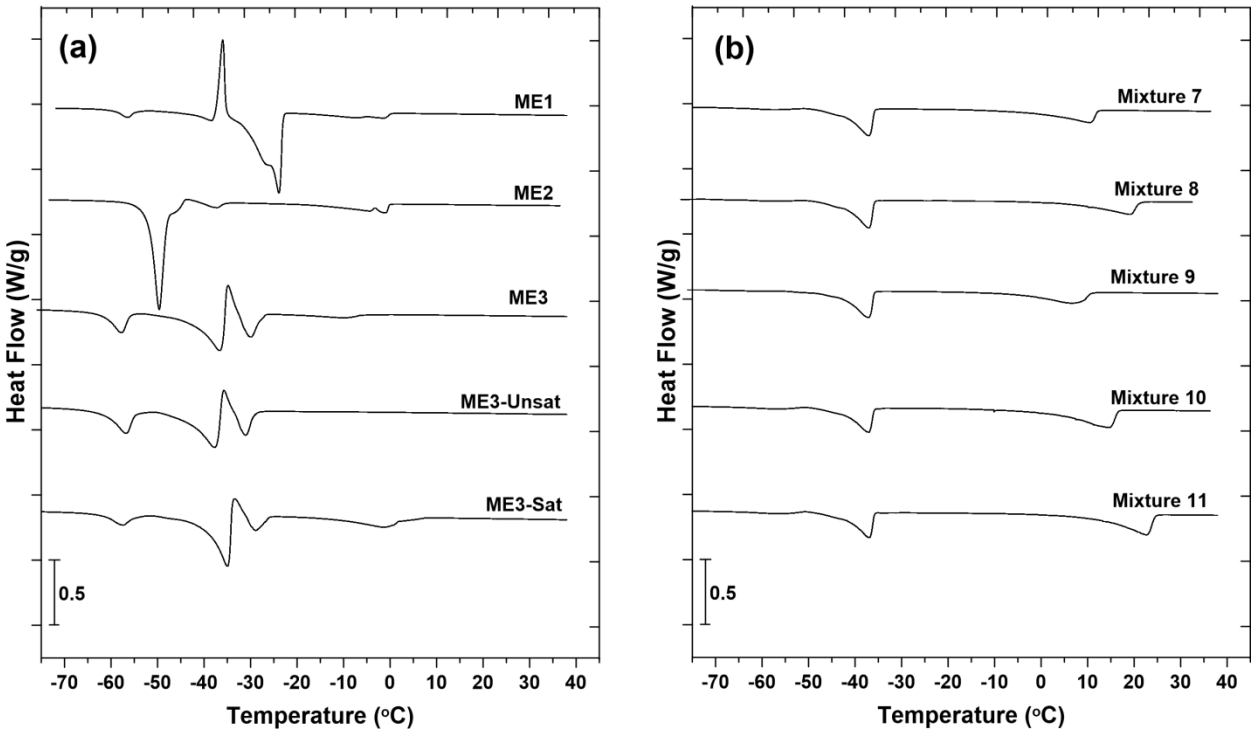

Figure 7. The DSC Responses during Heating Only for Methyl Esters Mixtures

2.3.2 Thermal Properties of PCMs

Table 3 contains the thermal properties of the first exothermic peak (associated with freezing the saturated methyl esters), the last endothermic peak (associated with melting the saturates), and the total enthalpy for all the enthalpic releases during the cooling or heating curves. Since the freezing/melting/enthalpy of saturated methyl esters can influence the ice melting efficiency of PCM, the first exothermic peak and the last endothermic peak are reported in this table. The temperature values are reported at the peak maximum rather than the onset temperature for the individual peaks. The enthalpy of the entire mixture cannot be used as an indication for ice melting because the different chemical species are freezing at their preferred temperature rather than freezing as a whole in a temperature near to ice melting temperature (0 °C). The enthalpy of freezing for saturated methyl esters appears to be related to total saturated methyl ester content. In addition, the composition of the saturated methyl esters content seems to also affect the enthalpy and freezing temperature.

Table 3. Thermal Properties of Methyl Ester Samples

	Cooling Curve			**Heating Curve**		
	C16:0, C18:0 Freezing Peak			C16:0, C18:0 Melting Peak		
Samples	Temp. (°C)	Enthalpy (J/g)	Total Curve Enthalpy (J/g)	Temp. (°C)	Enthalpy (J/g)	Total Curve Enthalpy (J/g)
ME1	-5.87°	(15.47)	(115.00)	-1.46°	(12.60)	(115.00)
ME2	-9.53°	(19.25)	(113.50)	1.01°	(19.84)	(111.10)
ME3	-21.50°	(7.66)	(97.32)	-9.88°	(6.82)	(99.15)
ME3 Sat	-11.41°	(26.94)	(110.00)	-1.29°	(22.72)	(97.43)
ME3 Unsat*	-	-	(80.41)	-	-	(85.25)
Mixture 1	-3.38°	(29.54)	(124.40)	-2.38°	(28.32)	(114.70)
Mixture 2	0.52°	(46.64)	(127.10)	8.88°	(45.57)	(119.80)
Mixture 3	6.31°	(60.81)	(138.30)	14.51°	(61.41)	(129.50)
Mixture 4	3.43°	(18.57)	(99.58)	12.02°	(16.20)	(87.93)
Mixture 5	11.56°	(32.86)	(111.40)	19.28°	(28.61)	(96.13)
Mixture 6	16.57°	(48.82)	(113.00)	23.69°	(46.03)	(96.88)
Mixture 7	0.24°	(30.31)	(72.79)	10.44°	(28.88)	(63.01)
Mixture 8	10.44°	(29.70)	(67.57)	18.99°	(29.26)	(58.17)
Mixture 9	1.92°	(26.15)	(69.19)	6.63°	(24.56)	(62.14)
Mixture 10	7.16°	(45.23)	(77.37)	14.71°	(42.54)	(73.93)
Mixture 11	15.08°	(45.95)	(90.92)	22.72°	(42.82)	(76.15)
Mixture 12	-5.23°	(22.03)	(86.60)	4.57°	(20.22)	(87.82)
Mixture 13	2.53°	(36.62)	(94.46)	11.45°	(34.44)	(89.65)
Mixture 14	8.18°	(53.62)	(112.40)	15.92°	(52.35)	(101.00)
Mixture 15	-4.61°	(22.28)	(84.33)	3.14°	(21.95)	(76.51)
Mixture 16	2.07°	(37.86)	(97.87)	9.18°	(38.99)	(87.40)
Mixture 17	7.82°	(52.25)	(102.00)	15.94°	(50.48)	(77.34)

*ME3 Unsat did not display the saturated methyl ester peak

2.3.3 Absorption of Water and PCMs into LWAs

In Table 4, the water vacuum absorption experiment results, which can be used as a control experiment for the total possible absorption, are compared with the vacuum and ambient absorption of LWAs into concrete.

Table 4. Water Absorption of LWAs Under Vacuum Condition

Sample	Retained Sieve Number	Water Vacuum Absorption (mass %)	PCM Vacuum Absorption (mass %)	PCM Ambient Absorption (mass %)
LWA #1		32%	-	-
Graded LWA #1	#4	-	23%	13%
	#8	35%	28%	16%
	#16	33%	27%	20%
	#30	31%	27%	20%
	#50	29%	23%	19%
	Pan	26%	-	-
LWA #2		23%	-	-
Graded LWA #2	#4	-	23%	8%
	#8	29%	24%	10%
	#16	26%	20%	12%
	#30	19%	16%	12%
	#50	17%	5%	7%
	Pan	13%	-	-

The vacuum pressure conditions for methyl ester absorption can be used as the control for the maximum absorption of methyl esters (Figure 8). Comparing these results to the water absorption experiment (Table 4), the data shows that the methyl esters under vacuum conditions are not reaching the maximum possible mass percent absorption of the water. These differences might be due to changes in specific gravity, viscosity, molecule size, and surface tension of the liquid. More research and experimentation are needed to determine the specific factors affecting this slight decrease in the absorption of methyl esters.

Figure 8 compares methyl ester absorption under the ambient conditions with the vacuum pressure conditions. It appears that as the LWA size decreases, the difference between the amounts absorbed between vacuum and ambient conditions decreases. One possible explanation for this is that the pores in the larger aggregate are bigger and, therefore, due to the lack of sufficient capillary suction, more time is needed at ambient conditions for methyl esters to ingress fully into the pores.

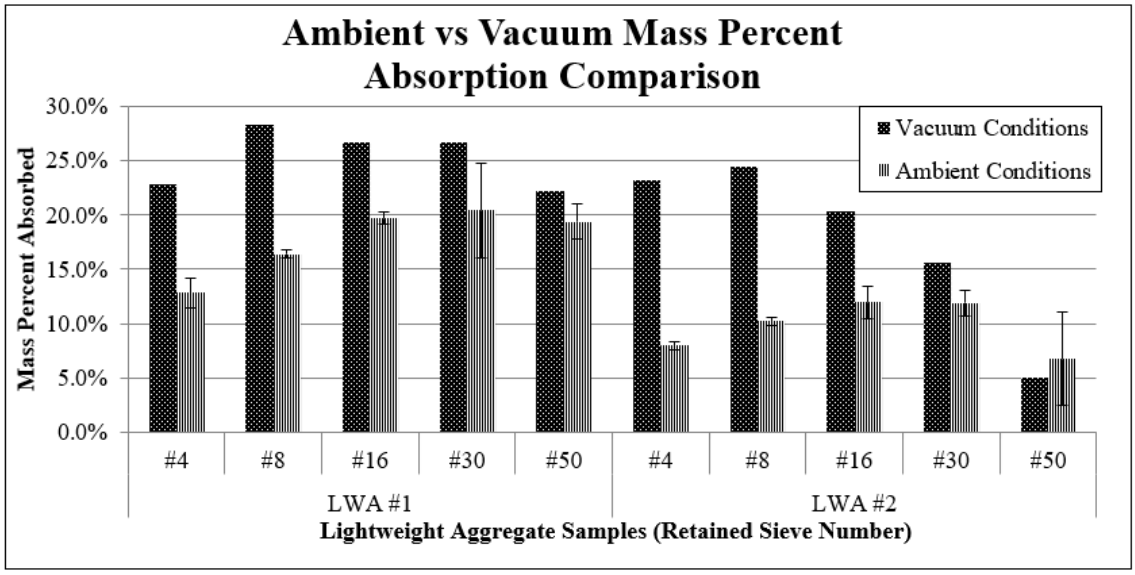

Figure 8. Comparison of Vacuum and Ambient Methyl Ester Mass Percent Absorption Conditions (The error bars represent ±1 standard deviation between three trials; the vacuum absorption is for only one trial.)

2.4 CONCLUSIONS

This study discusses the potential of the technology that incorporates PCMs in concrete pavement by inclusion of the PCMs in LWAs. Several organic PCMs were evaluated for their potential use in concrete pavement, and their thermal properties were determined. In addition, the absorption of PCMs into LWAs was investigated. Based on the results obtained in this work, the following conclusions can be drawn:

- A change in the concentration and the type of saturated methyl esters (C16:0 and C18:0) alters the thermal properties of methyl ester PCM samples. Increasing the methyl palmitate content (C16:0) results in a change toward the desired thermal properties required for concrete pavement application and ice melting.
- A change in the type of unsaturated methyl esters influences the freezing temperature of the saturated methyl esters. It seems that the use of unsaturated methyl esters with multiple double bonds (C18:2 and C18:3) tends to suppress the freezing temperature of the saturated methyl esters more than methyl esters with a single double bond (C18:1).
- There seemed to be a slight reduction in PCM ingress into the LWA. This reduction is considerable when the LWA is saturated in an ambient condition.
- Only a small portion of entire enthalpy for the methyl ester PCM samples is released in the temperature range required for ice melting on concrete pavement.

As a part of the ongoing project, more research is being performed to investigate the thermal behavior of other PCMs, such as paraffin oil and TAG. TAG have more complex crystallization behaviors, but with the small addition of saturated methyl esters, they may be able to kick-start crystallization in the desired temperature range. When results of this study are compared to those of future studies, it will be possible to propose PCMs for concrete pavement applications.

3. FABRICATING PCMs FOR LOW-TEMPERATURE PAVEMENT APPLICATIONS USING BINARY MIXTURES OF FAME

PCMs are latent heat storage materials that have the ability to absorb thermal energy from external sources and release the energy during phase transitions. The use of high latent enthalpy PCMs in concrete infrastructure has been proposed as a possible method for altering anti-icing practices on concrete pavements (Sakulich & Bentz, 2012a; Sakulich & Bentz, 2012b; Bentz & Turpin, 2007; Ling & Poon, 2013; Liston et al., 2014; Farnam, Krafcik, Liston et al., 2016). The energy stored in PCMs can be released during cooling (crystallization) and absorbed during heating (melting). The released energy can reduce the amount of snow and ice on the surface of the pavement, thereby decreasing the use of deicing salts and improving the durability of concrete (Farnam, Wiese, Bentz, Davis, & Weiss, 2015; Farnam, 2015; Esmaeeli, Farnam, Bentz, Zavattieri, & Weiss, 2016; Farnam, Bentz, Hampton, & Weiss, 2014; Farnam Bentz, Sakulich et al., 2014; Farnam, Todak, Spragg, & Weiss, 2015; Villani, Farnam, Washington, Jain, & Weiss, 2015).

Using PCMs in concrete pavements to melt ice and snow requires specific thermal, physical, and chemical properties to be compatible with the concrete system. The search for a suitable PCM has been directed toward the use of low-melting organic materials. FAME show solid–liquid phase transitions with desirable thermal properties within a narrow temperature range. FAME mixtures can be tailored to include a phase transition temperature that differs from the pure material for the required temperature slightly above 0 °C and high latent energy of fusion (>150 $J \cdot g^{-1}$). FAME's physical properties include low vapor pressure and small volumetric changes during phase transition. FAME are chemically stable, non-toxic, and non-flammable. They are commercially available and are sustainably derived from common vegetable and animal oils providing renewable supply without depending on petroleum (Dunn, 2008; Lockemann & Schluender, 1993; Liston, 2015).

In this study, the thermal properties of two binary mixtures providing the required thermal properties, methyl laurate + methyl myristate (C12-C14) and methyl laurate + methyl palmitate (C12-C16), were investigated using differential scanning calorimetry. Additionally, solid–liquid phase diagrams for each of the binary mixtures were developed providing information on the *liquidus* line, and transitions below the *liquidus* line are reported in this study.

3.1 EXPERIMENTAL

3.1.1 Materials

Methyl laurate (C12:0, 98% pure, CAS: 111-82-0), methyl myristate (C14:0, 98% pure, CAS: 124-10-7), and methyl palmitate (C16:0, 97% pure, CAS: 112-39-0), hereafter referred to as pure, were used for preparation of the binary mixtures. A series of binary mixtures were prepared gravimetrically by heating the methyl esters above their melting point before blending them at various mole fractions within the range of 0.00–1.00.

3.1.2 Composition Analysis

The FAME composition in each mixture was confirmed using a Thermo Scientific TRACE™ Ultra GC equipped with a variable split-flow programmable temperature vaporizing (PTV) injector, temperature programmable oven, a flame ionization detector (FID), and a AS/AI 3000 auto-sampler and auto-injector. The GC operating conditions were configured to follow the standard method, BS EN 14103-2011 (British Standards Institution, 2011), presented in Table 5, using a polar analytical capillary column, EC™-WAX, 30-m length × 0.25-mm inner diameter × 0.25-µm film thickness. ChromQuest™ 4.2 was used for data collection and the analysis of the chromatographs.

Table 5. Gas Chromatograph Operating Conditions

Inlet			Carrier		
Temperature	250 °C		Column Flow (He)	1.4 mL min^{-1}	
Split Flow	70 mL min^{-1} (50:1 ratio)		Flow Mode	Constant	
FID			Oven Program		
Temperature	270 °C		Initial	110 °C	hold 0.5 min
Air Flow	300 mL min^{-1}		Ramp 1	20 °C min^{-1} to 130 °C	hold 0.5 min
H_2 Flow	30 mL min^{-1}		Ramp 2	30 °C min^{-1} to 220 °C	hold 1 min
Make-Up (He) Flow	30 mL min^{-1}		Ramp 3	10 °C min^{-1} to 250 °C	hold 7 min

3.1.3 Thermal Analysis

The heat flow and temperature associated with phase transitions for each mixture were determined using a TA Instruments Q2000 LT-DSC instrument. The thermograms were analyzed using TA Instruments Universal Analysis 2000. Indium was used for the DSC calibration. Dry nitrogen was used for the sample purge gas with the flow rate regulated at 50 mL min^{-1}. A sample (10 ±2 mg) was weighed into a Tzero stainless steel high-volume pan and sealed hermetically. Using the protocol of Costa et al.(2011), the sample was heated at a rate of 5 °C·min^{-1} to 15 °C above the melting temperature of the highest melting temperature component and held for 20 minutes. The cooling thermogram was then recorded by cooling the sample at a rate of 1 °C·min^{-1} to 25 °C below the melting temperature of the lowest melting component. Then, the sample was held isothermally for 30 minutes. The heating thermogram was obtained by increasing the temperature at a rate of 1 °C·min^{-1} to the initial heated temperature. This program was repeated three times for each sample.

The peak top temperatures, the temperatures associated with the point of maximum heat flow, were determined using a Universal Analysis 2000 program of TA Instruments (New Castle, DE) for the melting (T_{melt}), eutectic reaction (T_{eut}), peritectic reaction (T_{peri}), and metatectic reaction (T_{meta}) temperatures. The eutectic, peritectic, and metatectic reactions were identified by an endothermic peak appearing at the invariant reaction's temperature. The peak top temperatures were also used for determining the temperature for phase transitions (T_{trans1}, T_{trans2}, and $T_{trans.pure}$) associated with overlapping peaks to avoid errors on temperature evaluation, a common method for evaluating mixtures of FAME, fatty acids, and fatty alcohols (Dunn, 2008; Maximo et al., 2014; Foon et al., 2006; Carareto, Costa, Rolemberg, Krähenbühl, & Meirelles, 2011; Costa et

al., 2007; Costa et al., 2009a; Costa, et al., 2009b; Costa, Rolemberg, Meirelles, Coutinho, & Krähenbühl, 2009; Carareto et al., 2014; Inoue, Hisatsugu, Yamamoto, & Suzuki, 2004; Inoue, Hisatsugu, Suzuki, Wang, & Zheng, 2004; Inoue, Hisatsugu, Ishikawa, & Suzuki, 2004). The onset temperature (T_{onset}) and end of melting temperature (T_{end}) were measured as the point of intersection from the line tangential to the point of maximum slope and the horizontal baseline. The total enthalpy values (ΔH_{melt}) were obtained by numerical integration of the area under all the peaks in the corresponding heat flow versus temperature curves.

3.2 RESULTS

3.2.1 Mixtures Composition

The composition of each binary mixture and the pure FAME used in this study are presented based on mole fractions in Tables 6 and 7. A particular mixture will be referred to by its methyl laurate mole fraction, such as $\boldsymbol{x}_{C12} \approx 0.77$.

Table 6. Composition of C12–C14 Binary Mixtures [(a)]

C12:0 (mole fraction)	C14:0 (mole fraction)	Others (mole fraction) [(d)]
0.9927[(b)]	0.0017	0.0057
0.9036	0.0913	0.0050
0.8591	0.1372	0.0028
0.8123	0.1822	0.0055
0.7674	0.2273	0.0052
0.7222	0.2762	0.0016
0.6764	0.3214	0.0021
0.6253	0.3731	0.0016
0.5817	0.4164	0.0020
0.5245	0.4722	0.0033
0.4274	0.5601	0.0120
0.3386	0.6592	0.0022
0.2229	0.7756	0.0016
0.1155	0.8839	0.0006
0.0022[(c)]	0.9921	0.0057

[(a)] Values represent an average of at least three replicates. Standard deviations are all less than ±0.010.
[(b)] Pure methyl laurate (C12:0).
[(c)] Pure methyl myristate (C14:0).
[(d)] Others include methyl palmitate, methyl 10-heptadecanoate, methyl stearate, methyl oleate, and methyl linoleate.

Table 7. Composition of C12–C16 Binary Mixtures [a]

C12:0 (mole fraction)	C16:0 (mole fraction)	Others (mole fraction) [e]
0.9927[c]	0.0030	0.0043
0.9034	0.0866	0.0099
0.8163	0.1740	0.0099
0.7243	0.2655	0.0101
0.6344	0.3637	0.0018
0.5443	0.4537	0.0020
0.4569[b]	0.5413	0.0019
0.3462	0.6490	0.0047
0.2525[b]	0.7447	0.0028
0.1275	0.8704	0.0020
0.0000[d]	0.9939	0.0061

[a] Values represent an average of at least three replicates. Standard deviations are all less than ±0.010 unless otherwise noted.
[b] Standard deviations are less than ±0.015.
[c] Pure methyl laurate (C12:0).
[d] Pure methyl palmitate (C16:0).
[e] Others include methyl myristate, methyl stearate, methyl oleate, and methyl linoleate.

3.2.2 Methyl Laurate and Methyl Myristate Binary Mixtures

The melting temperatures, transition temperatures under the *liquidus* line, and enthalpy for each methyl laurate + methyl myristate binary mixture are presented in Table 8. The DSC melting thermograms for a select number of the C12–C14 mixtures are plotted in Figure 9.

Table 8. Melting Temperatures and Enthalpy for C12–C14 Binary Mixture [a]

x_{C12} [b]	T_{onset} (°C)	T_{eut} (°C)	T_{peri} (°C)	T_{meta} (°C)	T_{trans1} (°C)	T_{trans2} (°C)	$T_{trans.pure}$ (°C)	T_{melt} (°C)	T_{end} (°C)	ΔH_{melt} ($J \cdot g^{-1}$)
0.99	4.57						6.49	6.72	7.67	184.50
0.90	−1.44	−0.35		1.00	2.56			4.22	4.96	167.80
0.86	−1.78	−0.23			2.03			3.51	4.14	164.10
0.81	−2.14	−0.43						0.94	2.14	167.13
0.77	−2.14							0.21	1.73	174.30
0.72	−2.06							0.66	2.03	177.83
0.68	−2.04							0.59	2.18	162.70
0.63	−2.01		0.39	1.30				5.43	6.97	166.47
0.58	−2.02		0.56	1.77				7.61	8.58	178.23
0.52	−2.01		0.35	1.41				9.11	10.12	169.13
0.43	−2.22		0.19	0.99	4.94 [c]			11.81	12.84	179.43
0.34	−2.25		−0.13	0.79	7.39 [c]			14.10	15.04	178.77
0.22	−2.30		−0.28	0.62	6.80 [c]	12.46		16.41	17.42	179.97
0.12	−2.76		−0.59	0.17				17.92	18.96	158.13

x_{C12} [b]	T_{onset} (°C)	T_{eut} (°C)	T_{peri} (°C)	T_{meta} (°C)	T_{trans1} (°C)	T_{trans2} (°C)	$T_{trans.pure}$ (°C)	T_{melt} (°C)	T_{end} (°C)	ΔH_{melt} ($J \cdot g^{-1}$)
0.00	18.55						20.48	20.68	22.09 [a]	188.63

[a] Values are an average of at least three replicates. All temperature standard deviations are less than ±0.10, unless otherwise noted. Enthalpy standard deviations are all less than ±2.43 $J \cdot g^{-1}$.
[b] Mole fraction of methyl laurate in the binary mixture.
[c] Temperature standard deviations are less than ±0.37 °C.

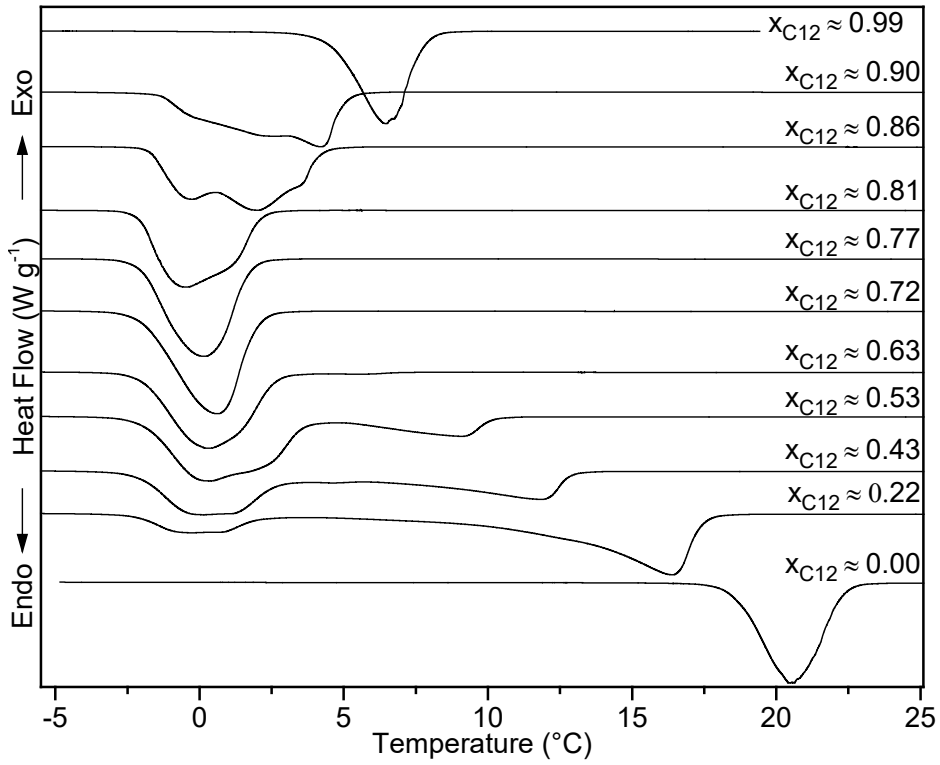

Figure 9. The DSC Melting Curves for Methyl Laurate + Methyl Myristate Binary System

The melting curves show the complex melting behavior of this binary system. The binary mixtures of methyl esters form non-ideal solutions exhibiting freezing point depression. By increasing the methyl myristate composition, the melting temperature of the system decreases, and multiple overlapping peaks form, relating to polymorphic behavior. This allows the mixture to be tuned to a particular temperature.

At the eutectic composition, the solid completely melts at the minimum melting temperature producing a sharp peak within a narrow temperature range where all the energy is absorbed. The eutectic reaction can occur in compositions other than the eutectic composition from the classically defined eutectic point, though still occurring at the eutectic temperature. The endothermic behavior associated with the eutectic reaction appears at compositions only above $\boldsymbol{x}_{C12} \approx 0.63$. The DSC melting curves show the eutectic point for this binary FAME mixture occurs between $\boldsymbol{x}_{C12} \approx 0.77$ and $\boldsymbol{x}_{C12} \approx 0.68$, where there is only a single endothermic peak. The

narrowest temperature range is associated with the eutectic point, $\boldsymbol{x}_{C12} \approx 0.63$ at $T_{M,peak} \approx 0.21$ °C, shown in Figure 10.

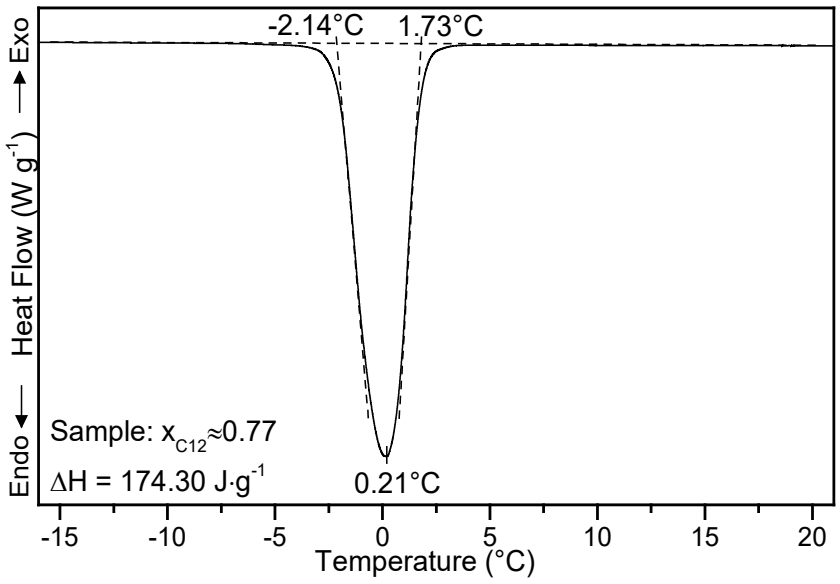

Figure 10. The DSC Thermogram for the Eutectic Composition of C12–C14, $\boldsymbol{x}_{C12} \approx 0.77$

The various other endothermic peaks are related to a peritectic reaction, a metatectic reaction and solid–liquid transitions under the *liquidus* line, and the melting peak. The peritectic, $\alpha + l \leftrightarrows \beta$, reaction is an isothermal, reversible reaction of a solid (α) and liquid (l) phase transforming into a new solid phase (β) during cooling. The metatectic reaction, $\beta \leftrightarrows \alpha + l$, is an isothermal, reversible reaction of a solid mixture phase (β) transforming into a different solid phase (α) plus a liquid (l) during cooling (Gamsjäger, Lorimer, Scharlin, & Shaw, 2008). Below $x_{C12} \approx 0.63$, two endothermic peaks appear, for example for $x_{C12} \approx 0.53$ in Figure 9. The peritectic reaction occurs slightly above the eutectic reaction temperature. The metatectic reaction occurs slightly above the peritectic reaction temperature. Both of these types of reactions have been observed in binary systems of fatty acids and binary systems of FAME (Costa, Boros, Coutinho et al. 2011; Carareto et al., 2011; Costa et al., 2009a; Costa et al., 2009b; Costa Rolemberg, Meirelles, Coutinho, & Krähenbühl,, 2009). The proximity of these two reaction's peak temperatures makes their identification difficult. At temperatures above these two reactions, other solid–liquid transitions occur below the *liquidus* line (Table 8). Further studies of these reactions and transitions can be conducted using X-ray diffraction, but it is out of the scope of this work.

The presence of the eutectic, peritectic, and metatectic reactions are confirmed through the use of a Tammann plot, the enthalpy variation of each reaction plotted as a function of the sample's molar composition (Chernik, 1995). The constructed Tammann plot for methyl laurate + methyl myristate is shown in Figure 11. The linear increase of metatectic, peritectic, and eutectic reaction enthalpy confirms that the endothermic behaviors seen in their thermograms are associated with a reaction rather than a solid–liquid transition (Carareto et al., 2011).

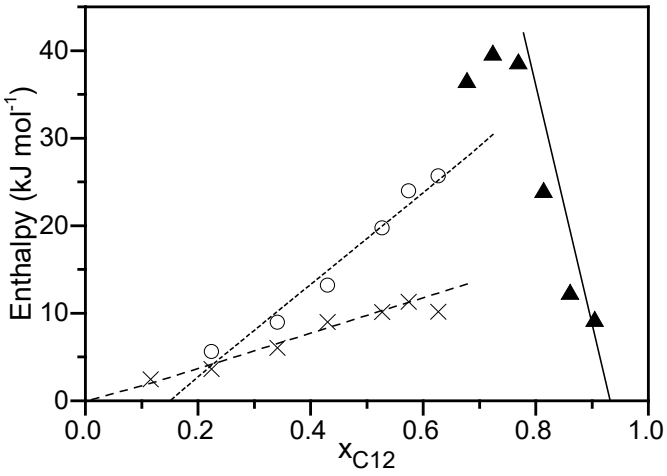

Figure 11. Tammann Plot for Methyl Laurate + Methyl Myristate Binary System: (▲) Eutectic Reaction Enthalpy, (□) Peritectic Reaction Enthalpy, and (×) Metatectic Reaction Enthalpy

For the eutectic reaction, the enthalpy increases to the eutectic point that occurs between $x_{C12} \approx 0.75$and $x_{C12} \approx 0.85$, which agrees with the DSC melting curves. However, significant overlapping of the peritectic and eutectic peaks resulted in indistinguishable points in the Tammann triangle. The two points at $x_{C12} \approx 0.68$ and $x_{C12} \approx 0.72$ are plotted as enthalpy associated with the eutectic reaction. However, the DSC measurements did not provide the resolution necessary to fully confirm that these two points are associated only with the eutectic reaction. Therefore, they were not used in completing the Tammann plot. The broad temperature range in these two compositions indicates that there might be two peaks that have merged together to form one broad peak. Analysis techniques such as X-ray diffraction could further delimit different reaction composition ranges, but it is out of the scope of this work.

The enthalpy decreases away from the invariant points until crossing the axis at the concentration where solid solutions form. With the linear fit of the enthalpy data points, the enthalpy intersects the composition axis at $x_{C12} \approx 0.02$ and $x_{C12} \approx 0.92$. Therefore, below $x_{C12} \approx 0.02$ and above $x_{C12} \approx 0.92$, the two FAME are partially miscible in the solid phase, forming two regions of solid solution.

Each reaction has its own maximum amount of associated enthalpy. The eutectic reaction absorbs/releases the maximum amount of enthalpy, ~40 kJ·mol^{-1}. The peritectic and metatectic reactions produce less enthalpy, ~30 kJ·mol^{-1} and ~11 kJ·mol^{-1}, respectively. Selecting the composition that will have a phase transition associated with the eutectic reaction at the desired temperature range will ensure the maximum amount of energy is used for the PCM.

The solid–liquid phase diagram for methyl laurate + methyl myristate binary system was developed based on the DSC thermograms and the developed Tammann plot, Figure 12. The presences of the eutectic, peritectic, and metatectic reactions divides the phase diagram into 14 different regions: four regions of solid–solid equilibria $C^b + C$, $C^b + C_h^b$, $C^a + C$, and $C^a + C_h^a$; five regions of solid–liquid equilibrium, $C^b + l$, $C_h^b + l$, $C + l$, $C^a + l$, and $C_h^a + l$; and five monophasic regions under the *liquidus* line, C^b, C_h^b, C^a, C_h^a, and C. Where C^a and C^b represent

the solid solution rich in methyl laurate (a) and methyl myristate (b), C_h refers to the solids formed from recrystallization during the metatectic reaction, and C is solids formed by the mixture of the components and l is the liquid phase. The presented phase diagram is comparable to phase diagrams in literature of binary mixtures of fatty acid methyl esters differing by two carbon atoms (Costa et al., 2011).

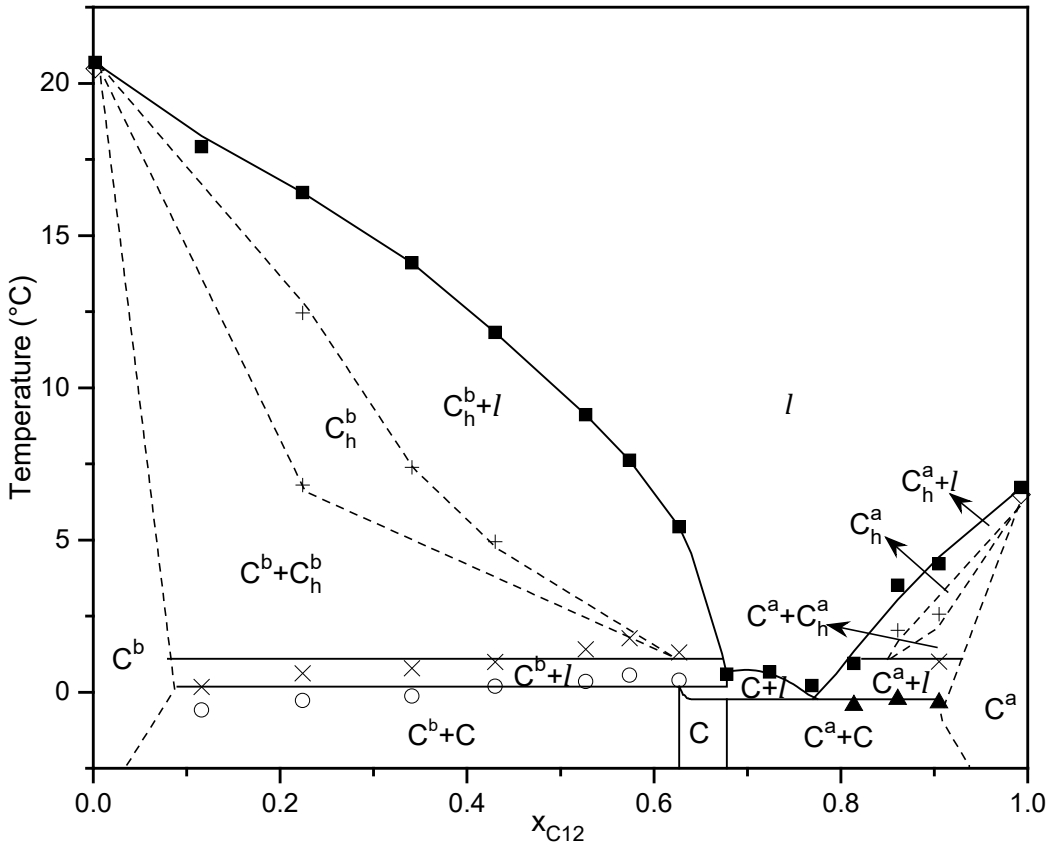

Figure 12. Solid–Liquid Phase Diagram for Methyl Laurate + Methyl Myristate Binary System: (a) Methyl Laurate, (b) Methyl Myristate, (■) Melting Temperature, (□) Eutectic Temperature, (□) Peritectic Temperature, (□) Metatectic Temperature, (+) Solid-s.

The methyl laurate + methyl myristate system produces a PCM with desirable thermal properties for low-temperature applications at $x_{C12} \approx 0.77$; this PCM has a melting temperature of 0.21 °C and enthalpy of fusion of 174.3 J·g^{-1}. These binary mixtures displayed a slight amount of supercooling during freezing; this is an important factor to keep in mind when selecting the appropriate binary composition for the PCM (Farnam, Esmaeeli, Bentz, & Zavattieri, 2015). Therefore, a binary mixture with a slightly higher melting temperature could be more desirable to reduce the amount of ice and snow on the surface of concrete.

The C12–C16 melting curves display a simpler melting behavior compared to the C12–C14 melting curves, Figure 13. There are two well-defined peaks in the C12–C16 system: one attributed to the eutectic reaction and the other with the melting point of the mixture. With the increase in methyl palmitate concentration in the system, the melting point decreases, and a low

melting peak appears, corresponding to the eutectic reaction. The eutectic peak is observed in all of the examined binary mixtures. The eutectic point occurs between $x_{C12} \approx 0.91$ and $x_{C12} \approx 0.82$, where there is a shift from the majority of the sample associated with the melting peak to the eutectic peak. Between compositions $x_{C12} \approx 0.73$ and $x_{C12} \approx 0.47$, Table 9, there are two small solid–liquid endothermic peaks near ~9 °C and ~12 °C.

Table 9. Melting Data for Methyl Laurate + Methyl Palmitate DSC Curves

x_{C12}	T_{onset} (°C)	T_{eut} (°C)	T_{trans1} (°C)	T_{trans2} (°C)	$T_{trans.pure}$ (°C)	T_{melt} (°C)	T_{end} (°C)	ΔH_{melt} ($J \cdot g^{-1}$)
0.99	4.57				6.49	6.72	7.67	184.50
0.91	1.07	1.86				3.91	5.04	190.10
0.82	−0.01	2.17				6.65	9.88	167.73
0.73	0.52	2.79	9.09	11.31		13.49	15.13	178.60
0.64	0.44	2.59	9.11	13.12		17.05	18.89	179.50
0.56	0.38	2.44	9.37			20.15	21.95	182.67
0.47	0.24	2.36	9.42			22.84	24.51	185.13
0.36	−0.02	2.03				25.22	26.65	196.87
0.26	−0.47	1.62				27.09	28.54	200.83
0.13	−1.90	1.10	2.58			28.93	30.25	201.93
0.00	29.21				31.76	31.93	33.15	207.73

Values are an average of at least three replicates. All temperature standard deviations are less than ±1.00 °C, unless otherwise noted. Enthalpy standard deviations are all less than ±0.91 J g^{-1}.

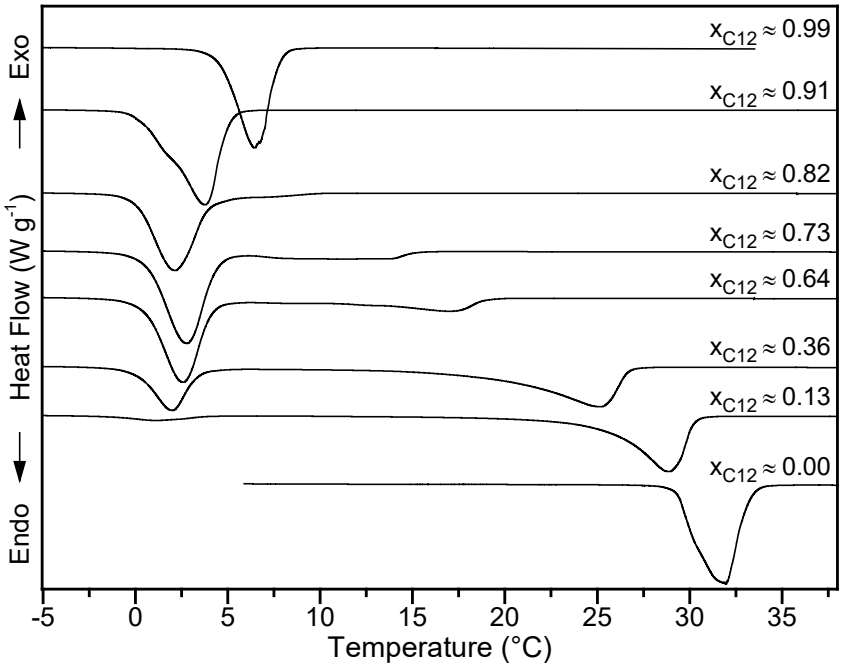

Figure 13. The DSC Melting Curves for Methyl Laurate + Methyl Palmitate Binary System

A Tammann plot was developed for the methyl laurate + methyl palmitate binary system for the eutectic reaction and the small endothermic peaks, Figure 14. As expected, the enthalpy linearly increases with the increase in methyl laurate concentration up to the eutectic concentration before decreasing linearly, confirming this endothermic behavior is associated with a reaction. The intersection of the two linear fit lines for the eutectic enthalpy denotes the eutectic composition at approximately $x_{C12} \approx 0.86$ at about ~37 kJ·mol^{-1} (166.5 J·g^{-1}). These lines intersect with the composition axis at $x_{C12} \approx 0.01$ and $x_{C12} \approx 1.00$. Therefore, these FAME are only miscible at low concentrations of methyl laurate, forming solid solutions below $x_{C12} \approx 0.01$.

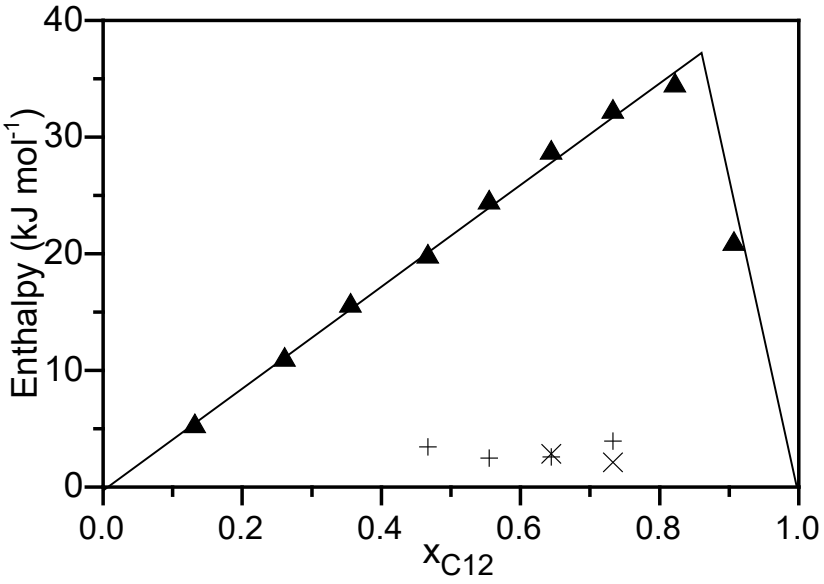

Figure 14. Tammann Plot for Methyl Laurate + Methyl Palmitate Binary System: (▲) Eutectic Reaction Enthalpy, (+) Enthalpy for Transitions at ~9 °C, (×) Enthalpy for Transition at ~12 °C

The enthalpy associated with the endothermic behavior near 9 °C and 12 °C, Figure 14, did not display an increasing linear behavior, confirming that this thermal behavior is related to solid–liquid transitions under the *liquidus* line and not a peritectic or metatectic reaction.

The solid–liquid phase diagram for methyl laurate + methyl palmitate binary system was developed based on the DSC melting thermograms and the developed Tammann plot, Figure 15. The presence of the eutectic reaction divided the phase diagram into four different regions: two solid–liquid equilibrium regions $C^b + l$ and $C^a + l$; and two monophasic regions under the *liquidus* line C and C^b, where C^b represents a solid solution rich in methyl palmitate and C represents the solids formed by a mixture of the components. The developed phase diagram is comparable to other phase diagrams for binary mixtures of fatty acid methyl esters differing by four carbon atoms (Costa et al., 2011).

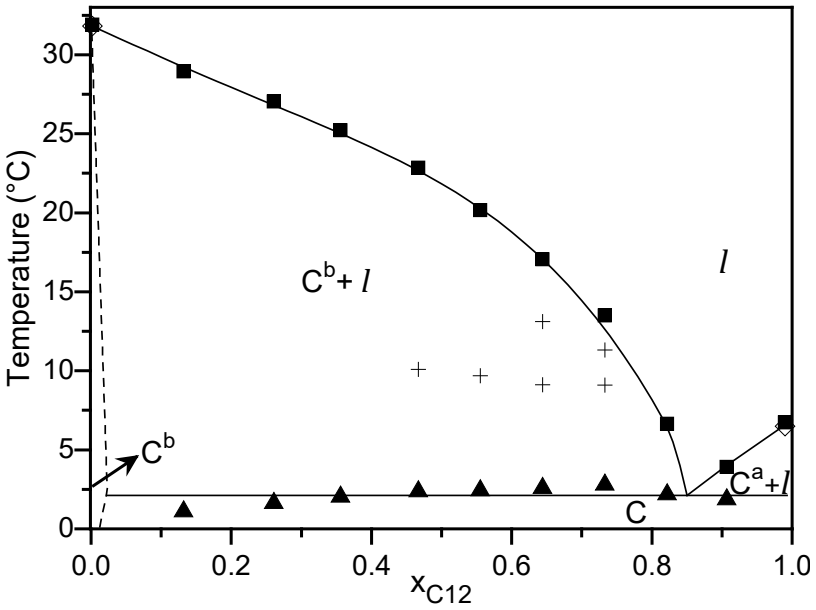

Figure 15. Solid-Liquid Phase Diagram for Methyl Laurate + Methyl Palmitate Binary System: Methyl Laurate (■) Melting Temperatures, (◇) Pure Transition Temperature, (▲) Eutectic Reaction Temperature, (+) Solid-Liquid Transition Temperature [(—) and (---) are guides for the eyes.]

The eutectic isotherm occurs at ~2.4 °C. The system's eutectic point occurs at a molar concentration of $x_{C12} \approx 0.86$. The solid solution forms at $x_{C12} \approx 0.01$ but not at the other end of the phase diagram. The solid–liquid transitions occur near 9 °C and 12 °C between $x_{C12} \approx 0.47$ and $x_{C12} \approx 0.73$.

The methyl laurate + methyl palmitate system presents thermal properties desirable for low-temperature applications at the approximate eutectic point of $x_{C12} \approx 0.86$ with an estimated melting temperature of ~2.4 °C and enthalpy of fusion of ~166.5 J·g^{-1}. The slightly higher melting temperature could prove beneficial in reducing the accumulation of ice and snow on the surface of concrete (see Figure 15).

The differences in the fatty acid methyl ester's chain length plays an important part in the solid–liquid phase behavior in binary systems. Presented in this study, systems differing by two carbon atoms display a complex melting behavior, whereas systems differing by four carbon atoms display a simple eutectic behavior. This chain length dependence has been reported before and also plays a role in the solid–liquid behavior of binary fatty acid systems (Costa et al., 2011; Inoue et al., 2003a; Inoue et al., 2004; Inoue et al., 2003b). As the chain length differences continue to increase, the system's components become more incompatible; therefore, FAME systems differing by six or eight carbon atoms could present a monotectic-type phase diagram. Inoue et al. (2003a) and Inoue et al. (2003b) noted the shift from eutectic phase diagrams to monotectic phase diagrams as the temperature differences increased in binary systems of fatty acids with oleic acid.

3.3 CONCLUSION

Binary mixtures of fatty acid methyl esters provide desirable thermal properties for use as low-temperature PCMs to improve anti-icing practices. Specifically, methyl laurate + methyl myristate and methyl laurate + methyl palmitate binary mixtures at their eutectic compositions are promising sustainable PCMs with melting temperatures of 0.21 °C and 2.4 °C and the latent heat of fusion of 174.3 $J \cdot g^{-1}$ and 166.5·J g^{-1}, respectively. The developed phase diagrams provide valuable information about the thermal properties at a range of methyl ester compositions. This information can be used in mathematical model development for simulating the anti-icing behaviors of these PCMs in concrete. Additionally, a proper incorporation method of the developed binary fatty acid methyl esters mixtures into the concrete system is required for effective utilization of the material as a PCM to reduce ice and snow without damaging the concrete pavement.

4. EVALUATING THE USE OF PCMs IN CONCRETE PAVEMENT TO MELT ICE AND SNOW

PCMs have the potential to be used to store thermal energy from ambient, solar, or applied heat sources (Kalnæs & Jelle, 2015; Ling & Poon, 2013). Organic PCMs are classified as paraffin and non-paraffin (Kalnæs & Jelle, 2015). Most organic PCMs do not require undercooling to provide nucleation during freezing and are generally noncorrosive; both desirable characteristics for concrete pavement applications (Abhat, 1983; Hawes, Banu, & Feldman, 1992; Regin et al., 2008; Sharma, Tyagi, Chen, & Buddhi, 2009). Inorganic PCMs are classified as salt hydrates and metallic. Metallic PCMs are not within the desired temperature range for building applications (Kalnæs & Jelle, 2015). The salt hydrates can corrode metals, need to be supercooled to induce freezing due to poor nucleating properties, experience phase segregation and thermal property alterations after multiple freeze-thaw cycles due to release/gain of water, and can interact with the cementitious binder (Abhat, 1983; Kalnæs & Jelle, 2015; Ling & Poon, 2013; Shi, Fay, Peterson, Berry, & Mooney, 2011; Sutter et al., 2008). Eutectics of organic and inorganic compounds are a minimum-melting composition of two or more components that freeze and melt congruently, forming mixtures of component crystals (Sharma et al., 2009) that can allow for the design of a particular mixture of organic or inorganic PCMs to create optimum operating temperatures in concrete pavement applications (Kalnæs & Jelle, 2015; Karaipekli, & Sari, 2008; Lane, 1989; Sharma et al., 2009).

PCMs have been conventionally used in solar water-heating systems, greenhouses, building walls and floors, window shutters, concrete to mitigate thermal cracking, and mass concrete (Abhat 1983; Choi, Khil, Chae, Liang, & Yun, 2014; Fernandes et al., 2014; Hembade, Neithalath, & Rajan, 2014; Kuznik & Virgone 2009; Regin et al. 2008; Sharma et al. 2009; Whiffen & Riffat 2012). PCMs have been proposed to be used in the concrete infrastructure to alter anti-icing practices in concrete pavements (Bentz & Turpin 2007; Ling & Poon 2013; Liston et al. 2014; Sakulich & Bentz 2012a, 2012b). Due to the PCM's high heat of fusion, the stored energy can be released during a freezing/icing event, thereby delaying or preventing ice formation (Liston et al. 2014; Sakulich & Bentz 2012a, 2012b). This can help decrease or eliminate the need for deicing salt to melt ice or snow on the surface of concrete pavements. Deicing salts can cause premature deterioration in concrete pavement, and any decrease in salt use can improve the durability of concrete (Farnam , Bentz, Hampton, & Weiss, 2014;Farnam,

Bentz, Sakulich et al., 2014; Farnam, Todak, Spragg, & Weiss, 2015; Farnam, Wiese, Bentz, et al., 2015; Qian, Farnam, & Weiss, 2014).

Figure 16 shows a schematic of using PCMs in concrete pavement to melt ice and snow (Memon, Cui, Zhang, & Xing, 2015; Sakulich & Bentz 2012a, 2012b). Using PCMs in the concrete infrastructure requires specific thermal, physical, and chemical properties that are compatible with the concrete. The desirable thermal properties of a PCM for successful use in the concrete pavement to melt ice and snow include a phase transition temperature slightly above 0 °C, high latent heat of fusion, high specific heat (heat capacity), and high thermal conductivity (Bentz & Turpin, 2007; Ling & Poon, 2013; Sakulich & Bentz, 2012a, 2012b). The PCM's physical properties should include high density, small volume change between phases, and low vapor pressure. The PCM's chemical properties should include stability and compatibility with concrete, and they should be non-toxic and non-flammable (Hawes, Banu, & Feldman, 1992; Liston et al., 2014). PCMs that are economical, commercially available, and environmentally friendly are also important.

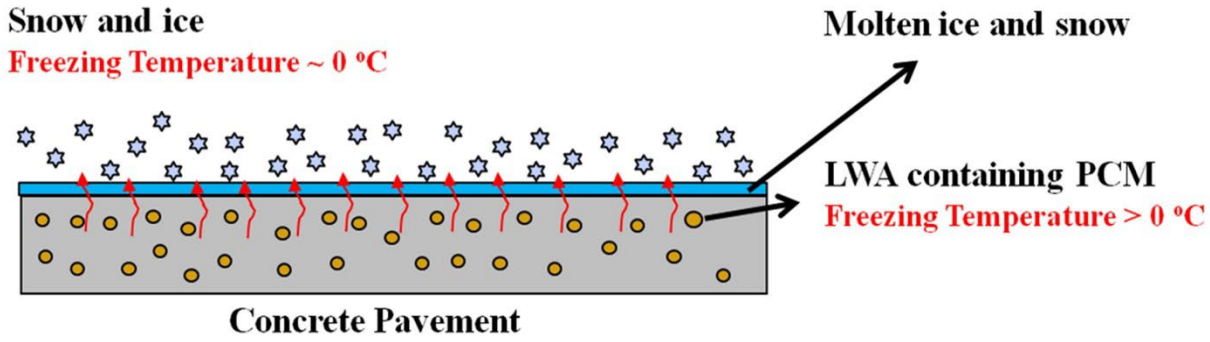

Figure 16. Using PCM in Concrete Pavement to Melt Ice and Snow Using LWA

The use of PCMs in concrete pavement application requires an efficient method to place PCMs into the concrete pavement without extensive changes to the construction practice. Different methods have been proposed to use PCM in concrete elements (Hawes & Feldman, 1992; Hawes, Banu, & Feldman, 1992; Sakulich & Bentz, 2012a). Figure 17 shows three of those methods: (a) filling tubes with PCM to raise the latent heat of the concrete-tube system preventing freezing of ice or snow accumulation on the concrete pavement (Velraj & Pasupathy, 2006); (b) incorporating the PCM directly using LWA or encapsulated PCM in the concrete pavement (Chen, Cao, Shan, & Fang, 2013; Sakulich & Bentz, 2012a; Tyagi, Kaushik, Tyagi, & Akiyama, 2011); and (c) the inclusion of PCM within the concrete pores and voids on the surface of the pavement. The last method has also been used for applying sealants to pavement surface (Jones et al., 2013).

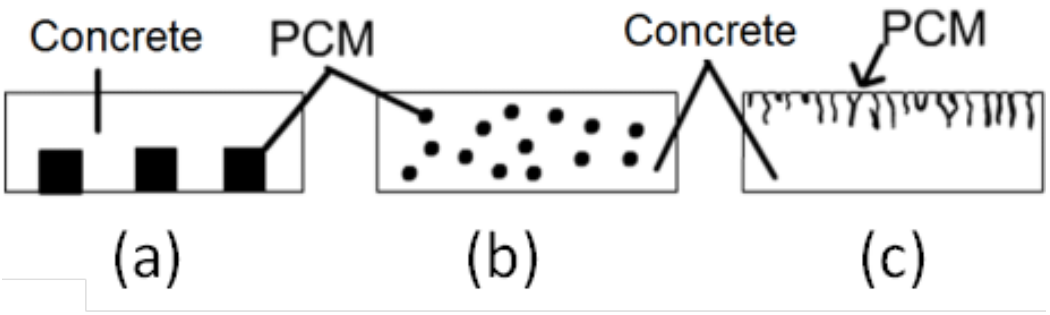

Figure 17. Three Methods of Incorporating a PCM Into Concrete: (a) Using Pipes of PCM, (b) Using Particles Containing PCM, and (c) Filling Concrete Surface Voids via PCM Absorption

Previous researchers (Bentz & Turpin, 2007; Ling & Poon, 2013; Liston et al., 2014; Sakulich & Bentz 2012a, 2012b; Stoll, Drake, & Salyer, 1996) have shown that PCMs have the potential to change deicing and snow-removal practice in concrete pavement and that they can be used to decrease the number of freeze-thaw cycles in concrete pavement, thereby increasing concrete freeze-thaw durability. Previous research has primarily characterized the thermal properties of PCMs themselves for concrete pavement applications using a low-temperature differential scanning calorimeter (Abhat, 1983; Bentz & Turpin, 2007; Liston et al., 2014) and predicted the PCM concrete performance to prevent ice formation by means of a numerical simulation (Sakulich & Bentz, 2012a). In a few cases, some durability and physical stability aspects were addressed (Hawes et al., 1992; Sakulich & Bentz 2012b).

4.1 EXPERIMENTAL PROGRAM

Mortar specimens were prepared containing paraffin oil and methyl laurate as PCMs. Two approaches were selected to incorporate PCMs into the mortar specimens: (1) using LWA, and (2) using an embedded tube.

An LT-DSC (Farnam, Bentz, Hampton, & Weiss, 2014; Villani et al., 2015), TA Q2000 with an operating range of −90 °C to 550 °C, was used to determine the thermal properties of the PCMs. An LGCC (Farnam, Bentz, Sakulich et al., 2014) was also used to evaluate the thermal response of mortar specimens containing PCMs during cooling and heating. The durability and stability of PCMs in mortar specimens were determined by (a) evaluation of the chemical reactions between PCMs and mortar constituents using LT-DSC, (b) evaluation of physical properties of the mortar using ultrasonic pulse velocity and compressive strength measurements, and (c) determination of PCM mass loss over time.

4.1.1 Materials

Two types of Ordinary Portland cement (OPC) were used: Type I and Type V with a Blaine fineness of 375 m^2/kg and 316 m^2/kg, respectively. Table 10 indicates the chemical composition of the cements, as reported by the manufacturers. An expanded shale LWA was used in this study. These aggregates were manufactured by Buildex in their Marquette plant with a fineness modulus of 2.94 and a specific gravity of 1.5 (Castro, Keiser, Golias, et al., 2011; Miller et al., 2014). Table 11 shows the properties of the LWA. The absorption of PCMs into LWA was

evaluated using two different conditions: ambient and vacuum conditions (Liston et al., 2014; Zhang, Li, Zhou & Wu, 2004). Two types of PCMs were used: (1) paraffin oil, which is a petroleum-based material with a specific density of 0.77; and (2) methyl laurate, which is a vegetable-based material with a specific density of 0.87. Both PCMs have a vapor pressure less than 0.01 mm Hg.

Table 10. Properties of OPC

Item	Percent by mass (%)	
	Type I	**Type V**
Silicon Dioxide (SiO_2)	19.43	21.3
Aluminum Oxide (Al_2O_3)	5.39	2.6
Ferric Oxide (Fe_2O_3)	3.18	4.2
Calcium Oxide (CaO)	63.45	63.2
Magnesium Oxide (MgO)	2.97	4.5
Sulfur Trioxide (SO_3)	3.38	2.8
Loss on Ignition	0.88	1.20
Sodium Oxide (Na2O)	0.35	NA*
Potassium Oxide (K2O)	0.77	NA*
Free Lime	NA*	0.38
Insoluble Residue	0.25	0.18
Total Equivalent Alkali as Na_2O	0.86	0.21
Tricalcium Silicate (C_3S)	60	64
Dicalcium Silicate (C_2S)	10	13
Tricalcium Aluminate (C_3A)	9	0
Tetracalcium Aluminoferrite (C_4AF)	10	13

* Not available

Table 11. Gradation and Absorption for LWA

Specimen	Sieve Number	Mass Retained (mass %)	Water Vacuum Absorption (mass %)	PCM Vacuum Absorption (mass %)	PCM Ambient Absorption, 24 h (mass %)
Graded LWA	4	1.8	NA*	23	13
	8	13.3	35	28	16
	16	28.4	33	27	20
	30	22.7	31	27	20
	50	13.6	29	23	19
	Pan	20.2	26	NA*	NA*
Mixed LWA			32 ±0.5	NA*	18.8 ±0.5

*Not available

4.1.2 Specimen Preparation and Conditioning

4.1.2.1 Use of LWA to Incorporate PCMs in Mortar

Mortar mixtures were prepared with an aggregate volume fraction of 55% and a water-to-cement ratio (*w/c*) of 0.42 by mass. To prepare mortar, oven dry LWAs were soaked in PCMs for 24 hours. After saturation with PCM, the PCM on the surface of LWAs was removed using a centrifuge technique (Miller et al., 2014) to reach the SSD condition. The aggregate was placed in a centrifuge bowl of known mass; the centrifuge bowl was then placed in the centrifuge, covered with a 4-µm filter and lid, and tightened into place; the centrifuge was then powered on and the test was run for 3 minutes at a speed of 2,000 rpm (Miller et al., 2014).

Mortar was prepared in a standard mortar mixer using LWAs containing PCMs in SSD condition in accordance with ASTM C305-12 (ASTM International, 2012). Mortar was also prepared using LWAs saturated with water (in SSD condition) as a control mortar. The mass of cement, mixing water, and LWA (in SSD condition) were 593 kg, 249 kg, and ~ 940 kg/m^3 of total material volume, respectively, providing 145–150 kg/m^3 of PCM in the mortar. The mortar was cast in 25.4 mm × 25.4 mm × 300 mm (1 in. × 1 in. × 11.81 in.) molds and the specimens were unmolded after 24 hours. All mortar bars were then sealed in double plastic bags and cured for 28 days in these sealed conditions at 23 °C ±0.5 °C. After 28 days of curing, the mortar bars were cut using a wet saw to 25.4 mm × 25.4 mm × 50.8 mm (1 in. × 1 in. × 2 in.) specimens. These specimens were then placed in a chamber at 23 °C ±1 °C and a relative humidity of 50 % ±1 for 7 days to remove moisture prior to the LGCC experiment.

The mortar was also cast in 50.8 mm × 50.8 mm × 50.8 mm (2 in. × 2 in. × 2 in.) molds to determine its compressive strength. These specimens were unmolded after 24 hours and were then sealed and cured for 56 days at 23 °C ±0.5 °C before the compression test.

4.1.2.2 Use of Embedded Tube to Incorporate PCM in Mortar

A plastic tube with a diameter of 10 mm and a length of 50.8 mm was located longitudinally in the center of the 25.4 mm × 25.4 mm × 50.8 mm (1 in. × 1 in. × 2 in.) mold. Mortar was then prepared and cast in the prepared mold. The mortar had a fine aggregate (i.e., natural sand) volume fraction of 55% and a *w/c* of 0.42 by mass. The specimens were demolded after 24 hours. The specimens were cured for 28 days in a sealed condition at 23 °C ±0.5 °C. After 28 days of curing, the specimens were placed in a chamber at 23 °C ±1 °C and a relative humidity of 50 % ±1 for 7 days to remove water moisture. The embedded tube was then filled using PCMs and the top and bottom of the embedded tube were sealed using plastic tape. Approximately, 105–125 kg/m^3 of PCMs were incorporated into the mortar specimens using the embedded tube. The specimens were then tested in an LGCC experiment. To evaluate the chemical reactivity of the plastic tube with PCM, a piece of plastic tube was immersed in a beaker containing PCM for a week and the mass change in the plastic piece was monitored; no mass change or change in plastic stiffness was observed during the immersion time.

4.1.3 Testing Procedure

4.1.3.1 Low-Temperature Differential Scanning Calorimetry

To determine the thermal properties of PCMs, LT-DSC was used. The heat flow and temperature associated with phase transitions in these materials were obtained. High-volume, stainless-steel, pans, specifically 100-µL specimen size TA high-volume pans with hermetic lids were used to contain the specimens. The initial temperature of the test was set to equilibrate at 40 °C for 10 minutes. After the initial temperature became stable, the LT-DSC cell was cooled to -80 °C at a cooling rate of 5 °C/min. The temperature of the specimen was then increased to 40 °C, again at a rate of 5 °C/min. The mass of a specimen was 11 mg ±2 mg.

4.1.3.2 Longitudinal Guarded Comparative Calorimetry

LGCC was used to determine the thermal response of a mortar specimen containing PCM during cooling and heating (Farnam, Bentz, Hampton, & Weiss, 2014, Farnam, Bentz, Sakulich et al., 2014). Mortar specimens (25.4 mm × 25.4 mm × 50.8 mm) containing PCM through either LWA or an embedded tube were tested in the LGCC device. A temperature gradient was generated in the test specimen to produce a one-dimensional heat flow. Two-meter bars with known thermal properties were used on the top and bottom of the mortar specimens; and temperatures at different locations were monitored to calculate the heat flow within the specimens.

The temperature of mortar specimens was varied from 24 °C to -40 °C by using a two-stage cold plate (Cascade CCP-22). The cooling and heating rates were -2 °C/h and 4 °C/h, respectively. At 24 °C and -40 °C, the temperature was kept constant for 1 hour and 4 hours, respectively, to allow the specimen to reach thermal equilibrium. The test was complete after one cycle.

4.1.3.3 Chemical and Physical Durability Assessment

Durability and stability of PCMs in mortar specimens were determined by.

a) an evaluation of chemical reactions between PCM and mortar constituents using LT-DSC,
b) an evaluation of physical properties of mortar using pulse velocity and compressive strength measurements, and
c) a determination of neat PCM mass loss over time.

It was shown that LT-DSC can be used to perform a calorimetry study to assess the chemical reaction between the cementitious matrix and reactive materials at different temperatures (Farnam, Bentz, Hampton, & Weiss, 2014; Farnam, Villani, Washington et al., 2016; Villani et al., 2015). Ground powder specimens were selected for this test since it is intended only to evaluate the potential reactivity of mortar constituents with PCMs. Mortar constituents consisted of LWA, hydrated cement paste for both Type I and Type V cement, and calcium hydroxide. During the test the temperature cycles ranged from 25 °C to -90 °C in the cooling path and from -90 °C to 70 °C in the heating ramp at a rate of a 5 °C/min. The powder (9 to 11 mg) was mixed with an equal mass of PCMs in a high-volume, stainless-steel pan and tested four times in LT-DSC: immediately after mixing (0 days), 1 day after mixing, 7 days after mixing, and 28 days

after mixing. The change in enthalpy of fusion over time, which can indicate a chemical reaction between mortar constituents and the PCM, was monitored.

Acoustic emission testing has shown promising performance for assessing the damage development in cementitious materials (ASTM International, 2009; Farnam, Bentz, Hampton, & Weiss, 2014;, Farnam, Geiker, Bentz et al., 2015a). To evaluate the dynamic elastic modulus of mortar specimens, compressional wave speed (pulse velocity) was measured through the length of the specimens using a pulsed wave generated by two coupled acoustic emission (AE) sensors in accordance with ASTM C597-09 (ASTM International, 2009) The dynamic elastic modulus was compared to the one obtained from a control mortar specimen to measure the damage index. Compressive strength measurements were also performed in accordance with ASTM C109/C109M-13 (ASTM International, 2013a) to evaluate the strength of mortar specimens containing PCM. To evaluate the potential mass loss over time, ~10 grams of PCMs were stored in a beaker and kept in a chamber at 23 °C ±1 °C and a relative humidity of 50 % ±1 for 38 days and the specimen mass was monitored during this time.

4.2 THERMAL PROPERTIES OF PCM RESULTS

Figure 18(a) shows the heat flow measurements obtained using the LT-DSC for both paraffin oil and methyl laurate. The heating ramp is shown, and the result is normalized by the mass of PCM. In addition, the heat released during the phase transformation is calculated and shown in Figure 18(b). Methyl laurate shows one endothermic behavior (i.e., one peak) at a temperature near 1.9 °C (which indicates the liquid/solid phase transformation) with an enthalpy of fusion of ~ 160.4 J/g. Paraffin oil shows two endothermic peaks at temperatures near -28.4 °C and 2.9 °C with enthalpies of ~ 15.4 J/g and 129.4 J/g, respectively. For paraffin oil, the phase transformation (at ~ -28.4 °C) might not be useful in snow melting and deicing applications, since ice and snow melt at a temperature near 0 °C. For a PCM to have good performance in snow melting and deicing applications, it is necessary that the PCM has a phase transformation temperature (most importantly the onset temperature) somewhat greater than 0 °C and a high enthalpy of fusion (Bentz & Turpin, 2007; Ling and Poon 2013; Sakulich & Bentz, 2012a; 2012b). Both paraffin oil and methyl laurate show reasonable thermal properties for snow melting and deicing applications since they can produce a sufficient heat (~130-160 J/g) during their phase transformation at ~2 °C–3 °C.

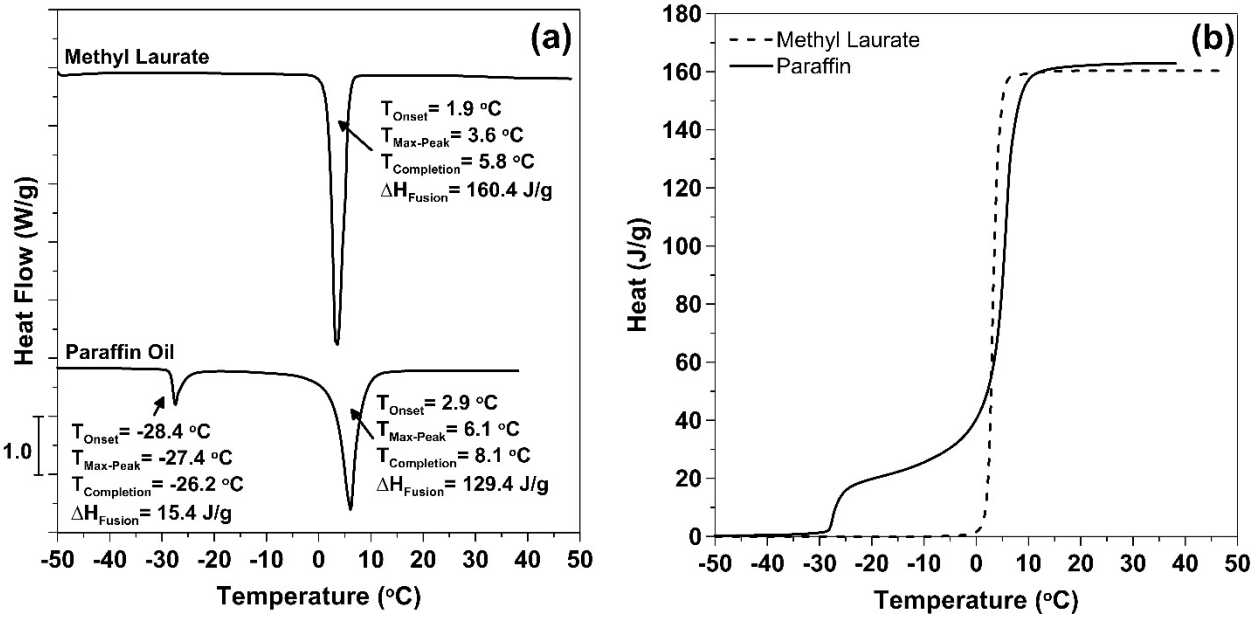

Figure 18. Thermal Responses of Paraffin Oil and Methyl Laurate Obtained Using LT-DSC (normalized per gram of PCM): (a) Heat Flow Versus Temperature and (b) Heat (Enthalpy) Versus Temperature

4.3 THERMAL RESPONSE OF MORTAR CONTAINING PCMs

4.3.1 Using LWA to Incorporate PCM in Mortar

The LGCC was used to perform thermal cycling on mortar specimens. The heat flow was calculated (Farnam, Bentz, Sakulich et al., 2014) during cooling and heating for mortar specimens containing PCM using the LWA approach and is shown in Figure 19. For Figure 19(a), the Type I cement was used to prepare mortar specimens, while the Type V cement was used to prepare mortar for Figure 19(b). Mortar specimens containing paraffin oil show heat release (an exothermic peak) during cooling associated with the paraffin oil phase transformation (i.e., freezing or solidification) and heat absorption (endothermic peak) during heating associated with paraffin oil melting. The heat release during paraffin oil solidification (freezing) can be used to melt ice and snow on the surface of the concrete pavement.

Mortar specimens containing methyl laurate did not release/absorb a significant/measurable amount of heat during cooling/heating for specimens prepared using Type I cement in the temperature range tested. This is partially solved when Type V cement is used to prepare the mortar specimen containing methyl laurate, since a melting peak can be seen during heating. It may be hypothesized that methyl laurate interacts with the cementitious matrix producing a material that is not beneficial to produce heat in the desired temperature range for snow melting and deicing salt applications. The reaction might be milder for mortar specimen prepared using Type V cement than the ones prepared using Type I cement. The reaction between methyl laurate and the concrete constituents and its influence on concrete properties will be described further in Section 4.4.1.

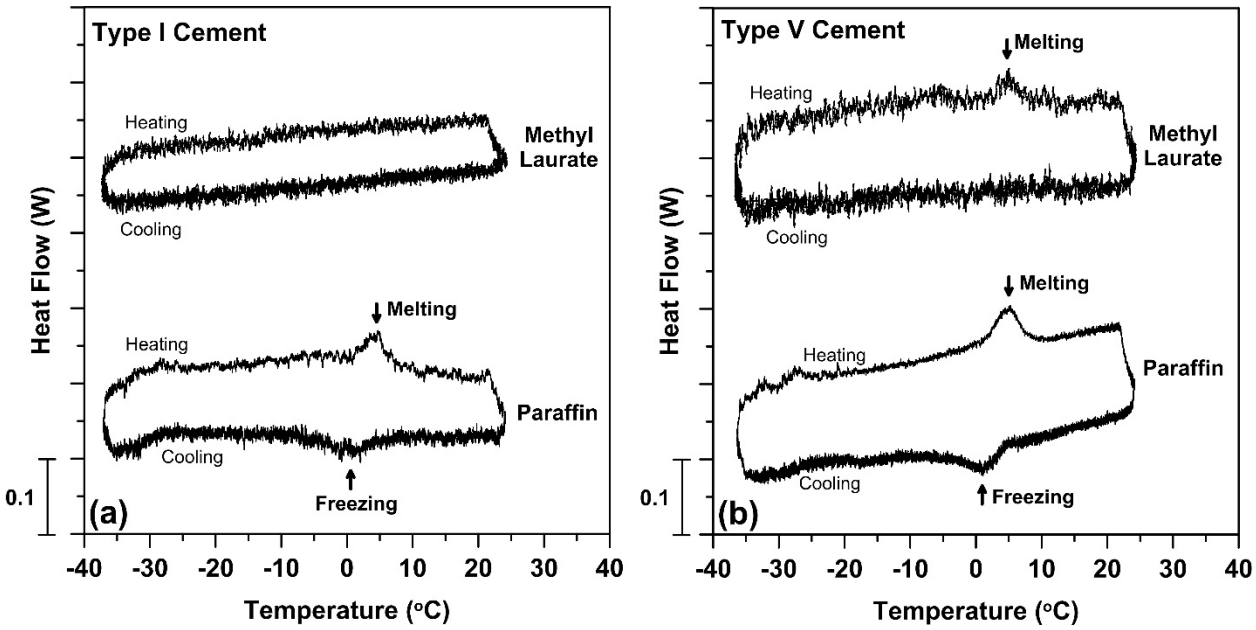

Figure 19. Heat Flow as a Function of Temperature Obtained Using LGCC for Mortar Containing PCM Using LWA: (a) Mortar Prepared Using Type I Cement and (b) Mortar Prepared Using Type V Cement

4.3.2 Using an Embedded Tube to Incorporate PCM in Mortar

Figure 20 shows that methyl laurate might interact with the cementitious matrix when the LWA is used to place PCM in the mortar specimens. When PCM is placed in the LWA, there is no barrier between PCM and different mortar constituents (such as calcium hydroxide, aluminate phases, and aggregates). As a result, PCM might interact with different mortar constituents that can produce a material that is not beneficial in melting ice and snow. Section 4.4.1 shows that this reaction is destructive and can cause cracking in the mortar specimens. The embedded tube/pipe can be an alternative approach to incorporate PCM in concrete elements. A non-reactive plastic or steel tube/pipe can be used to store PCM in concrete and prevent direct contact between the PCM and concrete constituents.

Figure 20 shows heat flow during cooling and heating as a function of temperature for mortar specimens containing PCM using the embedded tube approach obtained from the LGCC experiment. An exothermic phase transformation (freezing peak) and an endothermic phase transformation (melting peak) can be seen for both methyl laurate and paraffin oil. The exothermic phase transformation (i.e., heat release) during PCM solidification (i.e., phase transformation) can be used to melt ice and snow. The released heat can be further restored and recovered in PCM during PCM melting within the (subsequent) heating process.

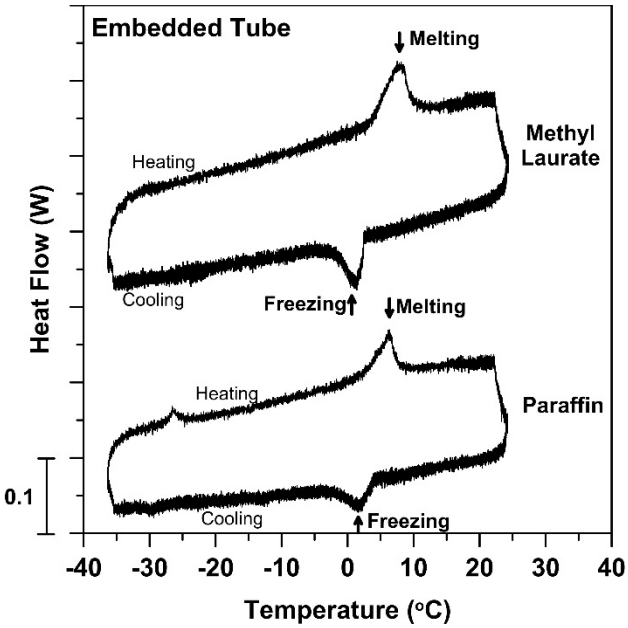

Figure 20. Heat Flow as a Function of Temperature Obtained Using LGCC for Mortar Specimens Containing PCM Through Embedded Tube

4.4 PERFORMANCE OF MORTAR CONTAINING PCM TO MELT ICE

The area under the heat flow versus time curve can be used to quantify the amount of heat that is released or absorbed (stored) during a phase transformation (freezing or melting). The total amount of heat release during PCM solidification was calculated for the mortar specimens tested with the LGCC experiment and is shown in Table 12.

Table 12. The PCM Potential to Release Heat and Melt Ice During Phase Transformation in Mortar Specimen Obtained Using LGCC Experiment

PCM Incorporation Method	PCM Type	PCM Quantity (kg/m^3)*	Heat Release (J/g_{PCM})	Heat Release (kJ/m^3)*	Calculated Molten Ice (kg/m^3)*	Ice-to-Concrete Depth Ratio (%)
LWA**	Methyl Laurate	150	–	–	–	
	Paraffin Oil	145	78.4 (±1.3)	11345 (±188)	34.0 (±0.5)	3.7 (±0.1)
Embedded Tube	Methyl Laurate	122.0 (±3.8)	98.0 (±6.8)	12111 (±1070)	36.3 (±3.2)	4.0 (±0.3)
	Paraffin Oil	111.7 (±4.3)	66.9 (±9.9)	7430 (±827)	22.3 (±2.5)	2.4 (±0.3)

* Per cubic meter of mortar specimen.
** The average value for samples prepared using both Type I and Type V are reported.
Note: the results are reported ± one standard deviation for at least two replicates of LGCC experiment.

A desirable amount of heat is released during PCM phase transformation (i.e., freezing) that can be further used to melt ice or snow. It was reported that the heat release measured using the LGCC experiment is approximately 40% less than the actual heat release during phase transformation in the mortar specimen tested in the LGCC due to the heat loss experienced during the LGCC experiment (Esmaeeli et al. 2015). As a result, the actual heat release could be much higher than the values reported in Table 12.

The temperatures at which the phase transformation begins, or ends were obtained during the LGCC experiment and are reported in Table 13. It should be mentioned that the onset temperature at the bottom surface of the specimen in the LGCC experiment may be a better indication of the temperature that is required on the top surface of the concrete pavement to melt ice and snow. In concrete pavement, the heat flow is toward the top surface of pavement during cooling, while in the LGCC experiment the heat flow is toward the bottom surface of the mortar specimen during cooling since the cold plate is located at the bottom. The onset temperature of the phase transformation at the bottom surface of the specimen was near 1.2 °C to 3 °C, which is in the range of desired temperatures for deicing applications for concrete (Bentz and Turpin, 2007; Ling and Poon, 2013; Sakulich and Bentz, 2012a, 2012b).

Table 13. Temperatures at the Top and Bottom of Mortar Specimens Associated with the Onset and the Completion of PCM Phase Transformation During LGCC Experiment

PCM Incorporation Method	PCM Type	Temperature of Specimen (°C)			
		PCM Freezing Onset		PCM Freezing Completion	
		Bottom	Top	Bottom	Top
LWA*	Methyl Laurate	-	-	-	-
	Paraffin Oil	3.0 (±0.3)	6.0 (±0.2)	-13.8 (±0.7)	-9.8 (±0.7)
Embedded Tube	Methyl Laurate	1.2 (±0.1)	3.5 (±0.1)	-12.7 (±1.5)	-9.6 (±1.5)
	Paraffin Oil	3.0 (±0.1)	5.4 (±0.4)	-8.2 (±3.1)	-5.2 (±3.4)

*Lightweight aggregate
Note: the results are reported ±1 standard deviation for at least two replicates of the LGCC experiment.

The amount of concrete that can be melted using PCM in the mortar specimen was calculated using Equation 2. The amount of ice can be simply converted to the equivalent amount of snow using the snow density and the snow packing (Schmucki et al., 2014). Equation 2 describes a procedure that can be used to determine the thickness of the ice on the surface of a concrete element that can be melted using the energy released by the PCM phase transformation.

$$Ice\ to\ concrete\ depth\ ratio = \frac{d}{D} = \frac{Q}{V_{concrete}} \cdot \frac{1}{\rho_{ice} \cdot \Delta H_{water/ice}} \quad (2)$$

Where: d is the thickness of ice on the surface of concrete element that can be melted using PCM incorporated in the concrete element

D is the thickness of the concrete element
Q (kJ) is the energy released during the PCM phase transition in the concrete element, which is obtained here using LGCC experiment for mortar specimen
$V_{concrete}$ (m^3) is the volume of concrete element, which is the volume of mortar specimen
$\Delta H_{water/ice}$ is the heat of fusion for ice during melting, which is equal to 334 kJ/kg
ρ_{ice} is the density of ice, which is equal to 916.7 kg/m^3

The ice-to-concrete depth ratio (%) was calculated for mortar specimens tested in the LGCC experiment using Equation 2 and is shown in Figure 21 as a function of elapsed time from the onset moment of PCM phase transformation. In addition, the amount of heat released during the PCM phase transformation per cubic meter of concrete was calculated from the LGCC experiment and is shown in Figure 21. As expected, mortar specimens containing methyl laurate using the LWA approach showed no heat release since a chemical reaction appears to alter the methyl laurate in LWA. Using the embedded tube approach, the methyl laurate specimen showed a considerable amount of heat release during its PCM phase transformation. The amount of ice-to-concrete depth ratio after a complete methyl laurate phase transformation within the embedded tube is near 4%, and this occurs in a relatively quick manner since the slope of the curve for methyl laurate is steeper than the ones for paraffin oil. This analysis assumes that heat conduction through the concrete is not a limiting factor in transferring energy from within the concrete to its top surface, where the snow/ice is located.

In both LWA and embedded tube methods, mortar specimens containing paraffin oil indicated significant heat release during the paraffin oil phase transformation. The amount of heat release was higher for methyl laurate than for paraffin oil because methyl laurate has a higher enthalpy of fusion than paraffin oil during solid/liquid phase transformations, as indicated in Figure 21. As a result, methyl laurate can produce a greater amount of heat during freezing than paraffin oil. The amount of ice-to-concrete depth ratio for paraffin oil is near 2.5% to 3.5%. For paraffin oil, the heat due to phase transformation is released more gradually in comparison to methyl laurate. Assuming a 14-in. (355.6-mm) thickness for a concrete pavement, paraffin oil can melt 0.35-in. (8.9-mm) to 0.49-in. (12.4-mm) thickness of ice on the surface of the pavement after the complete phase transformation.

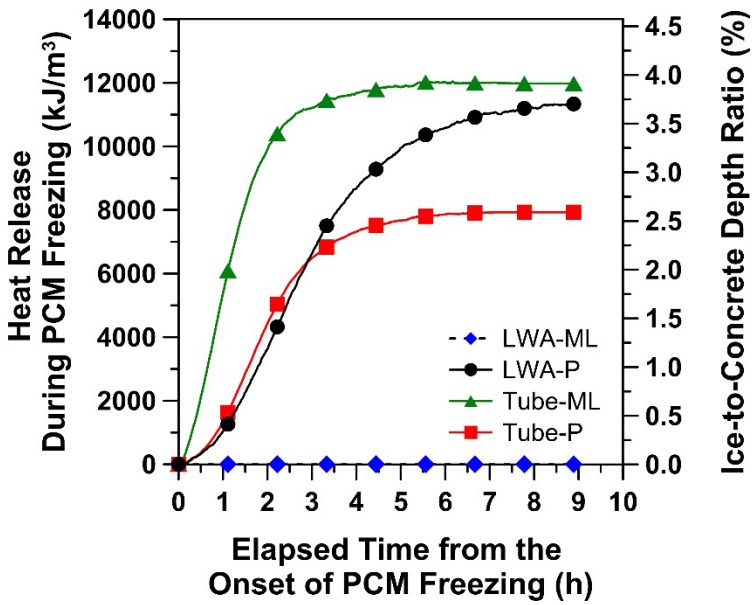

Figure 21. Released Heat During PCM Freezing in Mortar Specimen as a Function of Elapsed Time from the Onset of PCM Freezing (Quantity of PCM per volume of mortar sample varies for each case, as reported in Table 12.)

4.4.1 Chemical and Physical Durability Assessment

It is necessary that a potential PCM for deicing and snow melting applications remains non-reactive and stable over its lifetime in a concrete element. Any reaction between PCM and concrete constituents or loss of PCM over time could result in a reduction in concrete durability or a reduction in PCM performance to melt ice and snow, respectively.

4.4.2 Evaluation of Chemical Reaction Between PCM and Concrete Constituents

During the curing time of mortar specimens containing methyl laurate using LWA approach, some cracking was observed on the surface of mortar specimens, as shown by arrows in Figure 22(a). The cracking was developed and propagated over time, and a white fiber-shaped material grew within the cracking (shown by arrows in Figure 22(b)). In addition, no phase change was observed when these specimens were tested in the LGCC experiment (Figure 19). The cracking was not as severe when Type V cement was used instead of Type I cement to prepare the mortar specimen. In addition, the cracking was not observed when paraffin oil was used in the mortar specimen.

Methyl laurate appears to interact with the constituents of the mortar resulting in cracking and damage. An evaluation of this chemical reaction was performed for methyl laurate to understand the source of reaction and damage. A powder of cement paste (prepared using both Type I cement and Type V cement), calcium hydroxide, or LWA was blended and tested in LT-DSC to assess the chemical interaction. Evaluation of Type I and Type V cements can determine whether aluminate phases in concrete create the reaction, since Type V cement has relatively no tricalcium aluminate, while Type I cement has ~9% tricalcium aluminate (Table 10).

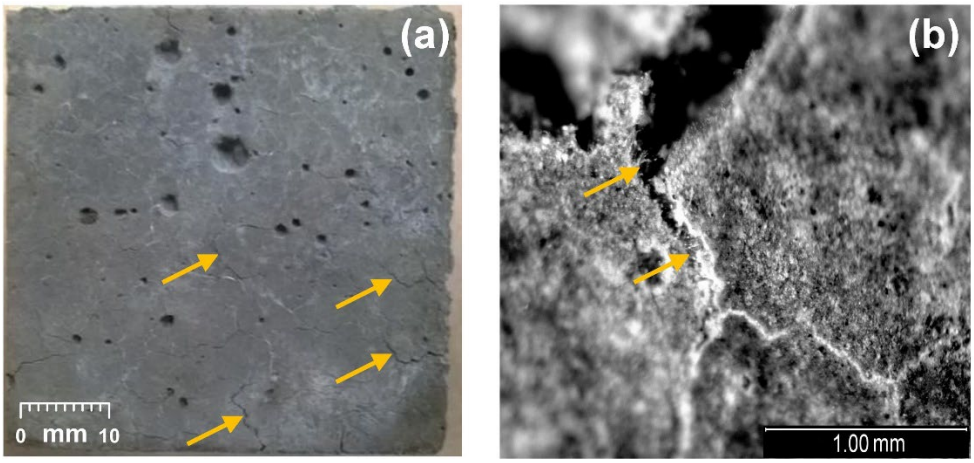

Figure 22. Mortar Specimen Containing Methyl Laurate Using LWA Approach (a) Cracked Surface (arrows show cracking) and (b) Microscopy Image (arrows show white fiber-shaped material)

Figure 23 shows the reduction in enthalpy of fusion (or heat of fusion) as a function of time for powders blended with methyl laurate obtained using LT-DSC. Paste made using Type I cement showed a substantial decrease in enthalpy indicating a relatively fast reaction between aluminate phases and methyl laurate. A reduction in enthalpy can also be seen for calcium hydroxide blended with methyl laurate, which is a reaction that appears to be more gradual than the reaction created by aluminate phases. The reduction in enthalpy is small for LWA and paste made using Type V cement. It can be concluded that aluminate phases and calcium hydroxide in cementitious materials are the main sources of the reaction between methyl laurate and the cementitious matrix. Use of Type V cement could reduce this reaction since there is relatively no tricalcium aluminate in Type V cement. However, calcium hydroxide is still present in a concrete made using Type V cement that might participate in reactions and decrease the methyl laurate performance to melt ice and snow as observed in Figure 19. Other approaches such as using an embedded tube or encapsulation can be used to incorporate methyl laurate in concrete to eliminate the reaction between methyl laurate and the cementitious matrix.

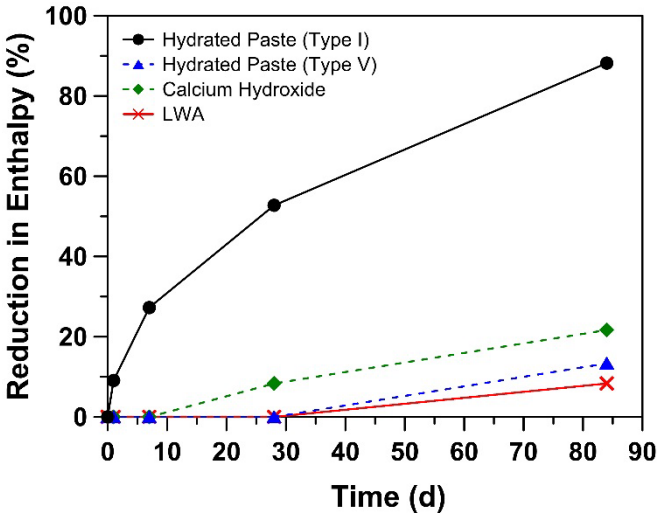

Figure 23. Reduction in Heat of Fusion (Enthalpy) Obtained Using LT-DSC for Methyl Laurate During Melting/Freezing Over Time Exposed to Different Constituents of Mortar

4.4.2.1 Evaluation of Physical Performance

The relative dynamic elastic modulus ($E_{PCM}/E_{Control}$) was calculated using Equation 3 for mortar specimens containing PCM using the LWA approach and is shown in Figure 24(a). Compressive strength was also measured and is reported in Figure 24(b).

$$\frac{E_{PCM}}{E_{Control}} = 1 - \left[\frac{V_{PCM}}{V_{Control}}\right]^2 \quad (3)$$

where E_{PCM} and $E_{Control}$ are the dynamic elastic modulus of the PCM specimen and the control specimen, respectively; and V_{PCM} and $V_{Control}$ are the average wave velocity through the length of the PCM specimen and the control specimen, respectively.

As indicated in Figure 24, mortar specimens containing methyl laurate using the LWA approach show reductions in both relative dynamic elastic modulus and compressive strength, indicating damage development and cracking in the mortar specimen due to the chemical reaction between methyl laurate and the cementitious matrix. The dynamic elastic modulus for mortar specimens containing paraffin oil using the LWA approach remains relatively unchanged (95% of the control specimen), and the compressive strength is in a desirable range for concrete pavement applications.

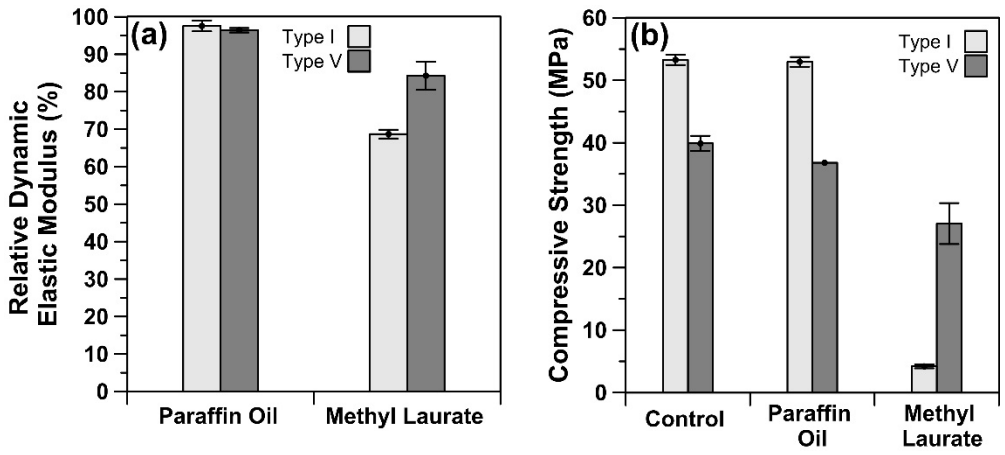

(a) (b)

Figure 24. Relative Dynamic Elastic Modulus with Respect to Control Specimen (a) and Compressive Strength for Mortar Specimen Made Using LWA and Different Types of Cement (Type I and Type V) (b) (The error bars indicate ± one standard deviation for at least two replicates of testing.)

Figure 25 indicates the mass loss as a function of time for methyl laurate and paraffin oil as they are exposed to a relative humidity of 50% and a room temperature of 23 °C. A relatively small amount of mass loss (~5%–8%) was observed after 38 days exposure. The mass loss is mainly due to PCM evaporation. This amount will be reduced for PCM stored inside a concrete element instead of experiencing direct exposure to 50% relative humidity at 23 °C since the PCM will be surrounded by a dense concrete matrix, embedded tube, or a shell provided by encapsulation.

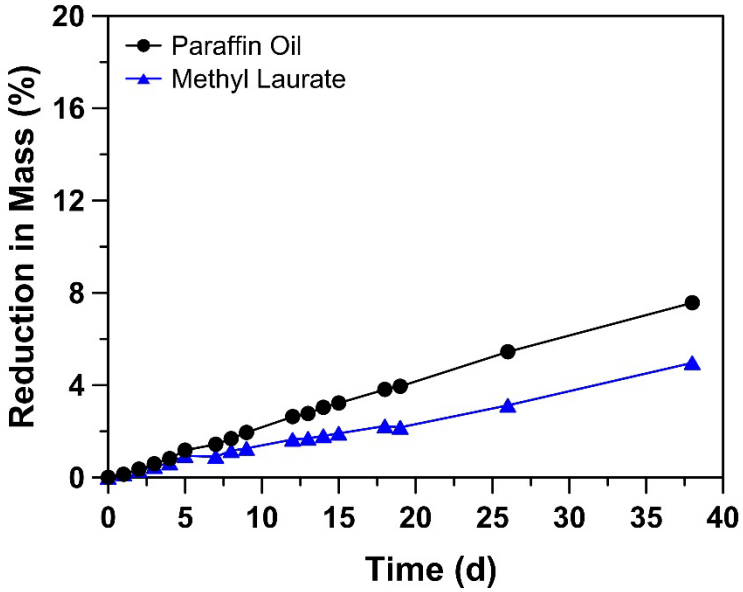

Figure 25. Stability of PCMs (i.e., change in mass) Over Time Exposed to 50% Relative Humidity at 23 °C.

4.5 SUMMARY

This study has reported the results of tests to evaluate the thermal response of mortars containing PCMs subjected to a thermal temperature cycle from 24 °C to -40 °C for use in melting snow and ice in concrete pavement. Two approaches were used to place the PCM in the mortar: (1) using LWA containing PCM and (2) using an embedded tube filled with PCM. Chemical and physical durability aspects of incorporating PCM in concrete were also assessed by monitoring the change in heat of fusion, compressive strength, relative dynamic elastic modulus, and mass loss over time. Methyl laurate and paraffin oil were selected as the PCMs used in this study. These PCMs have desired thermal properties (high heat of fusion during the phase transformation, ~ 130–160 J/g, and appropriate phase transformation temperature, ~ 2 °C–3 °C) for snow and ice melting.

When the PCM was stored in LWA and placed in the mortar specimens with PCM, the mortar specimen containing paraffin oil showed a heat release of ~ 11,000 kJ per cubic meter of mortar at ~ 3.0 °C during freezing (i.e., phase transformation of the PCM). However, methyl laurate showed no heat release due to two chemical reactions that occurred between the methyl laurate and the cementitious matrix. The two reactions appear to occur between the PCM and the aluminate phases or between the PCM and the calcium hydroxide in the cementitious matrix. As such, the use of Type V cement (containing lower tricalcium aluminate) could reduce the rate of the former reaction; but it cannot eliminate the latter reaction since cementitious material made using Type V cement still produces calcium hydroxide. Both chemical reactions appear to create cracking and damage in concrete; thereby reducing the dynamic elastic modulus and compressive strength. The use of paraffin oil as the PCM did not exhibit such reactions.

A second approach was used to place the PCM into concrete using an embedded tube/pipe filled with the PCM. The mortar with embedded tube containing paraffin oil and methyl laurate showed a heat release of ~ 7,500 (at ~ 3 °C) and ~ 12,000 (at ~ 1.2 °C) kJ per cubic meter of mortar during the phase transformation, respectively. These heat releases can be further used to melt 22–36 kg of pure ice per cubic meter of mortar on the surface of the concrete pavement. The PCM inside the embedded tube did not exhibit any reaction.

5. INCORPORATING PHASE CHANGE MATERIALS IN LARGE-SCALE CONCRETE PAVEMENT SLABS TO MELT SNOW AND ICE

Ice and snow are frequently removed from the surface of concrete pavement to increase safety during winter. Conventional methods used to remove snow/ice include snowplowing or the use of deicing chemicals/salts. The conventional methods are often costly and labor-intensive, could have environmental impacts, and can create damage in the concrete pavement (Farnam, Dick, Weise et al., 2015; Farnam, Bentz, Hampton et al., 2014; Farnam, Bentz, Sakulich et al., 2014; Farnam, Kraficik, Liston et al., 2015; Sutter et al., 2008; Shi, Fay, Peterson, & Yang, 2010). The incorporation of PCMs in concrete pavement was suggested to be an alternative way to melt snow/ice on the surface of the concrete pavement (Stoll et al., 1996; Lane, 1989; Bentz & Turpin, 2007; Farnam, Krafcik, Liston et al., 2015; Ling & Poon, 2013; Sakulich & Bentz, 2012a &2012b). Concrete containing PCM can melt snow/ice during cooling events by producing energy/heat when PCM transforms from liquid to solid (Ling & Poon, 2013; Sakulich & Bentz, 2012a; Regin et al., 2008; Sakulich & Bentz, 2012b). Therefore, the need for snowplowing would be reduced, decreasing costs; the use of deicing chemicals/salts would be reduced, which

is better for the environment and can reduce the damage caused by the deicing chemicals/salts; and the numbers of freeze-thaw cycles in concrete elements could be reduced, which can increase the service life of the concrete infrastructure.

Previous studies (Farnam, Krafcik, Liston et al., 2015; Liston et al., 2016; Liston et al., 2014) were performed to (1) produce a binary mixture of organic materials as PCMs for low-temperature applications, (2) characterize potentially desirable PCMs for snow/ice melting applications in concrete pavement, (3) evaluate approaches to incorporate PCMs in concrete, and (4) assess thermal and durability behaviors of the cementitious materials containing PCMs. This study extends the previous research by incorporating PCMs in large-scale concrete slabs and using these slabs to evaluate heat release during cooling/snowing events to melt snow/ice. Large-scale concrete slabs were prepared with and without PCM. The slabs were tested in a thermally controlled environmental chamber with an artificial snow melting experiment where shaved ice was placed on the slabs.

5.1 EXPERIMENTAL PROGRAM

The experimental program that was used in this study consisted of four parts: (1) characterizing PCM thermal behavior using a low-temperature calorimetry, (2) characterizing the properties of porous LWA used in this study, (3) thermal cycling of large-scale concrete slabs, and (4) snow melting evaluation of large-scale concrete slabs with and without PCM (Table 14).

Table 14. Experimental Program

Experiment	Sample Type	Purpose
Low-Temperature Calorimetry	(1) Bulk PCM (2) LWA* containing PCM (3) small broken piece of concrete made using PCM-impregnated LWA	To assess thermal behavior of PCM used in this study in different conditions
Particle Size Distribution and Absorption Capacity	LWA	To characterize LWA properties used in this study
Thermal Cycling	Concrete slabs: (1) Reference with no PCM (2) PCM-LWA	To assess thermal behavior of concrete slab with and without PCM
Snow Melting	Concrete slabs: (1) Reference with no PCM (2) PCM-LWA (3) PCM-PIPE	To determine melting capability of concrete slab with and without PCM

* Lightweight aggregate

5.1.1 Materials and Mixture Proportioning

OPC was used with a Blaine fineness of 375 m^2/kg. An expanded shale LWA was used in this study. These aggregates were manufactured by Buildex in their Marquette plant with a fineness modulus of 2.94 and a specific density of 1.5(Castro, Keiser, Golias, & Weiss., 2011; Miller et al., 2014). The particle size distribution of the LWA (Figure 26) was obtained using sieve analysis according to ASTM C136/C136M-14 (ASTM International, 2013). The maximum absorption capacity of LWA was determined based on saturating the sample with water using a vacuum. The LWA had a water absorption under vacuum of 32 ±0.5% by mass. The PCM ambient absorption was determined by saturating 500 grams oven dry LWAs with PCM for 72 hours. The LWA had a 72-hour PCM ambient absorption of 23.7 ±0.5% by mass. A 72-hour PCM ambient absorption of LWA was used to design the concrete mixture proportioning of a large-scale concrete slab made using LWA containing PCM. The PCM used in this study was paraffin oil, which is a petroleum-based material with a specific density of 0.77 and a vapor pressure less than 0.01 mm Hg.

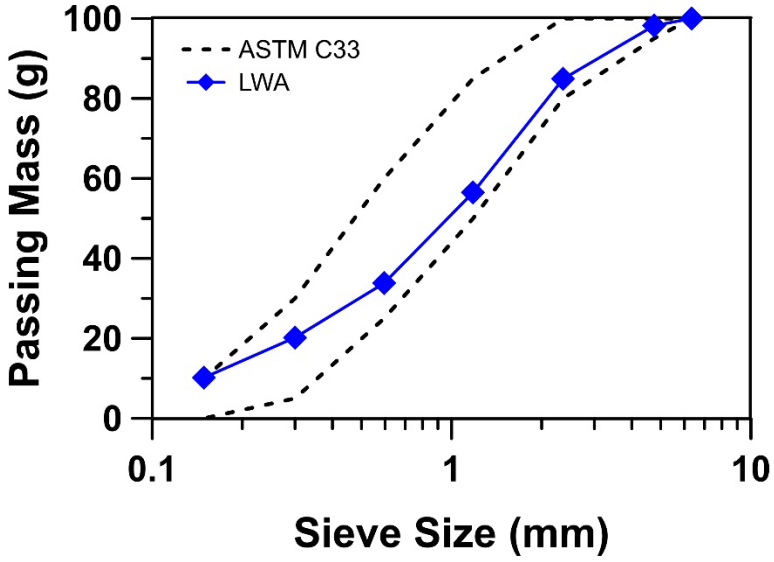

Figure 26. Particle Gradation for LWA

An LT-DSC (TA Q2000) with an operating range of -90 °C to 550 °C, was used to determine the thermal properties of the PCM (i.e., paraffin oil) (Farnam, Bentz, Hampton, &Weiss, 2014; Villani et al., 2015). Three types of samples were used in LT-DSC: (1) bulk PCM, (2) LWA containing PCM, and (3) small broken piece of concrete made using PCM-impregnated LWA. The heat flow and temperature associated with phase transitions in the samples were obtained. High-volume, stainless-steel pans (100-µL specimen size TA high-volume pans) with hermetic lids were used to contain the specimens. The temperature of LT-DSC varied between -90 °C and 50 °C. Figure 27 shows the LT-DSC testing procedure. A temperature cycling loop was performed between -90 °C and -70 °C to trigger nucleation to make sure everything transforms to solid (Farnam, Dick, Weise et al., 2015).

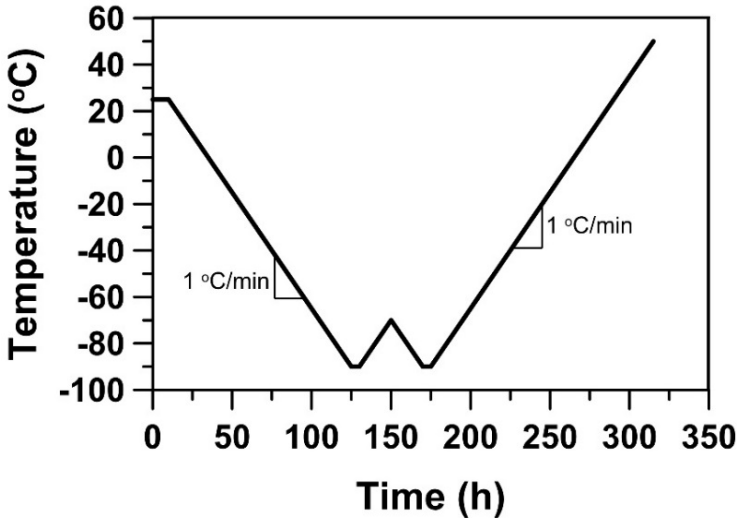

Figure 27. The LT-DSC Testing Procedure Results

5.1.2 Slab Preparation

Concrete slabs were prepared with and without PCM. Two approaches were selected to incorporate PCM into concrete slabs: (1) using LWA, and (2) using embedded metal pipes. Table 15 shows the materials proportioning in three types of slabs prepared in this study: (1) reference concrete slab with no PCM (labeled REF), (2) concrete slab made using LWA-containing PCM (labeled PCM-LWA), and (3) concrete slab with embedded metal pipes containing PCM (labeled PCM-PIPE).

Table 15. Materials Proportioning in Concrete Slabs (kg/m^3)

Item	REF	PCM-LWA	PCM-PIPE
Cement (Type I)	443	443	443
Water	199	199	199
Fine Aggregate (Natural Sand) in SSD (0–4.75 mm)	1,288	17	1,288
Coarse Aggregate (Limestone) in SSD (3/4″)	403	403	403
LWA in OD	0	717	0
Paraffin Oil	0	170	107.7*
Volume Fraction of Paraffin Oil (% by volume)	0	22.1	14.0
w/c (by mass)	0.45	0.45	0.45
Air Content	4.5	5.0	4.5
42-day Compressive Strength (MPa)	58.1 ± 1.9 **	45.9 ± 1.0	58.1 ± 1.9

* Calculated using (1) actual inner diameter size of the metal pipe = 22.5 mm (0.88 in), (2) actual length of the metal pipe considering the extension in the insulation and the wooden mold = 552.5 mm (21.75 in), and (3) the specific density of PCM = 0.77.
** ±1 standard deviation of 3 replicates

Frameworks were made to prepare concrete slabs to simulate a one-dimensional heat transfer in concrete pavement, as shown in Figure 28. Since the depth of a concrete pavement is relatively small in comparison to its width or length, one-dimensional heat transfer can be assumed in the concrete pavement. To simulate the one-dimensional heat transfer, the sides and the bottom of the sample had thermal Styrofoam insulation (thermal conductivity = 0.03 W/ (m.K)).

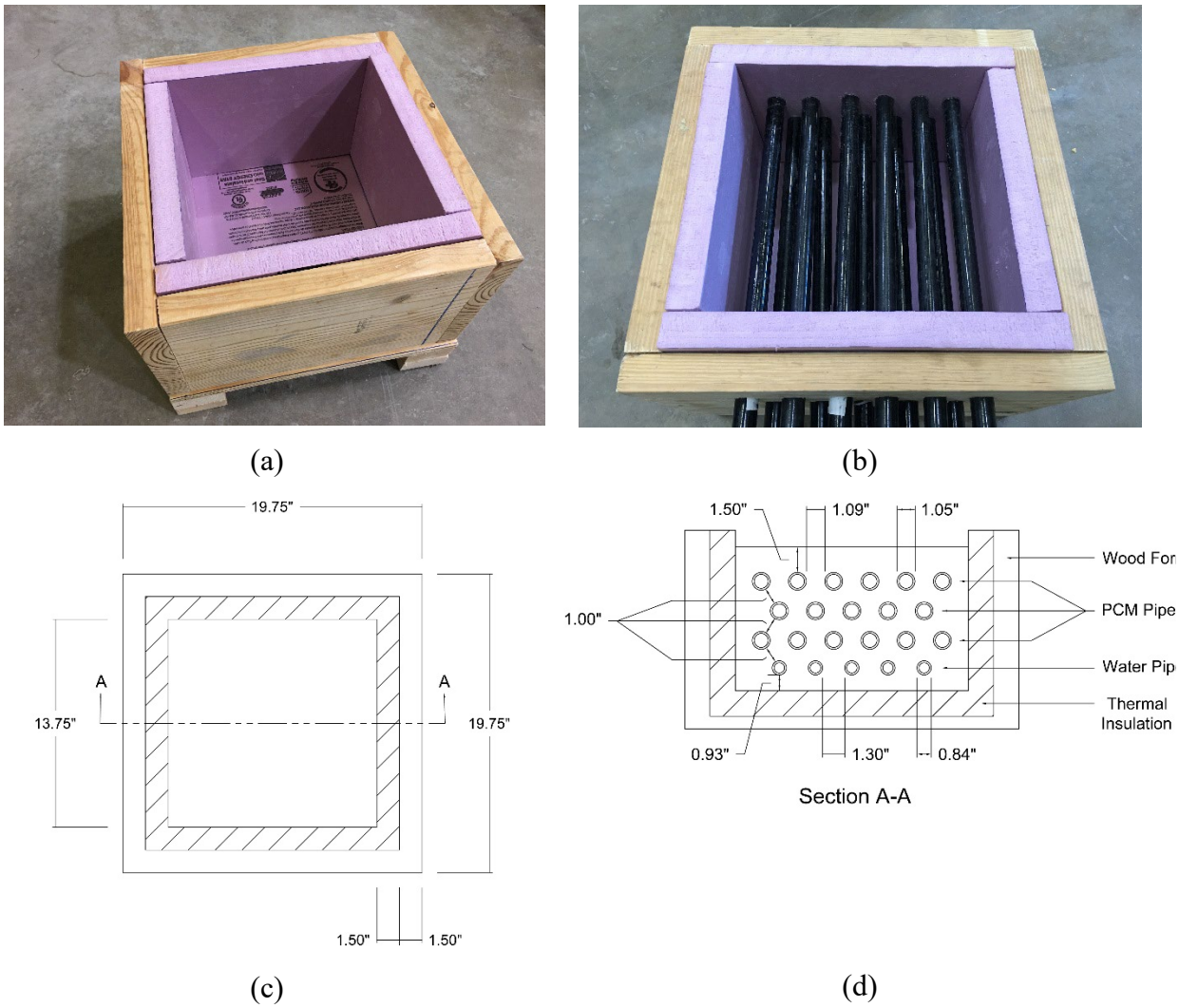

Figure 28. Design Details for the Large-Scale Concrete Slab: (a) Mold with Thermal Insulation, (b) Mold with Embedded Pipes, (c) Top View Details of the Mold and the Concrete Slab, and (d) Cross Section Details of the Mold and the Concrete Slab Containing Embedded Pipes

To prepare the concrete slabs using LWA containing PCM, oven dry LWAs were soaked in PCM for 72 hours. After soaking the LWA in the PCM, the PCM on the surface of LWAs was removed using a centrifuge (Miller et al., 2014) to reach an SSD condition. After soaking in the PCM, the LWA was placed in a centrifuge bowl; the centrifuge bowl with the LWA was then placed in the centrifuge, covered with a 4-µm filter and lid, and tightened into place; the centrifuge was then powered on and ran for 3 minutes at a speed of 2,000 rpm (Miller et al., 2014). Concrete was then prepared using LWA-containing PCM in SSD and cast in the mold

shown in Figure 28(a). The specimens were moist cured for 14 days at 23 °C ±0.5 °C. After 14 days of curing, the specimens were air-cured until the time of testing.

To prepare concrete slabs using embedded pipes containing PCM, metal pipes with an outer diameter of 26.8 mm (1.05 in.), an inner diameter of 22.4 mm (0.88 in.) and a length of 552.5 mm (21.75 in.) were located horizontally in the mold as shown in Figure 28(b) and (d). Concrete was then prepared and cast in the prepared mold. The slab was moist cured for 14 days at 23 °C ±0.5 °C. After 14 days of curing, the slab was air-cured until the time of testing. The embedded pipes were then filled using PCM, and the top and bottom of the embedded pipes were sealed using PVC caps. To prevent heat transfer through metal pipes, additional outer Styrofoam insulations were installed on both sides of the framework where pipes extended outside the framework.

The temperature was recorded at eight different locations within the depth of concrete slabs using Type T thermocouples. Figure 29 shows the location details for recording the temperature within the depth of the slab.

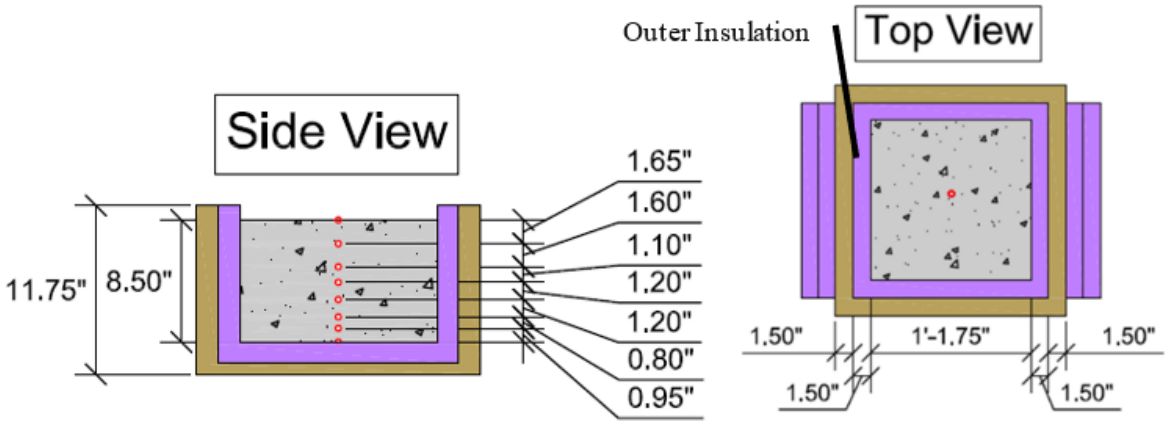

Figure 29. Thermocouple Locations (shown by red circles) Within the Depth of the Large-Scale Concrete Slab

5.2 CONCRETE SLAB TESTING PROCEDURE

Two series of experiments were conducted on the concrete slabs: (1) thermal cycling without applying artificial snow (i.e., shaved ice), and (2) snow melting with applying artificial snow on the top of the slab to simulate snow.

For the thermal cycling experiment, the concrete slabs were located in a thermally controlled environmental chamber. The ambient temperature was then varied between +10 °C and -10 °C. The initial temperature of the test was set to remain at 10 °C (for 3–5 days) to allow the slab to equilibrate. After the initial temperature stabilized, two cycles each of cooling and heating were applied: (1) the ambient temperature in the chamber was cooled from 10 °C to -10 °C at a rate of 4 °C/h within 5 hours, (2) once the slab reached -10 °C, the temperature of the chamber was kept constant for 24 hours, (3) the temperature was then increased to +10 °C at a rate of 4 °C/h within 5 hours, and (4) after reaching +10 °C, the temperature was kept constant for 48 hours.

5.2.1.1 Snow-Melting Experiment

For the snow-melting experiment, artificial snow (i.e., shaved ice) was made using cubic ice at 0 °C and a commercial ice shaver machine, and it was applied onto the surface of the concrete slabs while they were in a thermally controlled environmental chamber. Figure 30 illustrates the snow-melting experiment. Two slabs were tested concurrently in the chamber and a time-lapse camera with 1-minute capturing intervals was used on top of slabs to record snow-melting behavior. Each slab was tilted slightly (2°–5°) to allow molten snow (water) to, first, easily flow on the surface of the concrete slab, and second, run into a plastic tube that was connected to a beaker on a scale used to collect molten snow (water). The mass change of the beaker with molten snow (water) was recorded every 15 minutes. The temperature in the slab was also recorded every 1 minute at eight different locations as described in Figure 29.

Two tests were used with different temperature sequences. In the first test, procedure A, the maximum ambient temperature was kept at 7 °C while the minimum ambient temperature was kept at 2 °C. In the second experiment, procedure B, the maximum ambient temperature was kept at 5 °C while the minimum ambient temperature was kept at 0 °C. The maximum temperature for procedure A was kept above the freezing temperature of PCM (5.7 °C as reported in Table 16) while the maximum temperature for procedure B was kept near below the freezing temperature of PCM. This was done to assess the capability of PCM to melt snow at different temperatures.

The snow-melting experiment consisted of

(1) equilibrating the slab temperature at the maximum ambient temperature (for 3–5 days),
(2) decreasing the ambient temperature in the thermally controlled environmental chamber to the minimum ambient temperature in 1 hour,
(3) keeping the temperature at the minimum temperature for 3 hours,
(4) adding 3,000 g of artificial snow on the top of the slab in less than 5 minutes,
(5) keeping the temperature at the minimum temperature for 45 hours,
(6) increasing the temperature to the maximum temperature in 1 hour, and
(7) keeping the temperature at the maximum temperature for 3–5 days.

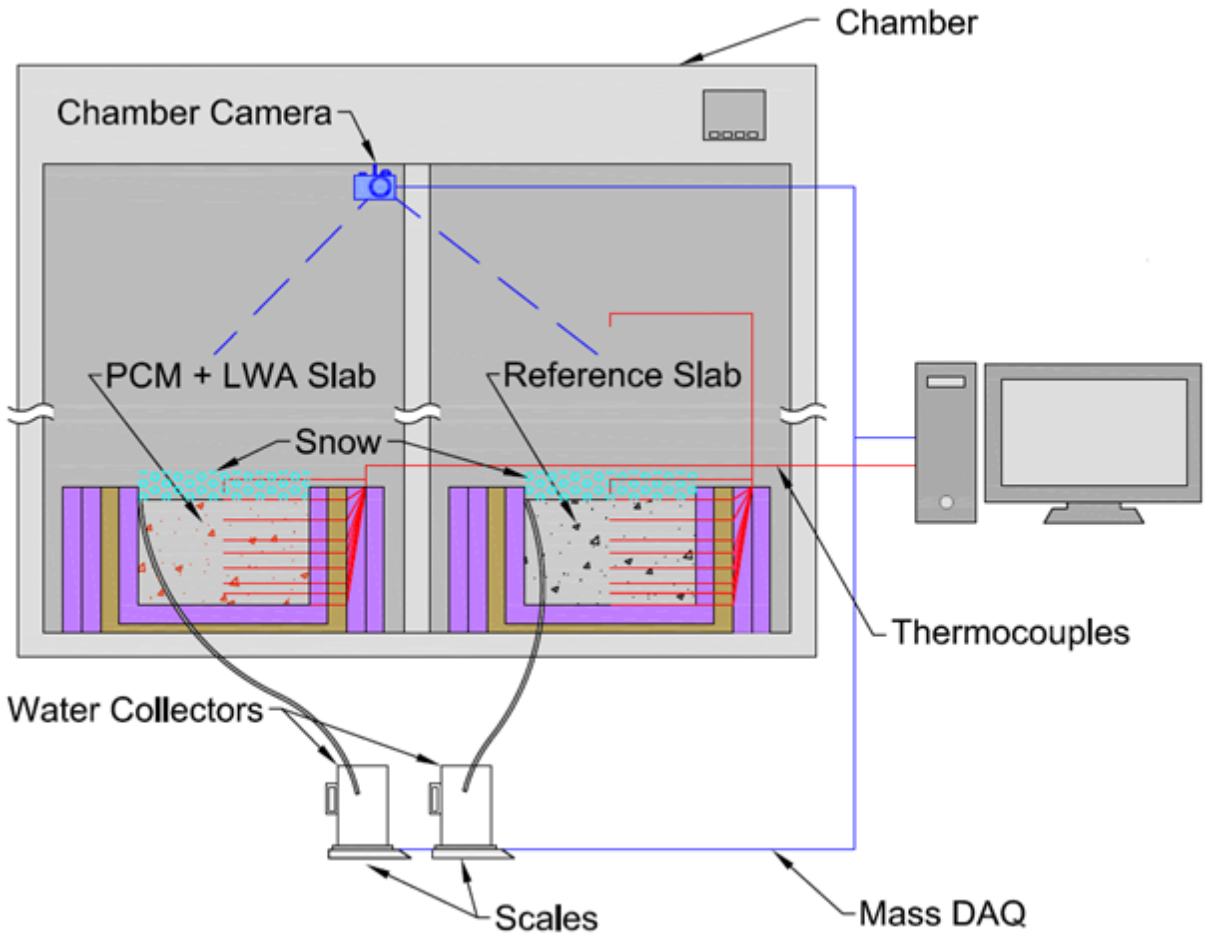

Figure 30. Snow-Melting Experiment Setup (The camera records the surface of the slabs.)

5.3 RESULTS

5.3.1 Thermal Behavior of PCM

Figure 31 illustrates the thermal behavior of PCM during the LT-DSC heating cycle in three conditions: (1) bulk PCM, (2) LWA containing PCM, and (3) small broken piece of concrete made using PCM-impregnated LWA. The heat release during each peak (indicating a phase transformation) was calculated using the heat curves (Figure 31(d), (e), and (f)) and is reported in Table 16. As expected, the bulk PCM showed a higher level of heat release (Table 16) since LWA and concrete samples have a lower volume fraction of PCM. Considering the PCM absorption of LWA (23.7% by mass), the heat release for LWA due to PCM phase transformation can be expected to be 23.7% of the bulk PCM. However, the LT-DSC result for LWA containing PCM (reported in Table 16) indicates even lower values due to the effect of pore sizes of the LWA, which changes the melting temperature. According to the Gibbs-Thomson equation, the freezing temperature of a liquid inside a porous material depends on its pore radius (Esmaeeli et al., 2016; Sun & Scherer, 2010a, 2010b, 2010c). PCM in smaller pores freezes at a lower temperature than PCM in bigger pores, which describes the observation of

several gradual LT-DSC peaks for LWA containing PCM in Figure 31(b). This behavior creates a gradual heat release as the temperature decreases. The same behavior can be seen for the broken concrete sample made using PCM-impregnated LWA (Figure 31(c)). Section 5.3.3 discusses how the gradual phase transformation due to pore size effect in LWA can be beneficial in melting snow in a wide range of temperatures in concrete slabs.

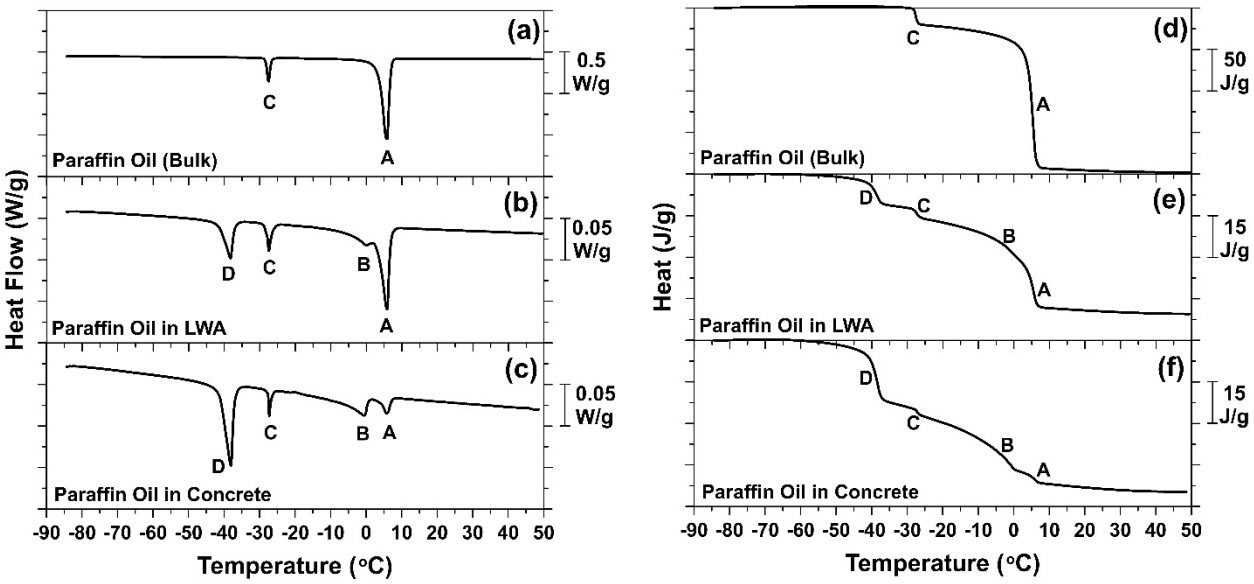

Figure 31. Thermal Response (left: heat flow, and right: heat) of PCM (paraffin oil) Used in this Study in Different Conditions: (a, d) Bulk Paraffin Oil, (b, e) LWA Containing PCM, and (c, f) Small Broken Piece of Concrete Made Using LWA Containing PCM (Note the scale bar varies for different conditions to better illustrate the peaks.)

Table 16. Results from LT-DSC

Sample Type	Sample Mass (mg)	PCM Mass (mg)	Heat Release (J/g_{Sample}) Peak A	Peak B	Peak C	Peak D	Temperature (°C) Max. of Peak A	Max. of Peak B	Max. of Peak C	Max. of Peak D
Bulk Paraffin Oil[a]	11.2 (±0.5)	11.2 (±0.5)	157.8 (±1.0)	NA*	19.8 (±0.5)	NA*	5.7 (±0.0)	NA*	-27.5 (±0.0)	NA
LWA Containing Paraffin Oil[b]	23.4 (± 9.5)	5.7 (±1.8)	16.3 (±3.4)	9.8 (±0.8)	3.1 (±0.4)	13.5 (±4.8)	5.8 (±0.1)	-2.0 (± 1.8)	-27.5 (± 0.1)	-38.2 (± 0.0)
Broken Concrete Made Using LWA Containing Paraffin Oil[c]	17.5 (±4.0)	6.4[d] (±1.5)	3.7 (±2.6)	10.5 (±0.6)	1.7 (±0.2)	16.5 (±3.4)	5.5 (±0.3)	-0.7 (±1.1)	-27.1 (±0.2)	-38.3 (±0.2)

* Not Available
[a] The value inside parentheses shows a standard deviation for 2 replicates.
[b] The value inside parentheses shows a standard deviation for 4 replicates.
[c] The value inside parentheses shows a standard deviation for 3 replicates.
[d] This value is estimated using information in Table 15 and may not be the actual amount of the PCM in the sample.

5.3.2 Thermal Cycling of Concrete Slabs

Concrete slabs with and without PCM were exposed to thermal cycling to evaluate the thermal response of the slabs during temperature variations. Figure 32 shows the thermal response of concrete pavement during thermal cycling of concrete slabs and the ambient temperature to illustrate cooling/heating moments in the concrete slabs. For the reference concrete slab with no PCM (Figure 32(b)), the very rapid decrease/increase of the temperature within the depth of the slab corresponded to the ambient temperature decrease/increase. For the concrete slab made using concrete with LWA containing PCM (Figure 32(c)), the temperature change within the depth of the slab due to ambient temperature variation has a time delay. This delay is mainly because PCM freezing/melting provides a gradual heat that is released/absorbed. The gradual heat release/absorption can compensate for the heat loss/gain in the concrete slab as the ambient temperature varies. As a result, the temperature within the depth of the concrete slab changes relatively slowly in the concrete slab containing PCM. This implies that the concrete slab made using LWA containing PCM will stay "warmer" for a longer period of time as the environmental temperature drops; thereby keeping the snow-melting capability of the slab active.

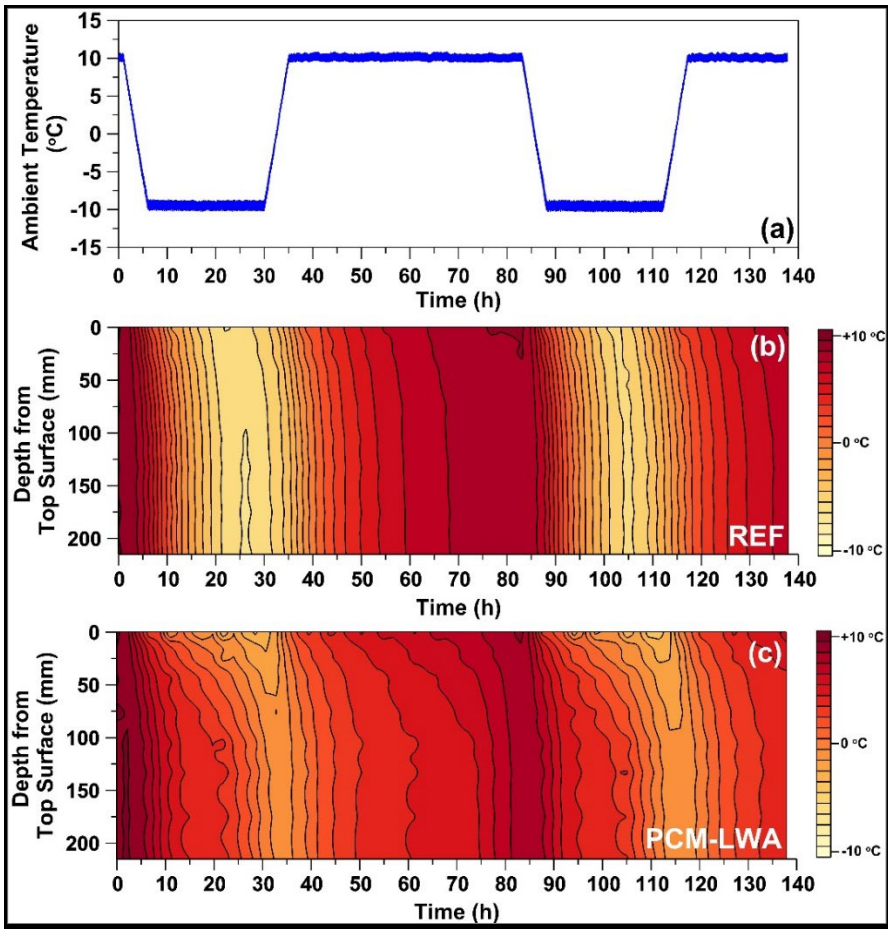

Figure 32. Thermal Cycling of the Concrete Slab (a) Ambient Temperature Applied in Thermal Cycling Experiment, (b) Temperature Profile Within the Depth of Reference Slab as a Function of Time, and (c) Temperature Profile Within the Depth of Slab Made Using LWA Containing PCM as a Function of Time

5.3.3 Snow-melting Potential of Concrete Slabs

To evaluate the snow-melting potential of slabs made using PCM, artificial snow (shaved ice) was prepared and applied on the surface of concrete slabs. Three types of data were recorded during the test: (1) time-lapse images were taken as a qualitative observation, (2) mass of molten snow (water) was monitored as a quantitative measurement, and (3) temperature profile within the depth of the slab was recorded as a quantitative measurement. Two testing procedures were applied (Section 5.2.1.1): procedure A (temperature varying between 7 °C and 2 °C), and procedure B (temperature varying between 5 °C and 0 °C).

5.3.3.1 Time-lapse Video

Time-lapse images were taken every 1 minute as a qualitative observation, and a video was produced for each test using VideoVelocity© software. Because of size limitations in the cooling-heating chamber, only two slabs were tested concurrently in the chamber. Table 17 presents the YouTube links for the time-lapse videos produced in this study for different types of slabs and testing procedures.

Table 17. Time-lapse Videos for Snow-melting Experiment*

Snow-Melting Procedure	Slab Types	YouTube link
Procedure A (temperature varying between 7 °C and 2 °C)	Reference and PCM-LWA	https://youtu.be/Ih45DB11IlI
	PCM-LWA and PCM-PIPE	https://youtu.be/PJht6Rx78bM
Procedure B (temperature varying between 5 °C and 0 °C)	Reference and PCM-LWA	https://youtu.be/1RVOiK9qNeA
	PCM-LWA and PCM-PIPE	https://youtu.be/RmZe7-SVsFY

* Time-lapse images began at the moment of snow addition to the surface of the slabs.

For procedure A, the concrete slab with embedded pipes containing PCM melts snow faster than the concrete slab made using LWA containing PCM. Both slabs containing PCM seemed to be capable of melting the entire amount of the added snow (3,000 g) within the cooling event when the temperature remained at 2 °C, while the reference sample without PCM was not able to melt the entire amount of snow within the cooling event until the temperature rose back to 7 °C.

For procedure B, none of the slabs could melt the entire amount of snow (3,000 g) within the cooling event when the temperature remained at 0 °C. However, it seems that the amount of available snow at the end of the cooling event was much lower in the slabs containing PCM than the reference slab with no PCM. Within the cooling event (when the temperature remains at 0 °C), the concrete slab made using LWA containing PCM appeared to melt snow more than the concrete slab with embedded pipes containing PCM, an opposite observation in comparison to procedure A, which will be discussed further in Section 5.3.3.2.

5.3.3.2 Mass of Molten Snow

The mass of molten snow (water) was measured every 15 minutes from the moment that snow was added to the surface of the slab to quantify the melting potential of the concrete slabs. Figures 33and 34 show the mass of molten snow (water) for two types of snow-melting testing procedures. The ambient temperature is shown in Figures 33 and 34 to illustrate the moments of cooling/heating events and the moment of snow addition to the surface of the slab. In addition, the equivalent depth of snow on the surface of the concrete slab is calculated and is shown in these figures assuming that the density of snow is 200 kg/m^3. In general, the density of snow varies between 50 and 400 kg/m^3 depending on its compaction: (1) new unpacked snow has a density between 50 and 70 kg/m^3, (2) damp new snow has a density between 100 and 200 kg/m^3, (3) settled snow has a density between 200 and 300 kg/m^3, and (4) wind-packed snow has a density between 350 and 400 kg/m^3(Paterson, 1994). In this study, it was assumed that damp/settled snow was used with a density of 200 kg/m^3.

The result of snow-melting mass for procedure A is shown in Figure 33(b). Both slabs containing PCM were able to melt the entire 300 g (136.9 mm) of added snow during the first ~25 hours after adding the snow when the ambient temperature remained at the minimum temperature (2 °C, i.e., the cooling event). However, the reference slab was not able to melt the entire amount of added snow during the cooling event, with only 67.4% of the snow melted. Figure 33(c) indicates the snow melting rate. The melting rate during the cooling event was higher at the beginning and then decreased over exposure time. The initial melting rate was the highest for the slab with embedded pipes containing PCM and the lowest for the reference sample among the three slabs tested in this study. Figure 33(d) shows the difference between the molten snow results for the slabs containing PCM and the molten snow results for the reference slab. The maximum difference reached was 62.6 mm (2.5 in) for the slab with pipes containing PCM, while this value was 52.2 mm (2.1 in) for the slab made using LWA containing PCM. These observations indicate that incorporating PCM into concrete slabs increases the snow-melting capacity of the concrete slab and can melt about 52.2–62.6 mm (2.1–2.5 in.) of snow more than the concrete slab without PCM during snowing events.

Figure 33(b) and (c) illustrate that the melting capability is faster for the concrete slab with embedded pipes containing PCM than the concrete slab made using LWA containing PCM, while the volume of PCM in the slab made using LWA containing PCM is higher than the volume of PCM in the slab with embedded pipes containing PCM (as reported in Table 15). This is due in part to the pore size effect that was discussed in Section 5.3.1. Various pore sizes in LWA provide a gradual heat release during PCM phase transformation that could decrease the rate of snow melting (when the ambient temperature before snowing event remains higher than the freezing temperature of PCM, 5.7 °C in this study, see Table 16). The fast-melting capability in the slab with pipes is mainly due to the fact that the freezing of PCM in the embedded pipes occurs rapidly and at one time. In the case where the slabs are exposed to a lower ambient temperature than the PCM freezing temperature before the snowing event occurs, PCM in embedded pipes might undergo its phase transformation before the snowing event and the PCM melting potential could reduce. To understand this hypothesis, another temperature variation was applied during the snow-melting experiment, and the ambient temperature on the surface of concrete slab varied between 5 °C and 0 °C (i.e., procedure B).

Figure 34 indicates the results of snow-melting experiment with the temperature history from procedure B. As hypothesized, the slab made using LWA containing PCM shows an improved melting capacity when compared with the slab with pipes containing PCM. In this case, the gradual heat release due to the different pore sizes in LWA is more beneficial for melting snow. The gradual heat release in the slab that used LWA containing PCM can melt snow over a wide range of temperature variations, but the slab with embedded pipes containing PCM might not be able to melt snow as well when the ambient temperature before a snowing event drops to a temperature below the PCM freezing temperature.

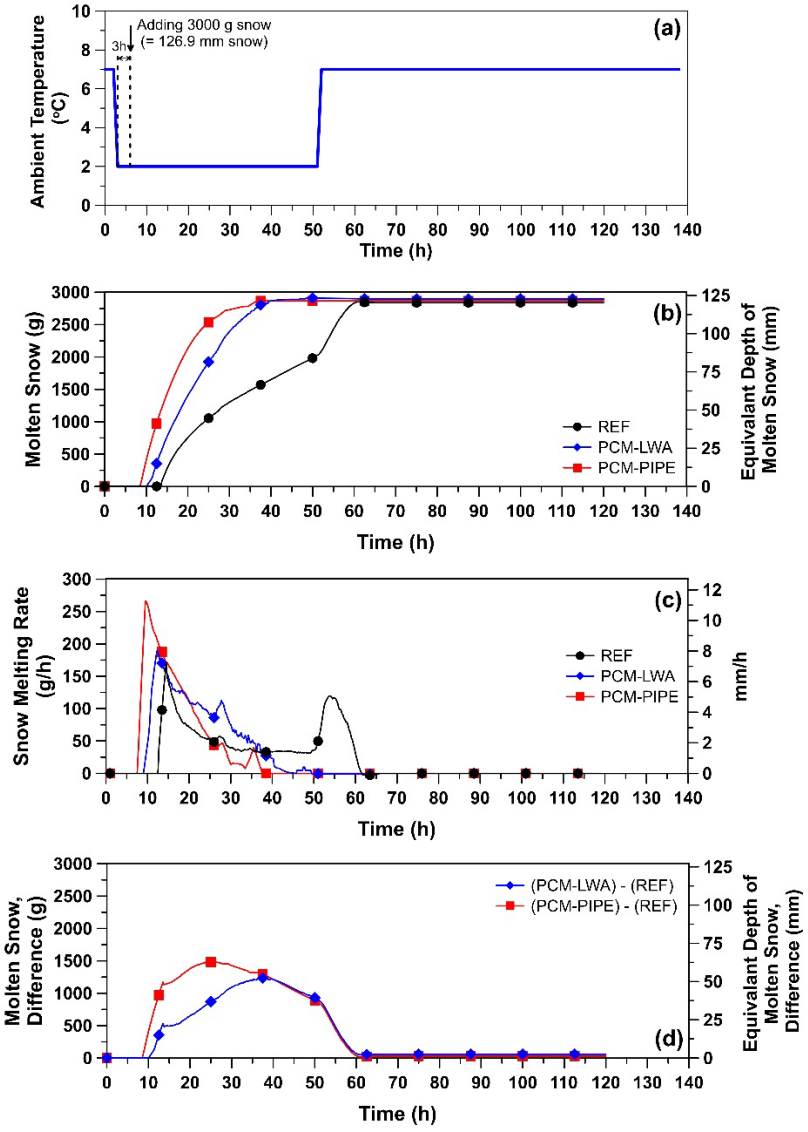

Figure 33. Snow Melting Test for Procedure A with Temperature Varying Between 7 °C and 2 °C: (a) Temperature History and the Moment of Snow Addition to the Surface of the Slab, (b) Mass of Molten Snow and Calculated Equivalent Depth of Molten Snow (with a density equal to 200 kg/m^3), (c) Snow Melting Rate, and (d) Mass and Depth Difference of Molten Snow (with a density equal to 200 kg/m^3) Between PCM Slab and Reference Slab

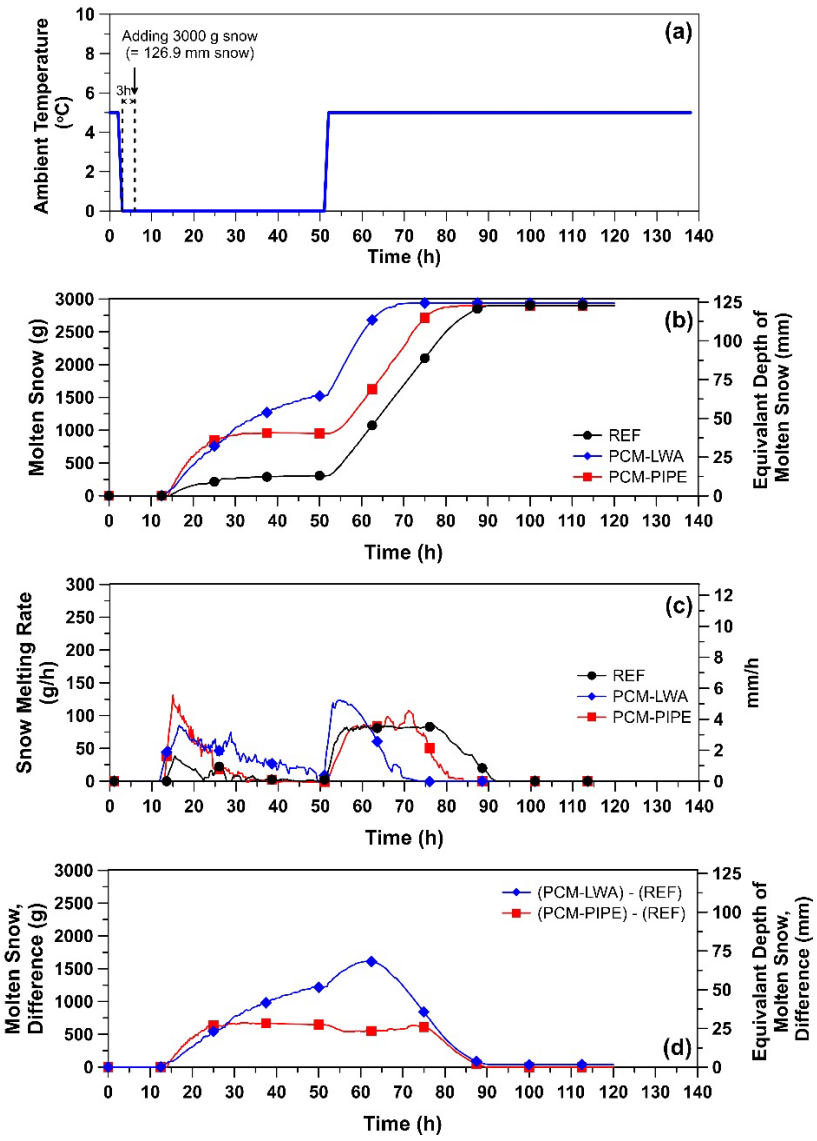

Figure 34. Snow Melting Test for Procedure B with Temperature Varying Between 5 °C and 0 °C: (a) Temperature History and the Moment of Snow Addition to the Surface of the Slab, (b) Mass of Molten Snow and Calculated Equivalent Depth of Molten Snow (with a density equal to 200 kg/m^3), (c) Snow Melting Rate, and (d) Mass and Depth Difference of Molten Snow (with a density equal to 200 kg/m^3) Between PCM Slab and Reference Slab

5.3.3.3 Temperature Profile within the Depth of the Concrete Slab

Figures 35 and Figure 36 illustrate the temperature profiles in the concrete slabs for ambient temperature varied according to procedures A and B, respectively. The temperature in the slab decreased as the snow was added to the surface of the slab. The temperature drop in the concrete slab during snow addition is due to two main reasons: (1) heat diffuses from higher temperature (inside the slab) to a lower temperature (top surface of the slab) lowering the energy (heat) level of the concrete slab, and (2) the melting of the snow absorbs energy from the surrounding environment (primarily concrete slab) and lowers the energy (heat) level of the concrete slab. As

observed in Figures 35 and 36, the temperature drop in the concrete slab after the addition of snow was more noticeable in the reference slab than in the slabs containing PCM. In slabs containing PCM, the heat release due to the PCM phase transformation compensates for a portion of the heat loss from the concrete slab preventing a noticeable temperature drop. The temperature drops in the concrete slab that used LWA containing PCM was slower than both the reference slab and the slab with embedded pipes containing PCM. Again, this is mainly due to the gradual heat release during the PCM phase transformation in the concrete slab that used LWA containing PCM that keeps the temperature change within the depth of the concrete slab less pronounced.

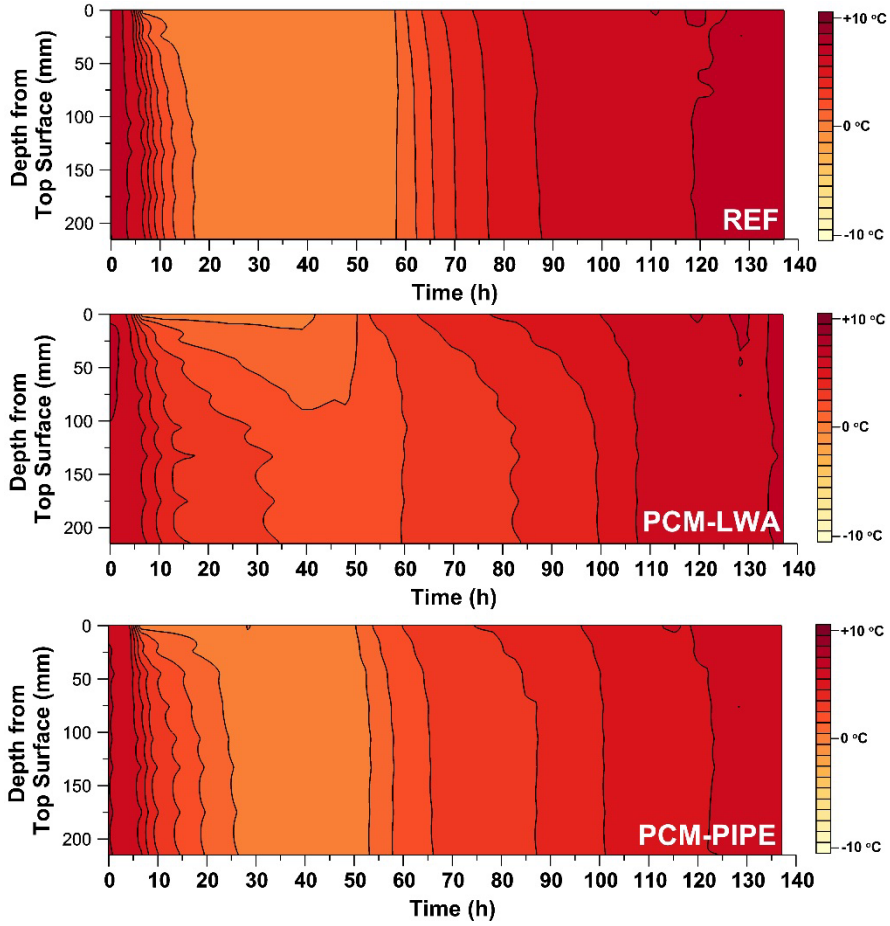

Figure 35. Temperature Profile Within the Depth of Slab as a Function of Time for Snow-Melting Test with Temperature Varying Between 7 °C and 2 °C (Procedure A)

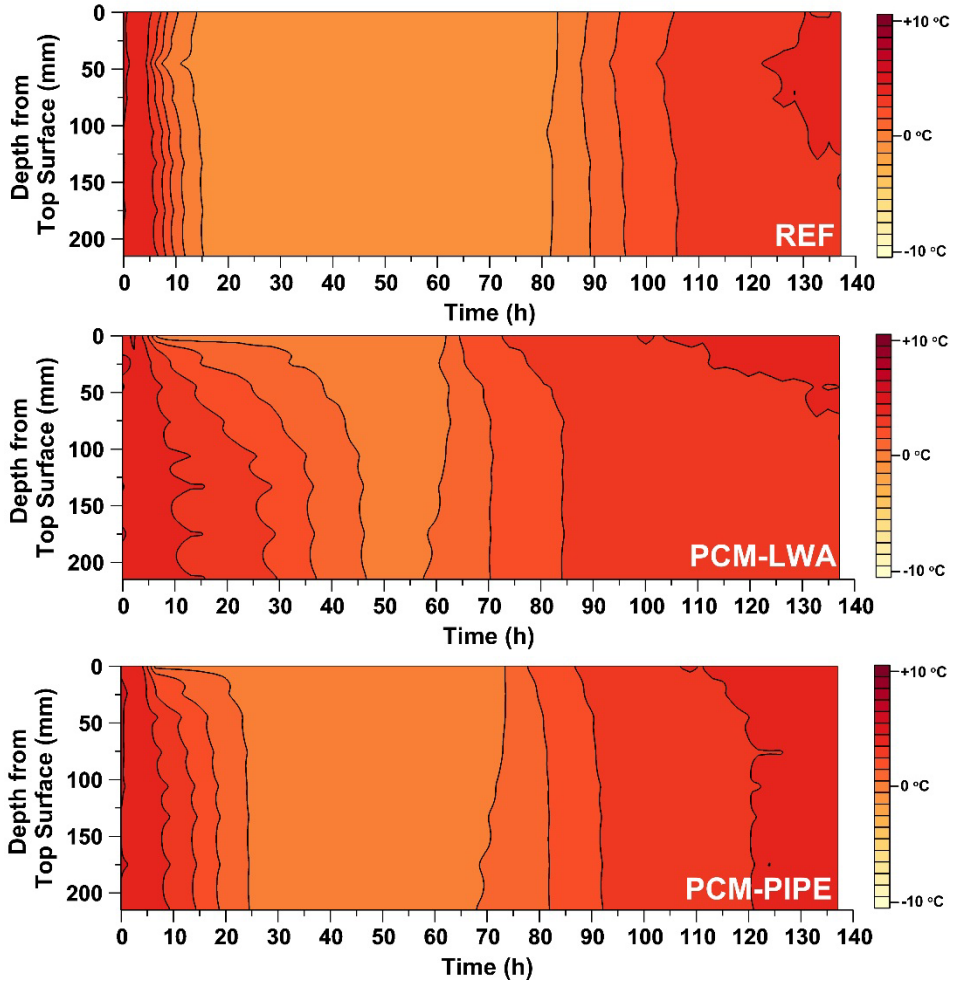

Figure 36. Temperature Profile Within the Depth of Slab as a Function of Time for Snow-Melting Test with Temperature Varying Between 5 °C and 0 °C (Procedure B)

5.4 SUMMARY

This section discussed the use of PCMs in large-scale concrete slabs to melt snow/ice. As the ambient temperature decreases to a temperature below the freezing temperature of PCM, the PCM undergoes a phase transformation from liquid to solid that can be used to melt snow/ice on the surface of the concrete pavement. Both the embedded pipe and LWA methods of PCM incorporation (discussed in Section 1) showed the ability to melt snow/ice on the surface of the concrete slabs. When the concrete slab was exposed to an ambient temperature above the freezing temperature of PCM before a snowing event, a relatively rapid heat release was observed for the embedded pipe method during PCM phase transformation, while the heat release in LWA method was more gradual. The rapid heat release in the slabs with embedded pipes containing PCM could be beneficial in melting snow/ice due to its faster rate than slabs made using LWA containing PCM; however, the snow-melting capability in the slabs with embedded pipes containing PCM can noticeably decrease when the concrete slab is exposed to an ambient temperature near or below the freezing temperature of PCM before snowing event. In

the LWA method, in contrast, the gradual heat release can be used in a wide range of temperature variation and the snow-melting capability remains relatively beneficial.

Additional research is needed to further understand other factors influencing concrete constructability and concrete pavement performance when the concrete contains PCM. Future research in this area might include concrete rheological performance, durability of concrete pavement, skid resistance of the pavement, and long-term stability of the PCM.

6. DEVELOPING A NUMERICAL MODEL TO SIMULATE PHASE CHANGES IN CONCRETE

Deicing salts are applied to the surface of concrete pavements to melt ice and snow in an effort to improve safety conditions for the traveling public. The solution that is produced (e.g., water-NaCl, $CaCl_2$, $MgCl_2$) can be absorbed into concrete pores. This solution alters the degree of saturation (i.e., the volume ratio of fluid in the specimen as compared to the total maximum volume of fluid that the specimen can hold) of the concrete pavement and the freezing temperature of the solution within the concrete pores, and can result in damage to the concrete pavement (Powers & Willis, 1950; Powers, 1945; Powers, 1958; Litvan, 1976; Scherer, 1999; Kaufman, 1999; Mehta & Monteiro, 2006; Spragg et al., 2011; Farnam, Bentz, Sakulich, Flynn, & Weiss, 2014; Villani et al., 2015; Farnam, Bentz, Hampton, &Weiss, 2014; Farnum, Esmaeeli, Bentz, & Zavattieri, 2015; Farnam, Wiese, Bentz, Davis, & Weiss, 2015).

Prediction of phase transformation within the pores requires an understanding of heat flow within a mortar during a freezing/thawing cycle (Han, Choi, Dantzig, & Bischof, 2006; Radjy, 1968). For this discussion, the term “latent heat” is used to denote the amount of energy released or absorbed during a phase transformation (formation or melting of ice or eutectic solid). The latent heat produced by the phase transformation of the pore solution can be used to quantify the amount of pore solution in concrete that freezes (Powers, 1945). There are two main phenomena that affect the freezing of pore solution in a mortar/concrete: (1) its pore size distribution, and (2) undercooling.

First, the pore size distribution in concrete influences its freezing. Concrete pores are typically categorized into three main classes: (1) gel pores with a radius smaller than 5 nm that are associated with the formation of cement (binder) hydration products, (2) capillary pores that are the remnants of the original water-filled space between (cement) particles and commonly range from 5 nm to 5 μm in radius, and (3) air-entrained or air-entrapped pores (voids) that range from 5 μm to 10 mm (Young, 1988; Whiting & Nagi, 1998; Kumar & Bhattacharjee, 2003; Castro, Bentz, & Weiss, 2011). The size of the pores in the concrete can influence the temperature at which freezing occurs. This is described using the Gibbs-Thomson equation (Sun & Scherer, 2010a). A large fraction of water associated with pore sizes greater than 5 nm (i.e., capillary pores or air-entrained or air-entrapped pores) is susceptible to freezing at a temperature above -10 °C (Farnam, Bentz, Sakulich et al., 2014; Li, Pour-Ghaz, Castro, & Weiss, 2012; Cai & Liu. 1998). According to the Gibbs-Thomson equation, the water absorbed in the gel pores will not begin to freeze until the temperature of the specimen drops to about -13 °C (Cai & Liu, 1998; Li, Sun, & Jiang, 2011; Sun & Scherer, 2010b). It is also worth mentioning that the solution inside concrete pores (i.e., pore solution) contains different ionic species (such as Na^+, K^+, Ca^{++}, and OH^-) (Andersson, Allard, Bengtsson, & Magnusson, 1989) that depress its freezing

temperature (Mehta & Monteiro, 2006). The absorption of salt solution into the pores can further depress the freezing temperature of this pore solution, due to the presence of additional ions, such as Cl^- (Scherer, 1999; Pigeon & Pleau, 2010; Beddoe & Setzer, 1988).

Undercooling also influences freezing in concrete. While it is expected that a solution freezes at its characteristic melting point temperature, T_m, freezing usually occurs at a temperature (i.e., T_f) lower than T_m. This reduction in freezing temperature is known as undercooling (Askeland & Pradeep, 2003; Debenedetti & Stanley, 2003; Wilding, 1992) and is primarily due to the fact that solidification (in most cases) requires the presence or formation of nuclei that can trigger the freezing action. Once the heterogeneous nuclei are present in the liquid phase, ice crystals begin to nucleate/grow; consequently, the latent heat of fusion is released into the undercooled liquid, increasing the temperature of the liquid toward T_m. Growth of ice continues until the temperature of the liquid reaches T_m (Askeland & Pradeep, 2003). Afterwards, the temperature of the liquid remains at T_m until the entire liquid solidifies; this is known as thermal arrest (Askeland & Pradeep, 2003). After thermal arrest, the amount of ice increases gradually as the temperature further decreases. Melting, however, occurs gradually in the pores as the temperature of each pore reaches its T_m value (Farnam, Bentz, Sakulich et al., 2014; Sun & Scherer, 2010b; Qian, Farnam, & Weiss, 2014). The amount of ice transformed to solution increases gradually as each set of larger pores in turn reach the associated T_m (according to the Gibbs-Thomson equation) (Sun & Scherer, 2010b, 2010c).

These two phenomena (i.e., pore size and undercooling) affect the freezing behavior of pore solution simultaneously in the mortar specimen and it may be essential to consider both in the simulation during freezing. In melting, however, only pore size influences the thawing behavior. Numerically, it is feasible to develop a theoretical model based on the heat transfer formulation to predict and simulate phase transformation and heat transfer in materials (Thomas, 1993; Velraj, Seeniraj, Hafner, Faber, & Schwarzer, 1999). One-dimensional finite difference (Velraj et al., 1999; Lecomte & Mayer, 1985; Costa, Buddhi, & Oliva, 1998; Bentz, 2000; Bentz & Turpin, 2007), two-dimensional finite difference (Velraj et al., 1999; Costa et al., 1998; Bentz & Turpin, 2007; Zivkivic & Fujii, 2001; Ismail & Abugderah, 2000), control volume (Hamada, Ohtsu, & Fukai, 2003; Voller & Swaminathan, 1993; Ismail & Da Silva, 2003; Fukai, Hamada, Morozumi, & Miyatake, 2003), and finite element (Gong & Mujumdar, 1997; Rubinsky & Cravahlo, 1981; Yoo & Rubinsky, 2007) methods all have been used to simulate such heat transfer problems. In this study, a one-dimensional finite difference model was used. In particular, this numerical method approximates the complex solid–liquid interactions in the porous mortar using a fixed-grid method (Shamsundar & Sparrow, 1975; Hibbert, Markatos, & Voller, 1988). The computational model is applied to estimate the thermal behavior of mortar containing NaCl solutions or just water under freeze-thaw cycles. The formation of ice is quantified by calculating the volume fraction of ice that is produced and the concentration of the remaining fraction of solution during cooling using the lever rule (Smith & Hashemi, 2005; Callister & Rethwisch, 2009). As the ice grows, the liquid to solid phase transformation releases latent heat, ΔH_f, that increases the temperature of the material locally and slows down the ice growth. An empirical approach is used to account for the sudden latent heat release produced by undercooling. This model is also used to describe, analyze, and interpret the experimental data obtained from low-temperature LGCC tests (Farnam, Bentz, Sakulich et al., 2014; Farnam, Bentz, Hampton et al., 2014).

6.1 NUMERICAL SIMULATION

The main objective of this study was to predict the thermal response of a mortar (considered at a macroscopic scale) that is experiencing phase transformations during a reduction and subsequent increase in specimen temperature (i.e., a freezing and thawing cycle). The goal of the simulations was to quantify the fraction of pore solution that can freeze in an undercooled mortar specimen. The temperature of the specimen can be tracked by solving the heat (energy balance) equation and considering the frozen fraction of the pore solution. The governing equation for the heat transfer within a mortar specimen can be determined using the energy balance Equation 4 (Incropera, DeWitt, Bergman, & Lavine, 2006).

$$\frac{\partial}{\partial x}\left[k_m(T)\cdot\frac{\partial T(x,t)}{\partial x}\right]+q_{gen}-q_{loss}=\rho_m(T)\cdot C_m^p(T)\cdot\frac{\partial T(x,t)}{\partial t} \tag{4}$$

where $T(x,t)$ is the temperature at location $x(mm)$ and time t(sec), $k_m(T)$ is the thermal conductivity of the mortar specimen $[W/(m\cdot K)]$ at temperature T, $\rho_m(T)$ is the density of the mortar specimen $(kg/m\text{^}3)$ at temperature T, C_m^p is its specific heat capacity $[J/(kg\cdot K)]$ at temperature T, q_{gen} is the rate of generated or consumed heat from any phase change of the pore solution $[J/(m^3\cdot \text{sec})]$, and q_{loss} is the rate of heat dissipation (to the environment) in the experiment $[J/(m^3\cdot \text{sec})]$.

Equation 5-a describes the incorporation of a released/absorbed latent heat term, q_{gen}, associated with freezing/melting of the pore solution within a mortar specimen. A heat sink term, q_{loss} is also included, as shown in Equation 5-b, to calculate the rate of heat dissipation to the environment (even though insulation is present). This heat term is considered as a fraction of the rate of generated latent heat to simulate the significant heat exchange between the mortar specimen and its surroundings in the lateral directions. Equation 5-c is the difference between the heat generated and the heat lost.

$$q_{gen}=\Delta H_f\cdot\rho_{soln}\cdot v_P\cdot\frac{\partial[v_F(T)\cdot\xi(T)]}{\partial t} \tag{5-a}$$

$$q_{loss}=\Delta H_f\cdot h_{loss}\cdot\rho_{soln}\cdot v_P\cdot\frac{\partial[v_F(T)\cdot\xi(T)]}{\partial t} \tag{5-b}$$

$$q_{gen}-q_{loss}=\Delta H^m{}_f\cdot\rho_{soln}\cdot v_P\cdot\frac{\partial[v_F(T)\cdot\xi(T)]}{\partial t} \tag{5-c}$$

where ΔH_f is the latent heat of fusion(kJ/kg), ρ_{soln} is the density of pore solution(kg/m^3), v_p is the total volume fraction of pores within the mortar specimen (0 to 1), $v_F(T)$ is the volume fraction of the pore solution that can freeze at temperature T (0 to 1), $\xi(T)$ is the frozen volume fraction of freezable pore solution with salt at temperature T (0 to 1), h_{loss} is the heat dissipation coefficient (<1), and $\Delta H_f^m=\Delta H_f\cdot(1-h_{loss})$ is the apparent latent heat measured considering heat dissipation during phase transformation in the system (< ΔH_f).

6.2 FROZEN FRACTION OF PORE SOLUTION WITHOUT SALT, $v_F(T)$

The mortar specimens contain a pore structure with a broad range of sizes. The pore size can alter the freezing temperature of water (Scherer, 1999; Mehta & Monteiro, 2006; Beddoe & Setzer, 1988). To determine the pore size distribution in the mortar specimen and thus to calculate $v_F(T)$, a desorption isotherm was obtained for the mortar using a dynamic vapor sorption analyzer (TA Q5000). The vacuum saturation method was used to fully saturate the mortar specimen (i.e., D_S = 100 %). Therefore, all of the pores, including air voids, were filled with water to investigate the role of curvature of the pores on the thermal behavior of the mortar. For melting, the pore size distribution obtained from an absorption isotherm was used (Litvan, 1972). Figure 37 provides the desorption-absorption isotherm for the mortar specimen and it correlates the degree of saturation (D_S) to the relative humidity (RH), which is the amount of water vapor present in the specimen expressed as a percentage of the amount needed for saturation at the same temperature (Villani et al., 2015). A characteristic hysteresis is observed in the desorption-absorption isotherm in Figure 37, at least partially due to the presence of "ink-bottle" pores.

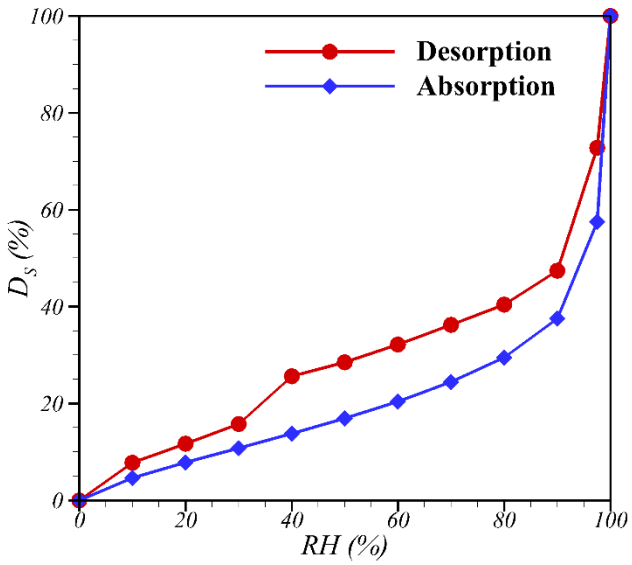

Figure 37. Desorption-Absorption Isotherms of Mortar Specimen

To calculate $v_F(T)$, two approaches were evaluated in this study: (1) a model with explicit consideration of a continuous pore size distribution, and (2) a phenomenological model with consideration of only a discrete pore size distribution. The first approach considers the effect of all pore sizes on the freezing process, and $v_F(T)$ varies continuously as the temperature changes. In the second approach, the effect of a discrete pore size distribution on ice formation inside the mortar specimen is simplified and a phenomenological model is adapted to simulate the freezing process of water inside the mortar specimen (it considers only two classes of pores: large pores that include all pores except gel pores (capillary and air-entrained or air-entrapped pores), and small pores (known as gel pores)).

In the phenomenological model, $v_F(T)$ is considered to be a constant value based on three main classes of pores: (1) gel pores, (2) capillary pores, and (3) air-entrained or air-entrapped pores. To investigate the accuracy of these two approaches, the LGCC test conducted by Farnam, Bentz, Sakulich et al. (2014) and Farnam, Bentz, Hampton et al. (2014) was simulated using these two models with consideration of continuous and discrete pore sizes, respectively. Also the thermal behavior of the mortar specimens saturated with water was compared with experimental results obtained in a temperature range between 24 °C and -35 °C.

6.2.1 A Model with Consideration of a Continuous Pore Size Distribution

Equation 6 describes the Gibbs-Thomson equation that relates the freezing temperature of a liquid inside a porous material to the pore radius.

$$\frac{2\gamma_{CL}}{r^*} \approx \left(\frac{S_L - S_C}{V_L}\right)\left(T_m - T_f(r^*)\right) \tag{6}$$

where γ_{CL} is the crystal/liquid interfacial energy (J/m^2), r^* is the radius of the pore for homogeneous nucleation (m), S_L and S_C are the molar entropies of the liquid and crystalline phases $[J/(mol \cdot K)]$, V_L is the molar volume of the liquid (m^3/mol), T_m is the melting temperature (K), and T_f is the freezing temperature as a function of pore radius (K) (Sun & Scherer, 2010b; Brun, Lallemand, Quinson, & Eyraud, 1977). Therefore, the temperature at which ice begins to form can be predicted as a function of critical pore radius r^* by solving Equation 6 for T_f (Sun & Scherer, 2010a, 2010b, 2010c).

Figure 38 displays the relationship between the size of the pore and the temperature that is needed to freeze water inside the pore, $T_f(r^*)$. At a temperature above $T_f(r^*)$, no phase transformation occurs inside the pores with radius less than r^*. Once the temperature reaches the associated freezing temperature, ice begins to form inside the pores with radii of r^*. Afterwards, ice propagates into the smaller pores, but only as the temperature drops further. This process is reversed during melting.

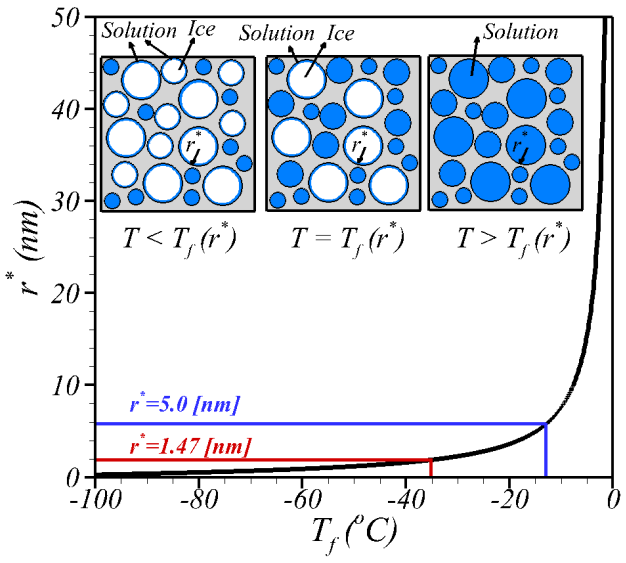

Figure 38. Effect of Pore Size on the Freezing Temperature of Water Using the Gibbs-Thomson Equation, Including a Schematic of Ice Formation in a Porous Material (inset)

The Kelvin-Young-Laplace equation can be used to correlate the pore radius to the relative humidity (RH) in a water-filled pore as described in Equation 7 (Radlinska et al., 2008; Henkensiefken, Bentz, Nantung, & Weiss, 2009).

$$r^* = \left(\frac{2\gamma}{\ln(RH)}\right)\cdot\left(\frac{V_m}{RT}\right) \tag{7}$$

In this study, the Kelvin-Young-Laplace equation (Equation 7) was used alongside the Gibbs-Thomson equation (Equation 6) to obtain the relationship between $v_F(T)$ and pore size in the mortar specimen based on its measured desorption-absorption isotherm (Figure 37). At a temperature of -35 ºC, solution absorbed into the mortar pores with sizes greater than 1.47 nm is susceptible to freezing as shown in Figure 38. Figure 38 also displays the process of ice formation in a porous material, as the ice forms inside the larger pores initially. Ice invades into the smaller pores progressively as the temperature drops. Figure 39 shows that 72% of the solution absorbed in the pores by volume can freeze between 0 °C and -35 °C. For the case of melting, the formed ice in the pores is similarly considered to melt gradually according to the Gibbs-Thomson equation (Equation 6). In this work, it is assumed that $1 = v_{air} + (D_S/100)$ and $(D_s/100) = v_w(r < r^*) + v_F(r > r^*)$, where v_{air} and v_w are the volume fraction of air and non-freezable pore solution in the total pores (0 to 1), respectively. To investigate the role of pore sizes, all of the pores with various sizes are assumed to be filled with water in this section, i.e., $v_{air} = 0$. It should be mentioned that the LGCC test was conducted within a temperature range between 24 °C and -35 °C.

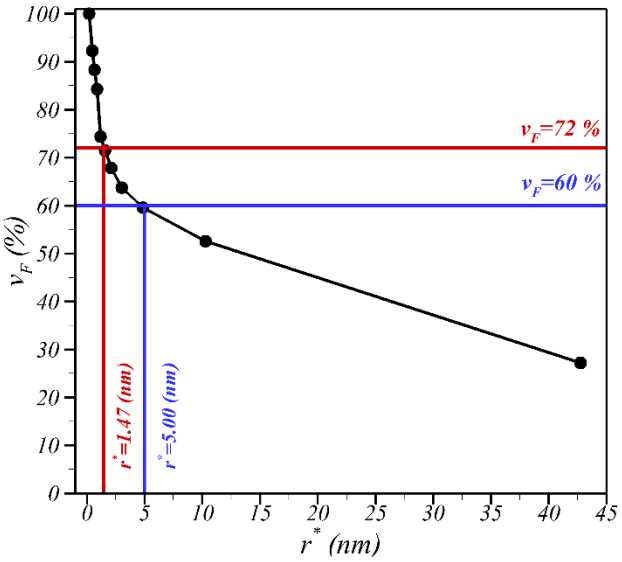

Figure 39. Volume Fraction of Pore Solution That Can Freeze as a Function of the Critical Nucleus (pore) Size

6.2.2 A Phenomenological Model with Consideration of a Discrete Pore Size Distribution

Although the continuous pore size distribution can be estimated to determine the volume fraction of freezable pore solution, this measurement is generally not available for field/commercial concretes. In this study, a phenomenological model was developed to use in practice, when knowledge of the continuous pore size distribution is not available. Since the freezing and thawing responses of most cementitious systems are dominated by the category of relatively large pores (i.e., capillary, air-entrained, and air-entrapped pores), a discrete pore size of 5 nm (a predefined critical pore size as the division between gel and capillary pores) can be used as a criterion to differentiate the freezable and non-freezable pore solution (Young, 1988; Li et al., 2012; Yang, Weiss, & Olek, 2006). For a mortar sample saturated with deionized water, this critical pore radius corresponds to a relative humidity (RH) equal to 81%, at which point all of the gel pores are filled by solution (Radlinska et al., 2008).

The corresponding freezing temperature of water in pores with a size of 5 nm is about -13 ºC according to the Gibbs-Thomson equation as displayed in Figure 38. Figure 39 displays the relation between derived volume fraction of freezable pore solution; v_F from associated relative humidity measured in experiments; and pore radius, r^*, using Equation 7. The corresponding volume fraction of freezable pore solution, v_F, in pores with size greater than 5 nm is measured to be 60% with respect to the total volume fraction of pores displayed in this figure. Consequently, the volume of freezable pore solution in the phenomenological model is underestimated by about 16% with respect to the model with direct consideration of pore size distribution assuming pure water to be the solution in the pores. This implies that 60% of the total solution by volume, corresponding to the solution that is absorbed into large pores (i.e., capillary pores, air-entrained pores, and air-entrapped pores) begins to transform to ice instantaneously, and the gradual process of ice formation in the remainder of the freezable pores (i.e., smaller pores, containing a lower volume fraction) will be neglected. Therefore, the radius

of curvature (pore size) would have a relatively small impact on the macroscopic freezing response of the air-entrained mortar specimen and the approach of a discrete pore size distribution will be implemented in the numerical model to investigate the thermal behavior of mortar specimens containing NaCl solutions.

6.3 FROZEN FRACTION OF PORE SOLUTION WITH SALT, $\xi(T)$

For the case where the pores are water-filled (0% NaCl), the value of $\upsilon_F(T)$ can be used to determine the latent heat released/absorbed when the temperature of the specimen reaches freezing/melting temperatures. In the case where the pores are filled with NaCl solution, the presence of this salt alters the freezing/melting behavior. The phase equilibrium of NaCl solution is shown in Figure 40. In this figure, the liquidus line shows the point at which ice begins to form within the NaCl solution. Above the liquidus line, no ice may be detected (i.e., point 1 in Figure 40). A mixture of ice and salt solution with varying concentration that follows the liquidus line exists between the liquidus and eutectic temperatures (T_{eut}= -21.1 °C), which is commonly known as the freezing region (i.e., point 2). At T_{eut} (i.e., the eutectic line), the formation of ice is complete and all the solution converts to a solid eutectic composition as the temperature of the solution decreases further. Below this temperature, it is assumed that no solution exists in the capillary, air-entrained, and air-entrapped pores. According to solidification principles (Askeland & Pradeep, 2003), the lever rule can be used to determine the amount of ice when the specimen temperature is between the liquidus and eutectic lines.

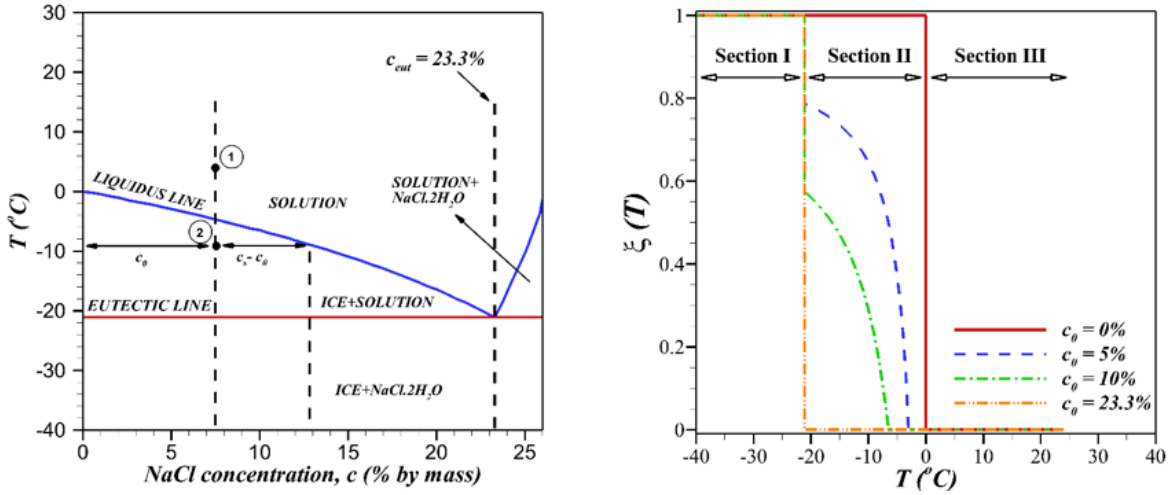

(a) (b)

Figure 40. Phase Diagram for Aqueous NaCl Solution (Sourirajan & Kennedy, 1962) (a) and the Fraction of Produced Ice as a Function of Temperature Within the Freezing Region for Bulk NaCl Solution (b)

The frozen fraction of the freezable pore solution $\xi(T)$was used in the numerical simulation to calculate the amount of latent heat released/absorbed during freezing/melting at each time step for the mortar specimen saturated with NaCl solution. The lever rule, given in Equation 8, was employed in this study as a tool to compute the amount of produced ice within the freezing region for NaCl solutions in a mortar specimen.

$$\xi(T) = \frac{c_s(T) - c_0}{c_s(T)} \tag{8}$$

where $c_s(T)$, the concentration of the ice solution mixture, can be estimated as a function of solution temperature by using Equation 9 (Farnam et al., 2014):

$$c_s(T) = a_2 \cdot T^2(x,t) + a_1 \cdot T(x,t) + a_0 \qquad -35^oC \le T(x,t) \le 24^oC \tag{9}$$

where a_0=0.003385, a_1=-0.016362 [1/(°C)], a_2=-0.000264 [1/(°C^2)], and c_0 is the initial concentration of NaCl solution above the liquidus line by mass (%). The coefficients in Equation 9 fit the $c_s(T)$ curve on data points derived from the phase diagram of aqueous NaCl solutions with R^2=0.999 as the measure of goodness-of-fit.

The frozen fraction of the freezable pore solution $\xi(T)$ was calculated for bulk solutions containing 0%, 5%, 10%, and 23.3% NaCl (by mass) and is depicted in Figure 40. This figure is divided into three temperature ranges for solution with NaCl concentrations of 0%, 5%, 10%, and 23.3%:

(1) -35 °C ≤ $T(x,t)$ ≤ -21.1 °C = T_{eut}, where the temperature of solution is below T_{eut} and the entire solution solidifies;
(2) -21.1 °C ≤ $T(x,t)$ ≤ 0 °C, where both liquid and solid phases (i.e., ice and solution) coexist; and
(3) 0 °C < $T(x,t)$ ≤ 24 °C, where no phase transformation occurs and the solution remains in its liquid state.

Ice formation or solidification of eutectic composition requires removal of sufficient heat/energy to compensate for the latent heat associated with the phase transformation. A considerable amount of latent heat can be released during solidification. Eutectic latent heat for NaCl solution was measured using a low-temperature differential scanning calorimeter and obtained to be ΔH_{eut} = 135 kJ/kg ±5 kJ/kg. The standard deviation for eutectic latent heat was determined on three mortar specimens containing NaCl solution with 5%, 10%, and 23.3% NaCl concentrations. The latent heat associated with ice formation was also considered to be ΔH_{ice}= 332.4 kJ/kg ± 2 kJ/kg over the range of -35 °C ≤ $T(x,t)$ ≤ 0 (Han et al., 2006; Sun & Scherer, 2010b; Brun et al., 1977). The heat of fusion $\Delta H_{melting}$ was given with a relative error < 0.25% by Equation 10 (Sun & Scherer, 2010b):

$$\Delta H_{melting}(T)(kJ/kg) \approx 333.8(kJ/kg) + 1.79[kJ/(kg \cdot K)] \cdot (T - T_m) \tag{10}$$

The rate of ice formation within mortar pores was considered in the numerical simulation by evaluating $\xi(T)$.

6.4 EFFECTIVE THERMAL PROPERTIES OF MORTAR SPECIMEN

To develop a reliable numerical simulation at the macro-scale, it is essential to properly define the material properties. This section discusses how the thermal properties of the mortar specimen

as a composite are defined for the proposed finite difference model with the consideration of two approaches concerning the distribution of pore sizes, namely continuous and discrete.

6.4.1 Thermal Conductivity

The effective medium theory (EMT) (Levy & Stroud, 1997) can be used to define properties of a composite material for a heterogeneous mixture. For mortar specimens either partially or fully saturated with water or fully saturated with NaCl solution at different concentrations, the thermal conductivity of the mortar (k_m) was estimated using the EMT formulation as described in Equation 11 and shown in Figure 41:

$$k_m = k_{dry} \cdot \frac{2(1-\nu_P)\cdot k_{dry}+(1+2\nu_P)\cdot k_P}{(2+\nu_P)\cdot k_{dry}+(1-\nu_p)\cdot k_P} \tag{11}$$

where k_{dry} is the thermal conductivity of the dry mortar specimen, k_p is the thermal conductivity of the material in the pores, and v_p is again the total volume fraction of pores.

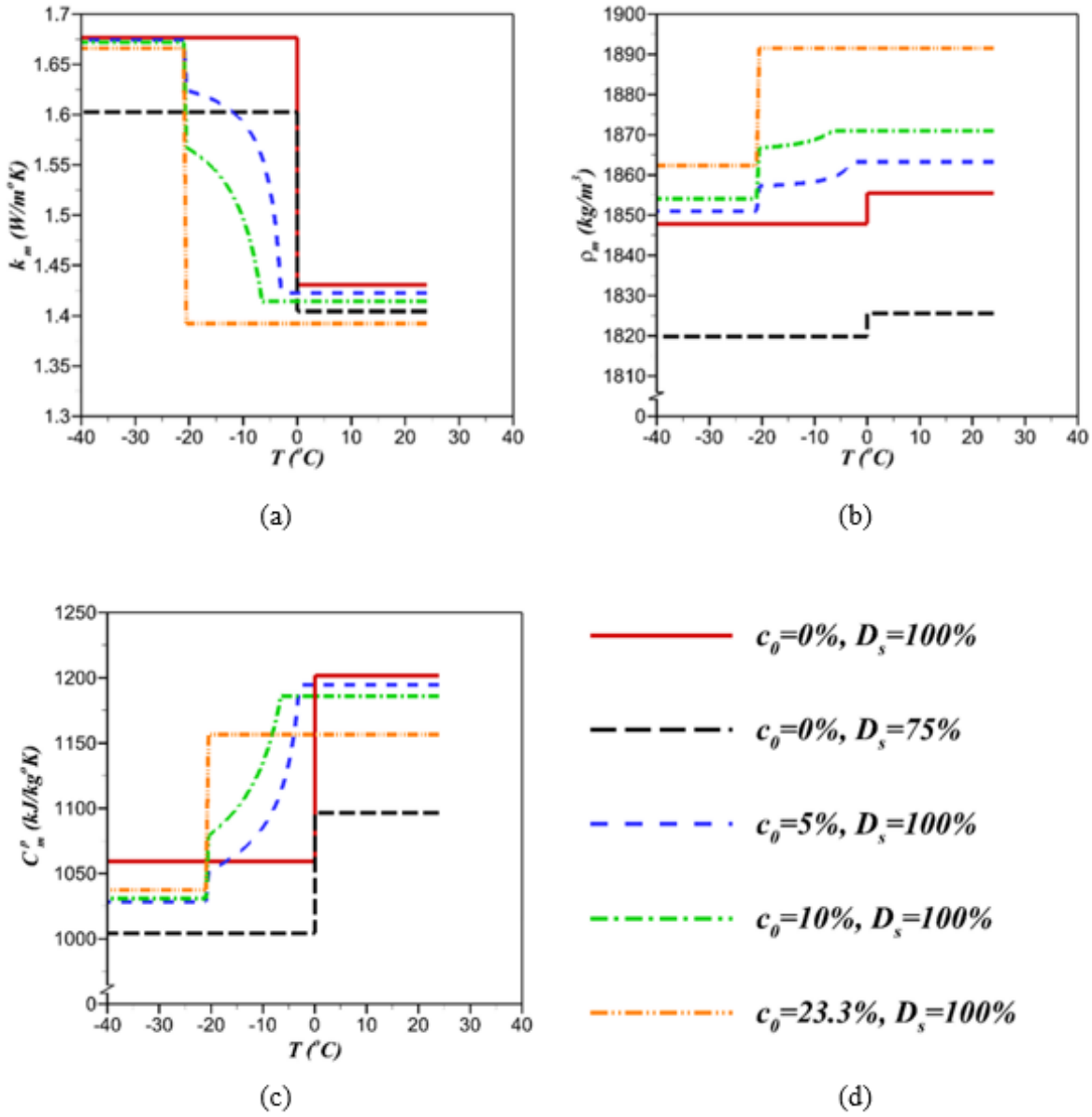

Figure 41. Calculated Effective (a) Thermal Conductivity(k_m), (b) Density(ρ_m), (c) Specific Heat Capacity ($C\_m\^p$) as a Function of Temperature for Mortar Specimens Containing, and (d) Various Concentrations of NaCl Solutions and Different Degrees of Saturation

Depending on the temperature and saturation state, pores in the mortar specimen might contain various constituents including air, ice, or NaCl solutions with different concentrations. The amount of solution and air in the mortar depends on its degree of saturation (D_S). The temperature of the mortar specimen can also change the amount of solution and ice in mortar pores as described in Sections 6.2 and 6.3. The change in the amount of air, ice, or solution can substantially alter the thermal conductivity of the mortar specimen due to the considerable differences between the thermal conductivities of air, solid ice, and solution (Table 18).

A parallel model (Progelhof, Throne, & Ruetsch, 1976) was employed to determine the effective k_P as a function of the volume fractions and thermal conductivities of each component (i.e., k_{air}, k_{ice}, and k_{soln}), as described in Equation 12.

$$k_P = k_{air} \cdot v_{air} + v_f \cdot [k_{ice} \cdot \xi + (1 - \xi)k_{soln}] + k_{soln} \cdot v_w \quad (12)$$

where k_{air} is the thermal conductivity of air, $v_{air} = 1 - (D_S/100)$ is the volume fraction of air in the mortar pores, k_{ice} is the thermal conductivity of ice, and k_{soln} is the thermal conductivity of the remnant pore solution within the mortar pores. Following the work of Farnam (Farnam, Bentz, Sakulich et al., 2014), no considerable changes of dimensions of the mortar specimens were observed. Therefore, the volume change is neglected in the thermal modeling of a macro-scale mortar specimen
($v_{air} = 1 - (D_S/100)$). However, the variation of physical and thermal properties of components of the mortar specimen could lead to a change in the volume of a micro-scale specimen.

Note that the unfrozen solution might exist in (1) smaller pores with an invariable NaCl concentration, and (2) larger pores that contain frozen solution (ice) and a NaCl solution with a higher concentration. The thermal properties of NaCl solution in the smaller pores are provided in Table 18; however, the thermal properties of NaCl solution with variable concentration in the larger pores can be determined knowing the frozen fraction and the lever rule. The corresponding thermal conductivities of air, ice, NaCl solution with different concentrations, and dry mortar are also provided in Table 18.

Table 18. Properties of Air, Ice, and NaCl Solution with Different Concentrations

Material	k (W/(m·K))	ρ (kg/m^3)	C^p (kJ/(kg·K))
Air (Touloukian; Hilsenrath et al., 1956)	0.023	1.35	1.005
Ice (Fletcher, 2010)	2.25	934	2030
0% NaCl solution (Pitzer, Piper, & Busey, 1984)	0.5886	997	4121
5% NaCl solution (Pitzer, Piper, & Busey, 1984)	0.5611	1036	3947
10% NaCl solution (Pitzer, Piper, & Busey, 1984)	0.5336	1074	3773
23.3% NaCl solution (Pitzer, Piper, & Busey, 1984)	0.46	1178	3310
Dry mortar (Campbell-Allen & Thorne; 1963; Daian, 1988; Bentz, Peltz, Duran-Herrera, Valdez, & Juarez, 2010)	1.7	2070	850

6.4.2 Density, ρ

The law of mixtures (a weighted mean) can be used to predict the density of a composite material. An effective density for mortar specimens (ρ_m) was estimated using the law of mixtures and is described in Equation 13 and shown in Figure 41(b).

$$\rho_m = \rho_{dry} \cdot (1 - v_P) + \rho_P \cdot v_P \tag{13}$$

where ρ_{dry} is the density of the dry mortar and ρ_P is the effective density of the materials in the mortar pores (i.e., air, ice, and solution).

The law of mixtures was again employed to obtain the effective density of the materials in the mortar's pores (i.e., ρ_P) as described in Equation 14.

$$\boldsymbol{\rho_P = \rho_{air} \cdot v_{air} + v_F \cdot [\rho_{ice} \cdot \xi + (1 - \xi) \cdot \rho_{soln}] + \rho_{soln} \cdot v_w} \tag{14}$$

where ρ_{air}, ρ_{ice}, and ρ_{soln} are the densities of air, ice, and solution, respectively. The corresponding densities of air, ice, NaCl solution with different concentrations, and dry mortar are also provided in Table 18.

6.4.3 Specific Heat Capacity, C^p

The process of determining an effective specific heat capacity is conceptually similar to determining an effective density (Zhou, Wang, Peng, Du, & Yang, 2010). The effective specific heat capacity for a composite mortar specimen C_m^p was calculated using Equation 15 and is shown in Figure 41(c).

$$\boldsymbol{C_m{}^p \cdot \rho_m = C_{dry}{}^p \cdot \rho_{dry} \cdot (1 - v_P) + C_P{}^p \cdot \rho_P \cdot (v_P)} \tag{15}$$

where C_{dry}^p is the specific heat capacity of the dry mortar and C_P^p is the effective specific heat capacity of materials in the mortar pores (i.e., air, ice, and solution) which can be calculated using Equation 16.

$$C_P^p \cdot \rho_P = C_{air}^p \cdot \rho_{air} \cdot v_{air} + \left\{ \begin{array}{l} v_F \cdot \left[C_{ice}^p \cdot \rho_{ice} \cdot \xi + C_{soln}^p \cdot \rho_{soln} \cdot (1 - \xi) \right] \\ + C_{soln}^p \cdot \rho_{soln} \cdot (v_w) \end{array} \right\} \tag{16}$$

where C_{air}^p, C_{ice}^p, and C_{soln}^p are the specific heat capacities for air, ice, and solution, respectively. The corresponding specific heat capacities of air, ice, NaCl solution with different concentrations, and dry mortar are provided in Table 18.

6.5 CONFIGURATION OF NUMERICAL SIMULATION AND BOUNDARY CONDITIONS

Following the work by Farnam, Bentz, Sakulich et al. (2014), the LGCC test was simulated to quantify heat flow and predict the temperature profiles of the mortar specimens. Two types of

experimental data were used: (1) fully saturated mortar specimens (i.e., 100% degree of saturation) with solutions containing 0%, 5%, 10%, and 23.3% NaCl (by mass), and (2) specimens saturated partially with water (i.e., no NaCl involved in the solution) at degrees of saturation equal to 75%, 85%, 95%, and 100%. The procedures used for preparation of fully saturated and partially saturated mortar specimens were addressed in previous experimental works (Farnam, Bentz, Sakulich et al., 2014; Farnam, Dick, Wiese et al., 2015; Farnam, Esmaeeli, Bentz, & Zavattieri, 2015).

The experimental conditions of one-dimensional heat transfer were provided in the LGCC experiment by using a heat sink at the bottom, longitudinal insulation on the sides, and foam as a thermal insulation around the system to minimize the heat dissipation from the experimental apparatus (Figure 42(a)). However, a difference between the measured released heat in an LGCC experiment and the associated enthalpy of fusion of PCMs (i.e., methyl laurate and paraffin oil), likely due to experimental imperfections (e.g., thermal bridges, heat leaks), was observed. Therefore, h_{loss}, a heat loss coefficient, is employed to simulate the energy dissipation in the experimental system which is estimated as a 40% to 60% heat loss (Farnam, Krafcik, Liston, Washington et al., 2016). The advection of heat to simulate the water transport occurring during the freeze-thaw cycle is neglected in this numerical investigation.

Two reference (meter) bars made of Pyroceram code 9606 with known thermal properties were used to measure the heat flow passing through the mortar specimen in the experiment (see Figure 42(a)).

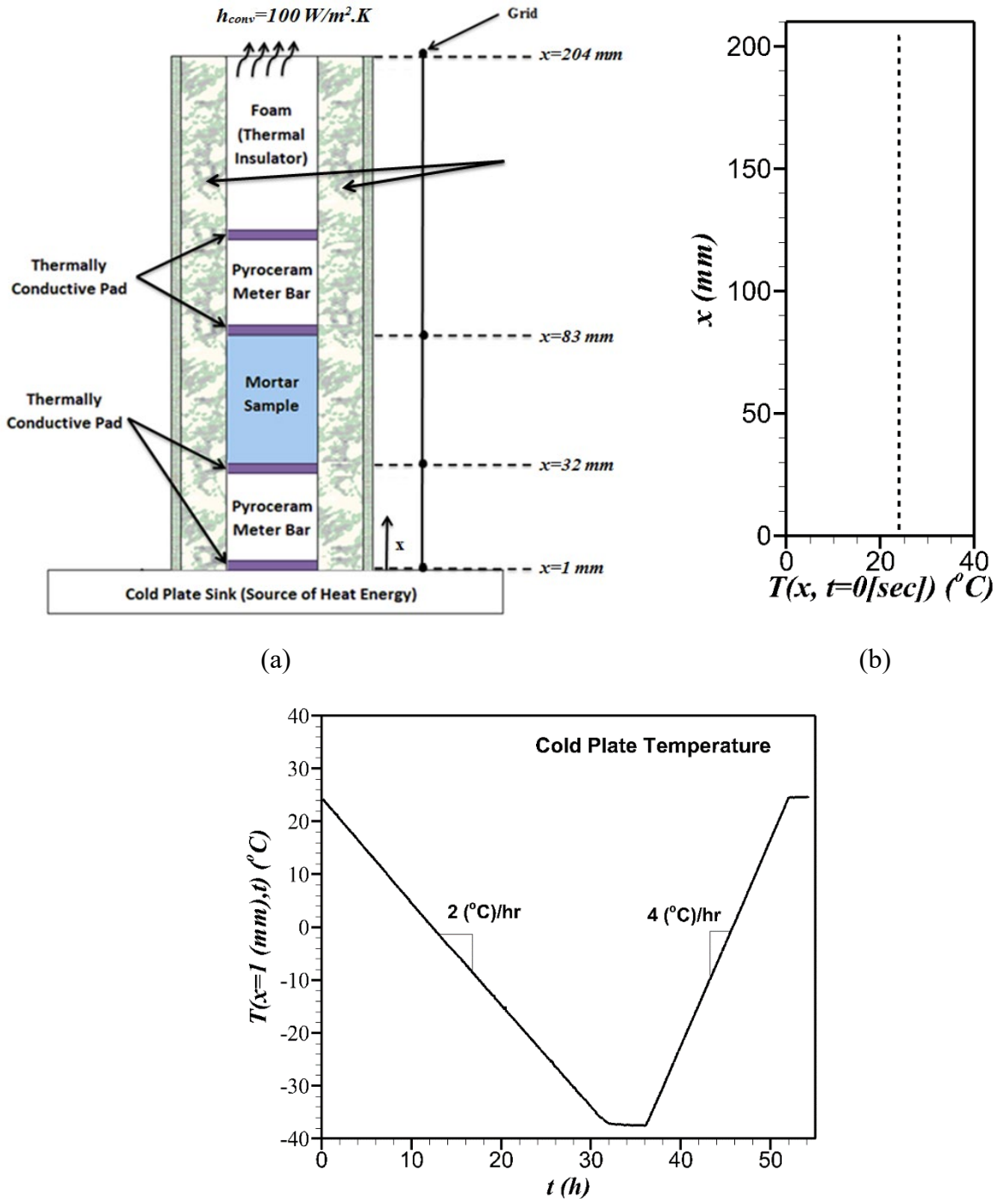

Figure 42. The LGCC Experiment with Adapted Finite Difference Nodes (a), Initial Temperature of Finite Difference Simulation, (i.e., $T(x,t=0)$) (b), and Temperature at the Bottom of the LGCC Experiment, (i.e., $T(x=1,t)$, as a function of time) (c)

The first step in the numerical approach was to discretize the experimental setup by a finite difference method using an appropriate grid spacing size, Δx of 1 (mm) and time step, Δt of 0.05 (sec). The initial temperature of the entire experimental setup was set equal to the ambient temperature $T\ (x,\ t{=}0) = 24$ (°C) as displayed in Figure 42(b). The temperature at the bottom of the LGCC experiment, $T\ (x = 1\ mm,\ t)$ (see Figure 42(a)) varied in the numerical simulation as a function of time according to the LGCC experimental protocol (Figure 42(c)). A heat convection coefficient $h_{conv} = 100$ W/(m^2·K) is employed to simulate the heat transfer between the air and the foam on the top (Incropera et al., 2006). Even though the insulating foam has a small thermal diffusivity parameter, significant heat energy is still transferred to the environment, resulting in a slight temperature differential between the top of the foam and the ambient environment. The relevant thermal properties of the thermally conductive pad, foam, and Pyroceram code 9606 used in the modeling are listed in Table 19.

Table 19. Properties of Thermally Conductive Pad, Foam, and Pyroceram Code 9606

Material	k (W/(m·K))	ρ (kg/m^3)	C^p (kJ/(kg·K))
Thermal Pad	3.0	309	850
Foam (Williams & Aldao, 1983)	0.03	20	1,340
Pyroceram Code 9606 (Farnam, Bentz, Sakulich et al., 2014)	*	2600	900

*The thermal conductivity of Pyroceram code 9606 as a meter bar material was calculated as a function of temperature (Farnam et al., 2014).

Figure 43 displays a flow chart of the one-dimensional explicit finite difference method adopted to simulate the saturated mortar specimen containing deionized water and NaCl solution with various concentrations. First, the thermal properties of components of the mortar specimen, temporal and spatial step sizes, and thermal initial and boundary conditions are determined. All the discretized layers (i.e., x = 1 mm to x = 204 mm) are employed to simulate the heat transfer for the LGCC experiment; however, only the finite layers of the mortar specimen (i.e., x = 32 mm to x = 83 mm) are investigated in this figure. During phase transformation of the pore solution in the mortar specimen filled with deionized water, two approaches of consideration of either a discrete pore size distribution or a continuous pore size distribution were employed, as discussed in section 3. The approach of using a distribution of continuous pore sizes introduces a progressive ice formation/melting in the pores that is simulated using Equations 6 and 7 and as shown in Figure 37; however, the volume fraction of pores with the size greater than 5 nm ($v_F = 60\%$) is considered to simulate the instantaneous ice formation/melting occuring in the approach of using discrete pore sizes. Additionally, the progressive fraction of produced/melting ice is calculated using the lever rule as discussed in Section 6.3.

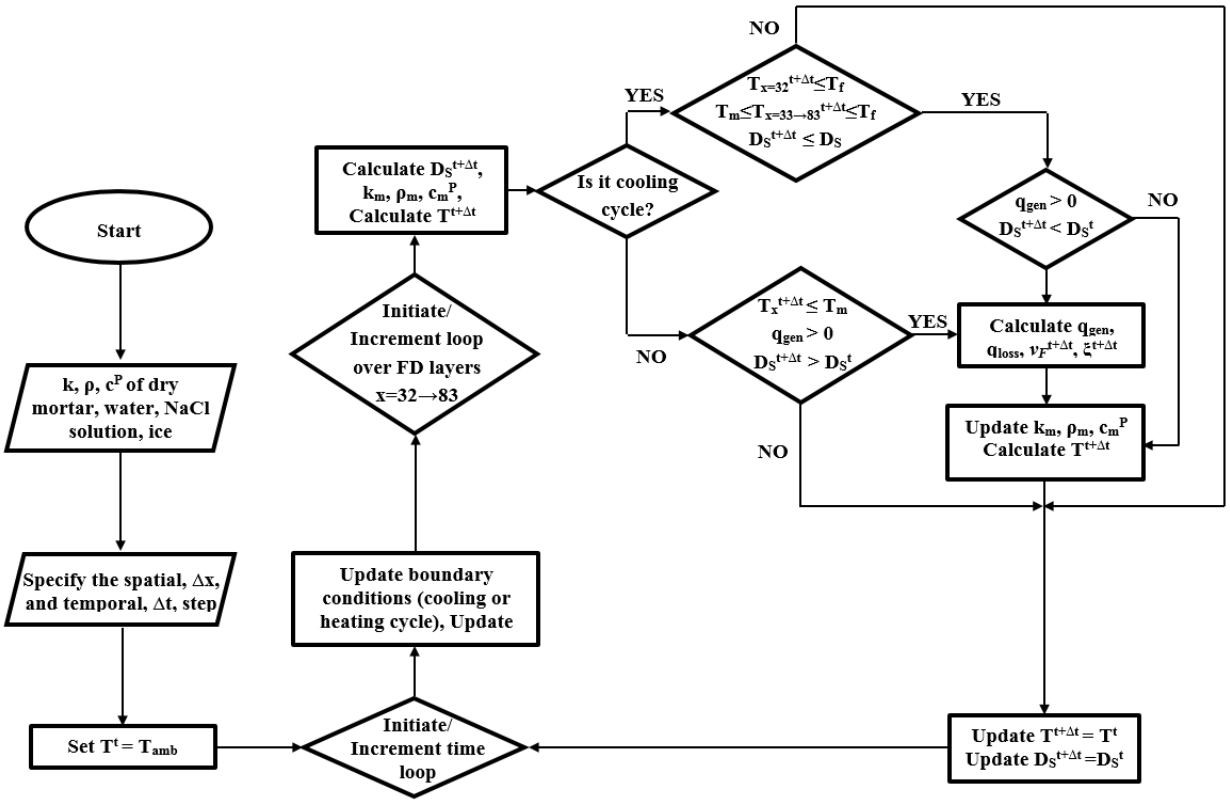

Figure 43. Numerical Algorithm of Finite Difference Strategy Using Heat Transfer Equation to Simulate the Thermal Behavior of a Saturated Mortar Specimen

6.6 UNDERCOOLING

The freezing temperature T_f is the point at which solidification of a liquid occurs, whereas a melting temperature T_m is the point at which a solid melts. In most materials, T_f is usually lower than T_m because of undercooling (Askeland & Pradeep, 2003; Debenedetti & Stanley, 2003; Wilding, 1992). Therefore, no ice can be formed until the temperature reaches T_f (see Figure 40(a)). The values of T_f and T_m are obtained directly from the LGCC experiment (Farnam, Bentz, Sakulich et al., 2014) and are reported in Table 20.

Table 20. Freezing and Melting Points of Saturated Mortar Specimens with NaCl Solutions (Farnam, Bentz, Hampton, & Weiss, 2014)

NaCl Solution Concentration (%)	Freezing Point T_f (°C)	Melting Point T_m (°C)	Amount of Undercooling with Respect to Liquidus Line**
0	-6.1	0.0	-6.1
5	-10.8	-3.0	-7.8
10	-12.0	-6.5	-5.5
23.3*	-21.1	-21.1	0

* For specimens containing 23.3% NaCl solution, the freezing point and melting point are identical (T_{eut}) because these points are located at the eutectic line and the entire solution only forms eutectic solid during solidification.
** The amount of undercooling is calculated by subtracting the melting point T_m from the freezing point T_f of the corresponding bulk NaCl solution.

The specimen size and cooling rate of the specimen can alter the degree of undercooling (Beddoe & Setzer, 1988). In general, less undercooling is observed for larger specimens (greater chance of a suitable nucleation source being present), while more undercooling is observed when a greater cooling rate is employed. In the LGCC test (using a 25-mm x 25-mm x 50-mm mortar specimen size), freezing was observed at -6.1 ºC when the mortar was saturated with water.

When the temperature of the bottom layer reaches T_f, the layers with temperatures lower than T_m can begin to produce ice instantaneously, and thus, the associated heat release results in increasing the temperature toward T_m. Subsequently, the temperature of the layer remains unchanged at T_m until the entire liquid within that layer transforms into ice. Since the numerical model with a discrete pore size distribution is considered to investigate the undercooling effect on thermal behavior of the mortar specimen, nearly 60% of the pores by volume (i.e., nearly all of the capillary pores, air-entrained pores, and air-entrapped pores) nucleate ice instantaneously for the case of the mortar specimen saturated with deionized water (solution with 0% NaCl concentration), as shown in Figure 44.

Figure 44 illustrates the effect of considering undercooling on the thermal behavior of the simulated mortar specimens saturated with deionized water solution compared with the model without undercooling. The heat loss coefficient, h_{loss}, is assumed to be a constant value of 60% in this figure. Similar to the observed experimental thermal behavior of the mortar specimen (Farnam, Bentz, Hampton, & Weiss, 2014), a temperature rise at the freezing point was observed in the phenomenological numerical model when undercooling was included, whereas no abrupt temperature ascent was observed without including undercooling. No considerable changes in the dimensions of the mortar specimens were measured during the freezing and melting processes in the experiment.

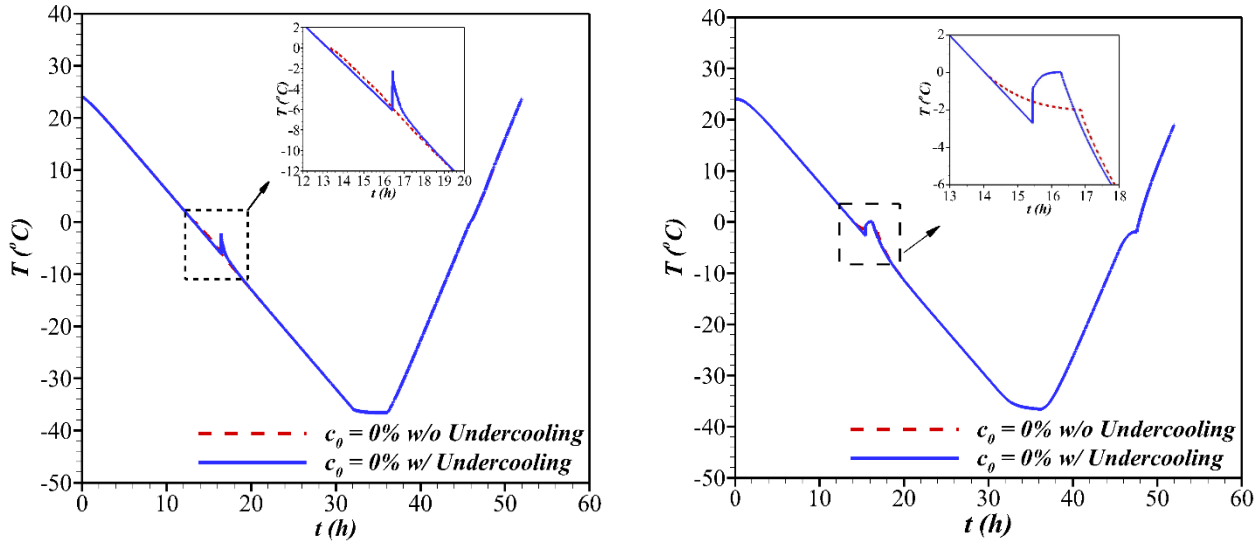

(a) (b)

Figure 44. Effect of Including Undercooling in the Numerical Simulation on Temperature Profile of Saturated Mortar Specimen Containing Water (0% NaCl) Exposed to One Freeze-Thaw Cycle at Different Locations of Mortar Specimen: (a) *x = 32 mm;* (b) at x = 83 mm

6.7 RESULTS

6.7.1 Mortar Specimens Saturated with Water

In this section, mortar specimens saturated with water at 75%, 85%, 95%, and 100% degrees of saturation (D_S) and the effect of pore size distribution are numerically investigated.

6.7.1.1 Fully Saturated Mortar Specimen

Two numerical models, with either a continuous or discrete pore size distribution, are investigated in this section. Figure 45 shows the experimental and numerical results for the thermal behavior of mortar specimens that were saturated (i.e., D_S = 100%) with water. The heat loss coefficient, h_{loss}, is assumed to be a constant value of 60% in this figure. The model with a discrete pore size distribution only considers the instantaneous freezing of the pore solution that can freeze ($v\_F = 60\%$), whereas the model with the continuous pore size distribution also considers an additional process of gradual freezing of the pore solution ($v_F = 72\%$) as displayed in Figure 45(c). Figure 45(a) indicates the numerical and experimental temperature profile for the saturated mortar specimen at the bottom layer in the LGCC experiment setup (i.e., x = 32 mm). A nearly instantaneous temperature rise that occurred at the moment of freezing can be observed, demonstrating the instantaneous freezing due to the temperature of the first finite difference layer of the mortar specimen (i.e., x = 32 mm) reaching the freezing temperature of (undercooled) water in the mortar specimen ($T_f = -6.1$ °C). However, the model with a continuous pore size distribution considers that the remaining amount of unfrozen water in the pores transforms to ice gradually until the temperature reaches -35 °C.

The model with a discrete pore size distribution considers the ice melting to occur by absorbing sufficient heat at the melting temperature of the large frozen pores observed in the experiment ($T_m = 0$ °C). In the model with a continuous pore size distribution included, the ice formed in the pores is considered to melt gradually starting at -35 °C (Sun & Scherer, 2010b), based on the measured absorption isotherm for the mortar.

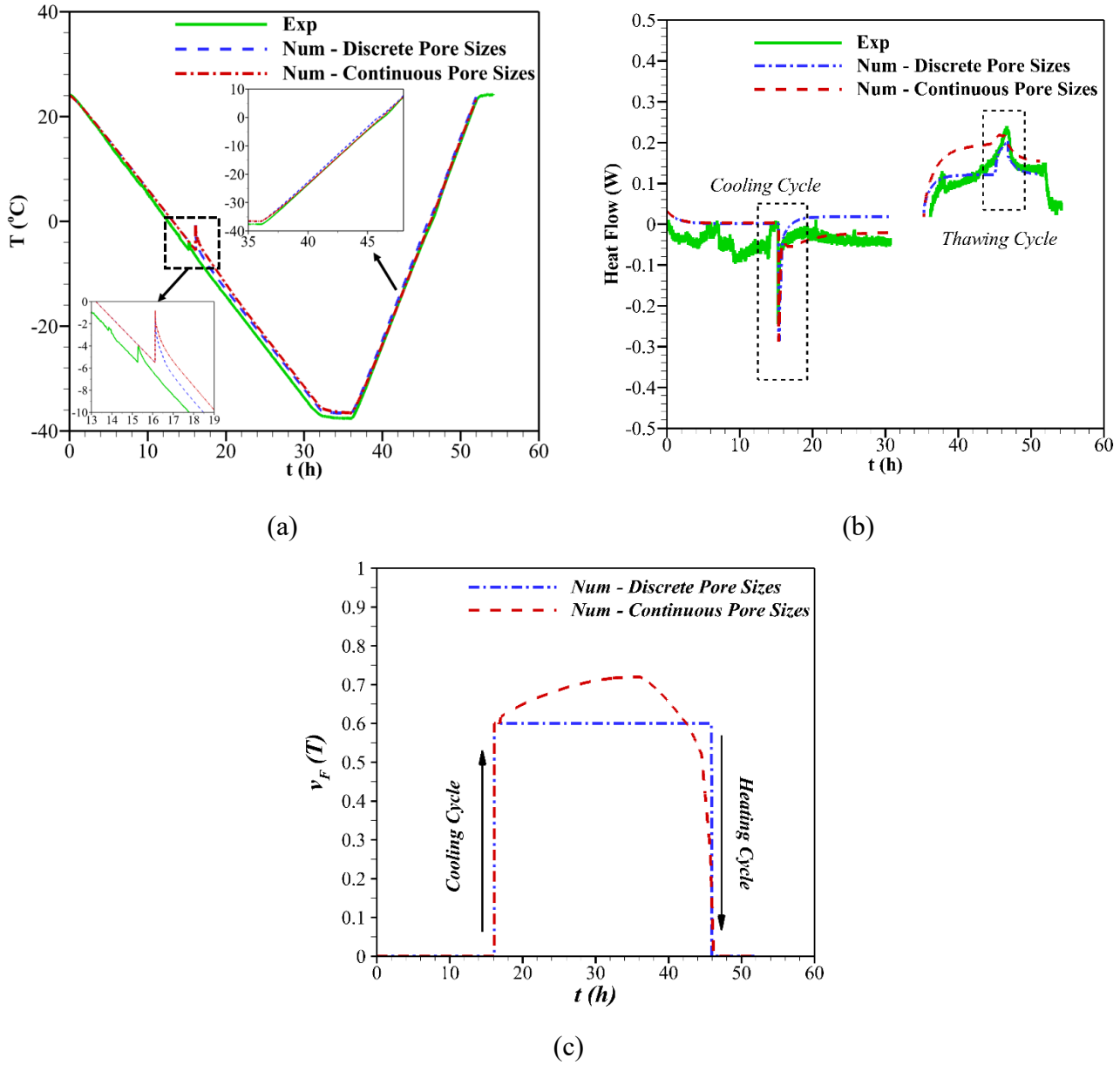

Figure 45. Experimental and Numerical Results for Mortar Specimen Fully Saturated with Water (a) Temperature Profiles at x = 32 mm; (b) Predicted Heat Flow; (c) Volume of Pore Solution Undergoes Phase Transformation at the Bottom Surface of the Mortar Specimen

The heat flow is obtained using the numerical simulation to evaluate the role of pore size distribution and compared to the experimental data shown in Figure 45(b). The formation of ice

in the pore solution results in an exothermic peak, which is representative of the latent heat release during a freezing cycle. In the model with a discrete pore size distribution, the exothermic peak is considered to occur at T_f and subsequently ceases when the entire amount of latent heat has been emitted to the surroundings. The endothermic peak begins as a gradual process at 0 °C, until all of the previously formed ice melts inside the frozen pores.

Conversely, the exothermic peak is extended to the end of the freezing cycle (-35 °C) due to gradual ice nucleation inside the smaller pores in the model with a continuous pore size distribution. For the case of melting, the endothermic peak is considered to occur gradually as a function of temperature and the pore size.

Therefore, the melting curve extends progressively to 0 °C, owing to the broad range of pore sizes in the model with a continuous pore size distribution. It was concluded that the consideration of pore size distribution can reasonably be neglected during the freezing process due to undercooling, whereas the melting of formed ice indicated a gradual process as the temperature increases in both the experimental data and the model with a continuous pore size distribution.

6.7.2 Partially Saturated Mortar Specimen

The amount of heat released during freezing (ΔH_m^F) was obtained using the numerical simulation for mortar specimens saturated at different degrees of saturation with the discrete pore size distribution model and is compared with experimental results in Figure 46. The results for these partially saturated mortar specimens are the experimental investigation of this work, whereas the experimental data of the fully saturated mortar specimen was already published (Farnam, Bentz, Hampton, & Weiss, 2014). Two heat dissipation coefficients of 40% and 60% are considered as discussed in Section 6.5. The coefficient of variation for the experimental results was obtained as 8.6%. The numerical simulation predicts greater heat release than that obtained in the experiment due to further experimental imperfections.

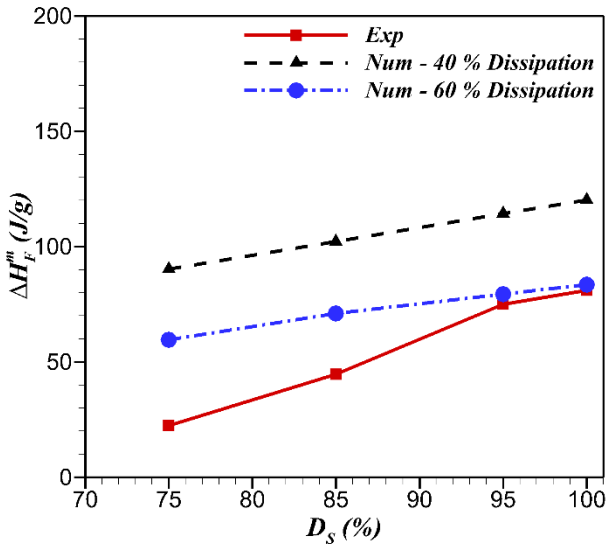

Figure 46. Amount of Heat Release During Freezing (ΔH_m^F) for the Mortar Specimen Saturated at Different Degrees of Saturations(D_S)

6.7.3 Mortar Specimens Saturated with NaCl Solution

The role of NaCl concentration in the pore solution on the thermal behavior of the mortar specimens was also investigated. The process of solidification of the brine solution absorbed in the large pores with a high degree of connectivity was investigated in this model. Therefore, the volume fraction of freezable pore solution containing NaCl solution was assumed to be 60%. Afterwards, the parameter $\xi(T)$ was employed to calculate the volume fraction of frozen pore solution $v_F(T)*\xi(T)=0.6*\xi(T)$ using the lever rule (based on the phase diagram of NaCl solution). Since it is proposed that the pores larger than gel pores are susceptible to freezing in this numerical model, the size of a salt crystal was sufficiently large so as not to increase its solubility correspondingly. As mentioned in section 6.6, undercooling compels the solutions inside the porous media to freeze at a temperature below their melting points which can result in an instantaneous solidification of a relatively large fraction of pore solution within the mortar specimen (see Table 20). It is hypothesized that after this sudden freezing, a gradual phase transformation of the water phase of the solution to ice would occur for the remaining solution in the mortar specimen saturated with NaCl solution. This was computed by using the lever rule approach to solidify the remaining unfrozen fraction of solution (excluding the eutectic solution) until the temperature of each layer reaches $T_{eut} = -21.1$ °C. For the case of mortar specimens saturated with 23.3% NaCl solution ($c\_eut = 23.3\%$), no ice is formed until the temperature decreases to T_{eut}.

At this temperature, the unfrozen eutectic solution transforms to eutectic ice gradually. Two different procedures are proposed to investigate the role of eutectic solution solidification on the macro-scale thermal response of the mortar specimen. The first method considers that the eutectic solution, the remaining unfrozen solution, can gradually form eutectic ice by releasing the eutectic latent heat as observed in the experiment shown in Figure 47(a) (Farnam, Bentz, Hampton, & Weiss, 2014). The second method was to allow the eutectic solution to migrate to

the adjacent accessible pores with smaller sizes to avoid the formation of eutectic ice in the numerical simulation. Finally, the numerical results were compared with macro-scale experimental data. The numerical and experimental results of heat flow of two mortar specimens saturated by NaCl solutions with 5% and 10% concentrations are compared in Figure 47(a). The variation of the two numerical models is calculated as 3%, which indicates that the eutectic phase transformation of the NaCl solution should be considered in the numerical modeling. Figure 47(b) shows the heat flow as a function of time obtained from the numerical simulation for the specimen saturated with NaCl solution while this figure compares the thermal behavior of a mortar specimen with and without undercooling. First, since a more gradual freezing is considered, a broader exothermic peak in the heat flow was observed for the numerical simulation without undercooling,. Second, since the freezing point T_f is assumed to be identical to the melting temperature T_m, the ice formation occurs earlier in the case of the mortar specimen without including undercooling. Third, since a lower volume fraction of pore solution freezes at the corresponding freezing point T_f, the exothermic peak becomes smaller by increasing the NaCl solution concentration, which results in a lower heat release through the mortar specimen. Fourth, due to depression of the freezing point T_f, the exothermic peak of the mortar specimens saturated with greater NaCl solution concentrations occurs later. The heat loss coefficient, h_{loss}, is assumed to be a constant value of 60% in this figure. Figure 48 displays how pore solution solidifies/melts during cooling/heating at the bottom and top layers (surfaces) of the mortar specimen since the temperature difference is the maximum between these layers. At the bottom layer, solution containing NaCl first freezes suddenly when reaching T_f due to undercooling effects. Afterwards, ice gradually forms as the temperature further decreases until the temperature reaches T_{eut} at the bottom layer of the mortar specimen. At T_{eut}, all liquid solidifies in the capillary, air-entrained, and air-entrapped pores.

As described in section 6.6, at the moment of sudden freezing (when the temperature of the bottom layer reaches T_f), the portion of the mortar specimen whose temperature is between T_f and T_m was allowed to freeze instantaneously. Since the temperature of the top layer of the mortar specimen is higher than the temperature at its bottom layer during a cooling cycle, a lesser amount of ice is produced at the top layer during the sudden freezing (i.e., undercooling) in comparison to the bottom layer, as can be seen in Figure 48. The remainder of the pore solution begins to freeze as the temperature of the layer drops. This solidification process is similar between the bottom and top layers of the mortar specimen containing 0% NaCl solution, since this process takes place immediately (0.04 seconds). During heating, the melting transformation occurs gradually and the amount of ice can be simply calculated based on the lever rule, since no undercooling occurs.

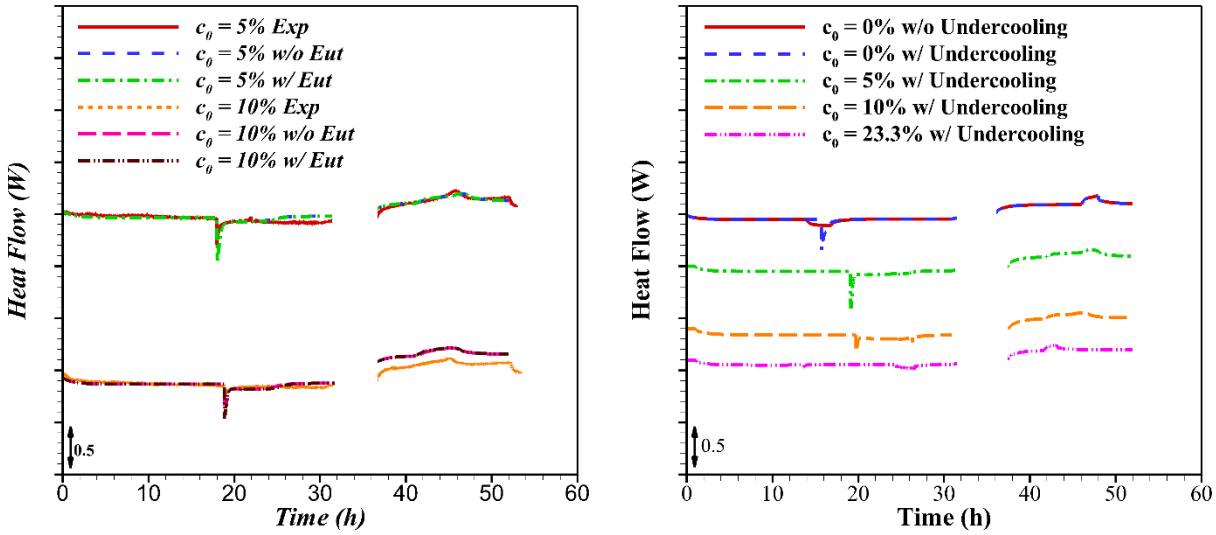

(a) (b)

Figure 47. Heat Flow as a Function of Time for Mortar Specimens Saturated with NaCl Solution Obtained from (a) Experimental Results and Numerical Simulation to Investigate the Role of Eutectic Phase Transformation and (b) Numerical Simulations at Various Concentrations (0%, 5%, 10%, 23.3%)

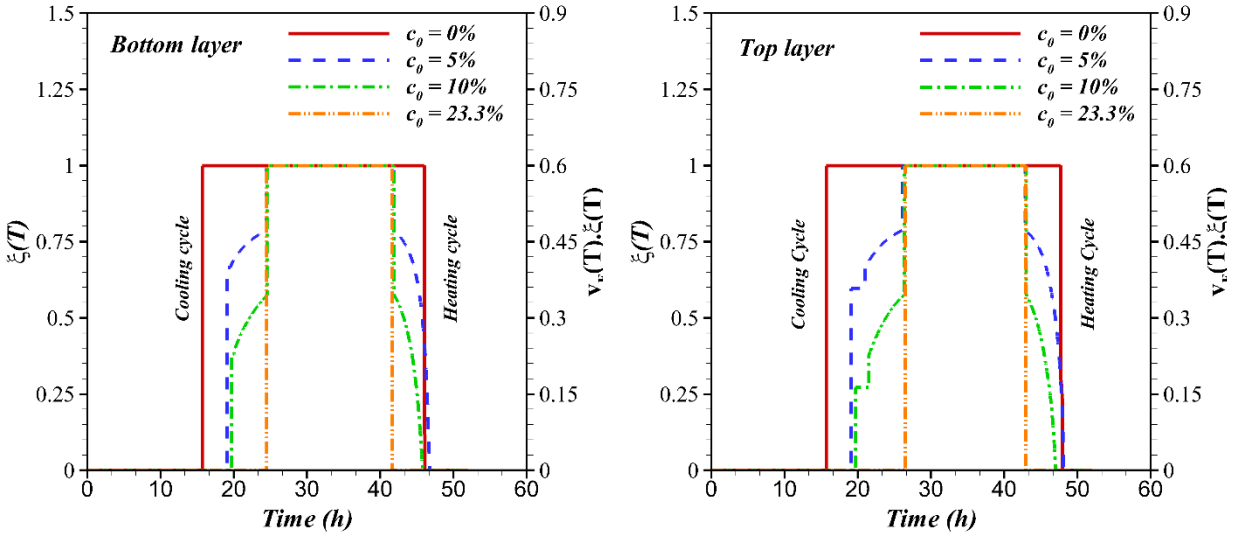

(a) (b)

Figure 48. Frozen Fraction of Pore Solution of the Mortar Specimen Saturated Using NaCl Solution as a Function of Time at (a) Bottom Layer (x = 32 mm) and (b) Top Layer (x = 83 mm)

There is, therefore, relatively no difference in the melting behavior of pore solution between the top and the bottom layers of the mortar specimen. Figure 49 shows the accumulated released/absorbed heat by the mortar specimen as a function of its bottom layer temperature (i.e.,

($x = 32$ mm)). Pore solutions containing 0%, 5%, and 10% NaCl illustrate a relatively extreme heat emission due to freezing, while the solution containing 23.3% NaCl releases relatively little energy as it is only composed of the eutectic composition (see Figure 49(a)). A snapback (rise) of temperature is observed at freezing onset due to the undercooling of pore solution. Figure 49(b) displays how the specimen absorbs heat during heating/melting. Since melting is a gradual process, the heat absorption occurs at a relatively gradual rate with respect to the freezing process. The total amount of released heat during freezing is identical to the total amount of absorbed heat during melting in the system. The heat loss coefficient, h_{loss}, is assumed to be a constant value of 60% in this figure.

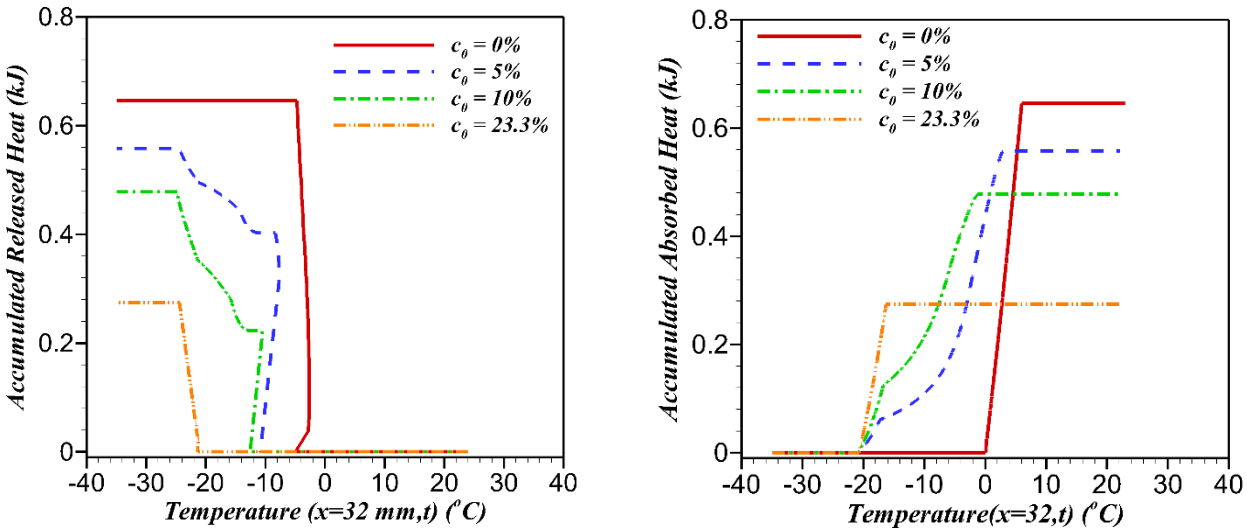

(a) (b)

Figure 49. Accumulated Heat as a Function of Temperature for Mortar Specimen with 5%, 10%, and 23.3% NaCl Concentration (a) Heat Released by the Specimen During One Freezing Cycle and (b) Heat Absorbed by the Specimen During One Thawing Cycle Versus Cold Plate Temperature

The amount of heat released during freezing (ΔH^m_F) is numerically obtained and plotted as a function of NaCl concentration and compared with experimental results in Figure 50. The coefficient of variation for the experimental results is obtained as 8.6%, based on three replicate specimens. The numerical results are calculated by considering the two coefficients of heat dissipation, h_{loss}, to compare to the experimental data.

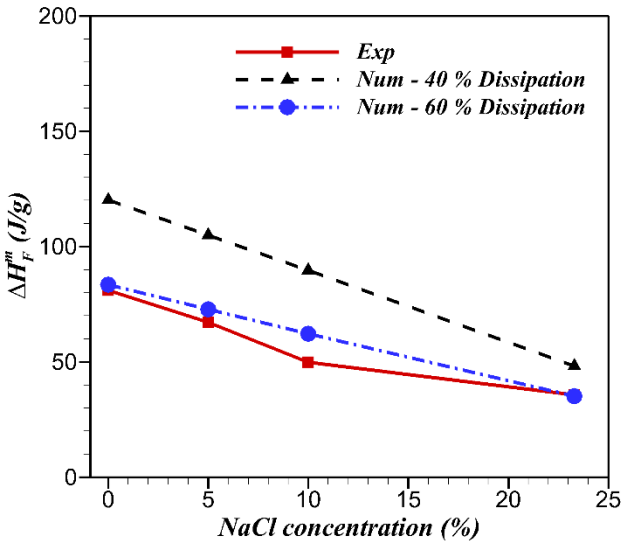

Figure 50. Amount of Heat Release During Freezing (ΔH^m_F) for the Mortar Specimen Saturated with Different NaCl Solutions

Considering these heat dissipation coefficients, the coefficient of variation between experimental result and numerical results with 40% and 60% are obtained as 36% and 9%, respectively. The numerical over-prediction of latent heat emission is caused by further experimental imperfections.

6.8 SUMMARY

A one-dimensional finite difference numerical model was used to predict the macroscopic freeze-thaw behavior of air-entrained mortar specimens. The effective thermal properties of the composite mortar were estimated using homogenization techniques. The role of curvature, owing to a broad range of pore sizes, was considered in calculating the volume fraction of freezable pore solution exposed to freezing/thawing cycles using measured absorption-desorption isotherms. It was concluded that the role of pore size (or curvature) on the macroscopic behavior of the air-entrained mortar specimen was negligible during freezing due to the quantity of larger pore sizes in realistic mixtures and undercooling, whereas the role of curvature had a considerable impact on the macroscopic behavior of the frozen mortar specimen during melting. The lever rule approach, derived from a phase diagram of the NaCl-water solution, and undercooling were adopted in the numerical model. It was concluded that this model can simulate the freezing and thawing process of mortar specimens saturated with water or various NaCl solutions to predict the thermal behavior of mortar specimens at various degrees of saturation or saturated with various concentrations of NaCl solutions.

The computational results were compared to the experimental ones obtained for mortar specimens saturated with NaCl solution using a low-temperature LGCC. A lower amount of heat release (or freezable fraction of pore solutions) was observed in the experiment than the theoretical value predicted based on the measured desorption isotherm. The difference could be mainly due to experimental conditions allowing significant heat dissipation within the LGCC

experiment. To justify the experimental underestimation of heat release, two heat loss coefficients (40% and 60%) were evaluated to validate the numerical results. Accordingly, a better agreement was exhibited between the numerical results and the experimental data.

7. NUMERICAL SIMULATION OF PCMs APPLICATION IN CONCRETE PAVEMENT

Concrete incorporating PCMs can be used in pavements to store thermal energy to aid in snow and ice removal (Hawes & Feldman,1992; Bentz & Turpin, 2007). PCMs have the ability to absorb or release the energy in heat at specific temperature when they experience phase transformation (Mondal, 2008). The heat capacity and high density of concrete pavement combined with the incorporation of the latent heat storage of PCMs can provide an ideal case for energy storage. Two potential applications of PCMs in concrete have been addressed in the works of Zhang et al. (2004) and Bentz & Turpin (2007). The porous LWA was successfully impregnated with PCM, as described in Sections 2 and 4.

This section contributes to existing knowledge based on the use of PCMs in the airport concrete pavements. For this study, the thermal behavior observed in two sets of experiments was simulated using a fundamental one-dimensional finite difference method. The thermal responses of two experiments were compared with the numerical predictions during the freeze-thaw thermal cycles to assess the validity of the model on application of PCMs in concrete. Finally, concrete pavements of four locations were simulated to evaluate the efficiency of using PCMs at the time the temperature of the pavement drops below 0 (°C). In conclusion, this study showed how incorporating PCMs can improve the potential for passive heating to melt snow and ice in airport pavements.

7.1 NUMERICAL SIMULATION

In Section 5, the authors show that PCMs can be incorporated in LWAs and incorporated into concrete to provide passive heating. The concrete that contains PCMs experience heating when the PCM undergoes a phase transformation as the temperature of specimen reduces to the melting point, T_m, of a PCM. At this temperature, the transition from liquid to solid in the PCM releases heat. The objectives of this study were to (1) quantify the fraction of PCM that can change phase (freeze/melt) at a specific temperature, and (2) estimate the amount of the released/absorbed latent heat produced by the phase transformation of PCM. The thermal response of the concrete specimen can be predicted using the general heat diffusion equation shown in Equation 17 (Incropera et al., 2006).

$$k_c(T) \cdot \left[\frac{\partial^2 T(x,t)}{\partial x^2}\right] + h_{diss} \cdot \left[\frac{\partial T(x,t)}{\partial x}\right] + q_{gen} - q_{loss} = \rho_c(T) \cdot c_c^p(T) \cdot \left[\frac{\partial T(x,t)}{\partial t}\right] \qquad (17)$$

Where:

$T(x,t)$ is the temperature in the pavement at location $x(mm)$ and time $t(\text{sec})$,
$k_c\ (T)$ is the thermal conductivity of the concrete $[W/(m \cdot {}^oK)]$ at temperature T,
$\rho_c(T)$ is the density of the concrete (kg/m^3) at temperature T,
$c^p{}_c(T)$ is its specific heat capacity $[J/(kg \cdot {}^oK)]$ at temperature T,
h_{diss} is the heat dissipation coefficient carried to the lateral direction $[W/(m^2 \cdot {}^oK)]$,

q_{gen} is the rate of generated or consumed heat from any phase change of the PCM $[J/(m^3 \cdot \text{sec})]$, and q_{loss} is the rate of heat dissipation during phase transformation in the experiment $[J/(m^3 \cdot \text{sec})]$.

A 40%–50% reduction of heat release was measured using an LGCC experiment during phase trasnformation in the previous testings (Farnam, Esmaeeli, Bentz, & Zavattiero, 2015). Equations 18a and 18b describe the latent heat term, q_{gen}, related to freezing/melting of PCM and dissipation of latent heat term, q_{loss}, related to significant heat loss between the concrete and environment.

$$q_{gen} = \rho_{PCM} \cdot v_{P-LWA} \cdot \frac{\partial[\Delta H_f]}{\partial t} \tag{17a}$$

$$q_{loss} = h_{diss-enth} \cdot \rho_{PCM} \cdot v_{P-LWA} \cdot \frac{\partial[\Delta H_f]}{\partial t} \tag{17b}$$

Where:

ΔH_f is the latent heat of fusion (kJ/kg),
$\rho_{PCM}$is the density of the PCM (kg/m^3),
v_{P-LWA} is the total volume fraction of pores within the LWAs, and
$h_{diss-enth}$ is the heat dissipation coefficient when PCM experiences the phase transformation (<1).

7.2 FREEZABLE FRACTION OF PCM

The released/absorbed heat flow of the PCM was measured (in Section 5) using the LT-DSC at a loading rate of 0.1 °C/min, shown in Figure 51(a). The exothermic/endothermic peaks representing the phase transformation are shown in the cooling and heating portions of the concrete respectively, and the results are normalized by the mass of the PCM. It is observed that the solidification of the PCM occurs at the temperature of T_f=4.09 °C and steadily progresses until the temperature drops to -8 °C, which implies a gradual process of solidification of the liquid PCM. As mentioned in Section 5, this is due to the pore size distribution of the LWA that varies the temperature of the phase change.

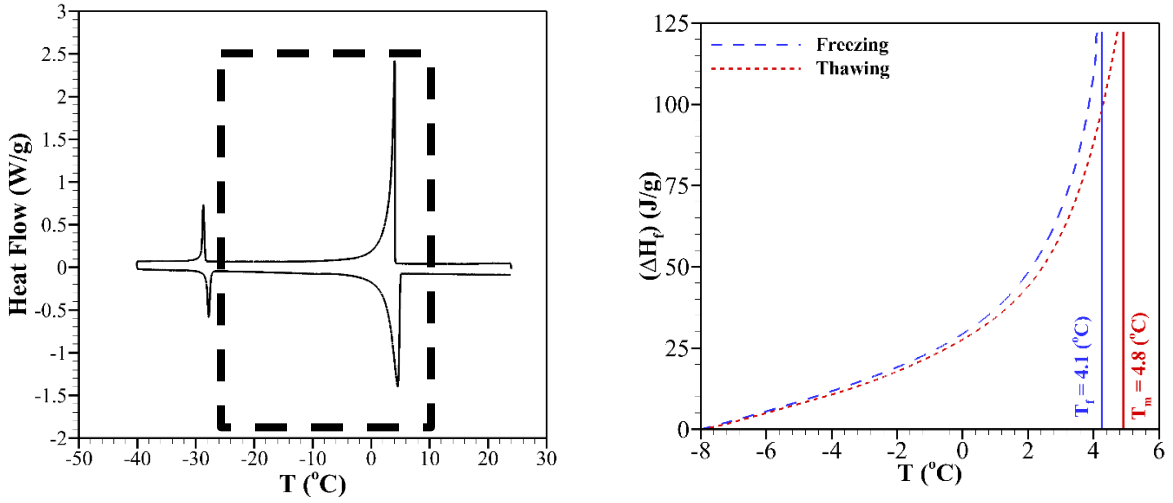

(a) (b)

Figure 51. (a) Thermal Storage Analysis of PCM (paraffin oil) Using an LT-DSC Device and (b) Rate of Released/Absorbed Enthalpy Heat of Fusion During One Freeze-Thaw Cycle

In melting, the solid PCM begins to melt at -8 °C, and this gradual process of thawing continues until the temperature increases to T_m = 4.8 °C; after this temperature, no solid PCM can exist. The heat that is released or absorbed during the phase transformation is calculated and shown in Figure 51(b). Paraffin oil shows an exothermic enthalpy fusion of ~$157.1\,J/g$ and endothermic enthalpy fusion of ~$155.1\,J/g$.

To calculate the rate of enthalpy of fusion $\frac{\partial \Delta H_f}{\partial t}$, two approaches were evaluated in this study: (1) an approach with consideration of only one characteristic temperature to occur phase transformation, and (2) an approach with explicit consideration of a broad range of temperatures at which phase transformation can occur, as shown in Figure 51(b). In the first approach, it is assumed that the solidification and melting can be simplified as occurs at two specific temperatures of T_f and T_m, correspondingly. The second approach considers that the solidification/melting processes occur at a continuous range of temperature and $\frac{\partial \Delta H_f}{\partial t}$ varies continuously as the temperature changes.

7.3 EFFECTIVE THERMAL PROPERTIES OF CONCRETE

Cementitious systems (i.e., mortar or concrete specimens) are composed of various constituents as a porous composite material. To predict a reliable thermal response of these composites, it is necessary to correctly estimate the thermal properties to be used in Equation 17. Depending on the temperature and saturation state, the concrete might be composed of dry concrete, aggregates, liquid/solid PCM impregnated in LWAs, and pore structure containing air and water. It is assumed that no ice exists in the pores since the degree of saturation of specimen is lower than 40%. Therefore, water solution in the pores is not susceptible to freezing at a temperature greater than -35 °C (Esmaeeli et al., 2016).

7.3.1 Thermal Conductivity, k_m

The EMT (Levy et al., 1997) can be used to define properties of a composite material for a heterogeneous mixture. The thermal conductivity of the concrete, k_c, was estimated using the EMT formulation, as described in Equation 19.

$$k_c = k_{dry} \cdot \frac{2(1-\nu_P-\nu_{P-LWA})\cdot k_{dry}+(1+2(\nu_P+\nu_{P-LWA}))\cdot k_P}{(2+\nu_P+\nu_{P-LWA})\cdot k_{dry}+(1-\nu_p-\nu_{P-LWA})\cdot k_P} \quad (19)$$

Where:

k_{dry} is the thermal conductivity of the dry concrete specimen,
$k_p$is the thermal conductivity of the material in the pores,
v_p is the total volume fraction of pores in the cement paste matrix, and
$v_{P-LWA}$is the volume fraction of pores in LWAs.

A parallel model (Progelhof et al., 1976) was employed to determine the effective k_p as a function of the volume fractions of each component (i.e., k_{air}, k_{water}, and k_{sol}n), as described in Equation 20.

$$k_P = k_{air} \cdot v_{air} + k_{water} \cdot (v_P - v_{air}) + k_{solid} \cdot \xi(T) \cdot v_{P-LWA} + k_{liquid} \cdot [1 - \xi(T)] \cdot v_{P-LWA} \quad (20)$$

Where:
k_{air} is the thermal conductivity of air,
$v_{air} = (1 - D_S) \cdot v_P$ is the volume fraction of air in the concrete pores,
k_{water} is the thermal conductivity of water solution in the pores,
v_p is the total volume fraction of pores in the matrix,
k_{solid} is the thermal conductivity of solid paraffin, and
k_{liquid} is the thermal conductivity of the remnant liquid paraffin within the LWA pores.

The corresponding thermal conductivities of air, water, solid/liquid paraffin, and dry concrete are also provided in Table 21.

Table 21. Additional Properties of Thermally Conductive Pad, Foam, and Pyroceram Code 9606

Material	*k (W/(m·K))*	ρ *(kg/m^3)*	*c^p (kJ/(kg·K))*
Dry concrete	1.78 ±0.3	2162 ±150	950 ±100
Water	0.52 ±0.018	998 ±5	4183 ±5
Liquid paraffin	3.1 ±0.7	766 ±140	2981 ±190
Solid paraffin	3.2 ±0.7	865 ±148	2604 ±248
Thermal Pad	3.0	309	850
Foam	0.03	20	1340
Pyroceram Code 9606	*	2600	900

7.3.2 Density, ρ

The law of mixtures (a weighted mean) can be used to predict the density of a composite material as described in Equation 21.

$$\rho_c = \rho_{dry} \cdot (1 - v_P - v_{P-LWA}) + \rho_P \cdot (v_P + v_{P-LWA}) \tag{21}$$

Where:
ρ_{dry} is the density of the dry concrete and
ρ_P is the effective density of the materials in the concrete and LWA pores (i.e., air, liquid paraffin, and solid paraffin).

The law of mixtures was again employed to obtain the effective density of materials in concrete and LWA pores (i.e.,ρ_P) as described in Equation 22.

$$\boldsymbol{\rho_P = \rho_{air} \cdot v_{air} + \rho_{water} \cdot (v_P - v_{air}) + \rho_{solid} \cdot \xi(T) \cdot v_{P-LWA}} \\ \boldsymbol{+\rho_{liquid} \cdot \big(1 - \xi(T)\big) \cdot v_{P-LWA}} \tag{22}$$

Where ρ_{air}, ρ_{water}, ρ_{solid}, and ρ_{liquid} are the densities of air, water solution, solid paraffin, and liquid paraffin, respectively. The corresponding densities of air, water solution, solid paraffin, liquid paraffin, and dry concrete are also provided in Table 21.

7.3.3 Specific Heat Capacity, c_m^p

The process of determining an effective specific heat capacity is conceptually similar to determining an effective density using Equation 23.

$$c_c^p \cdot \rho_c = c_{dry}^p \cdot \rho_{dry} \cdot (1 - v_P - v_{P-LWA}) + c_P^p \cdot \rho_P \cdot (v_P + v_{P-LWA}) \tag{23}$$

Where: c_{dry}^p is the specific heat capacity of the dry concrete and c_P^p is the effective specific heat capacity of materials in the concrete and LWA pores (i.e., air, water solution, liquid paraffin, and solid paraffin) which can be calculated using Equation 23.

$$C_P^p \cdot \rho_P \cdot v_P = C_{air}^p \cdot \rho_{air} \cdot v_{air} + C_{water}^p \cdot \rho_{water} \cdot (v_P - v_{air}) + \\ \left[C_{solid}^p \cdot \rho_{solid} \cdot \xi(T) \cdot v_{P-LWA} + C_{liquid}^p \cdot \rho_{liquid} \cdot \big(1 - \xi(T)\big) \cdot v_{P-LWA}\right] \tag{23}$$

Where: c_{air}^p, c_{water}^p, c_{solid}^p, and c_{liquid}^p are the specific heat capacities for air, water solution, liquid paraffin, and solid paraffin, respectively. The corresponding specific heat capacities of air, water solution, liquid paraffin, solid paraffin, and dry concrete are provided in Table 21.

7.4 CONFIGURATION OF NUMERICAL SIMULATION IN THE LGCC EXPERIMENT

The LGCC experiment was numerically simulated to determine the thermal response of concrete specimen containing PCM. A one-dimensional heat transfer is provided to minimize the heat

dissipation throughout the experiment by installing a heat sink at the bottom, foam (thermal insulator) and longitudinal insulation on the sides, and foam at the top of the experimental system (see Figure 52(a)). However, two different types of heat dissipation are observed: (1) convection of heat energy in lateral direction due to temperature difference of concrete specimen and ambient, and (2) a difference between the measured released heat in an LGCC experiment and the associated enthalpy of fusion of PCM due to experimental imperfections (e.g., thermal bridges, heat leaks). Two heat loss coefficients of h_{diss} and $h_{diss\text{-}enth}$ are employed to simulate the energy dissipation in the experimental system, which are estimated as 0.7 ($W/m^2.^oK$) and 40%–60% heat losses.

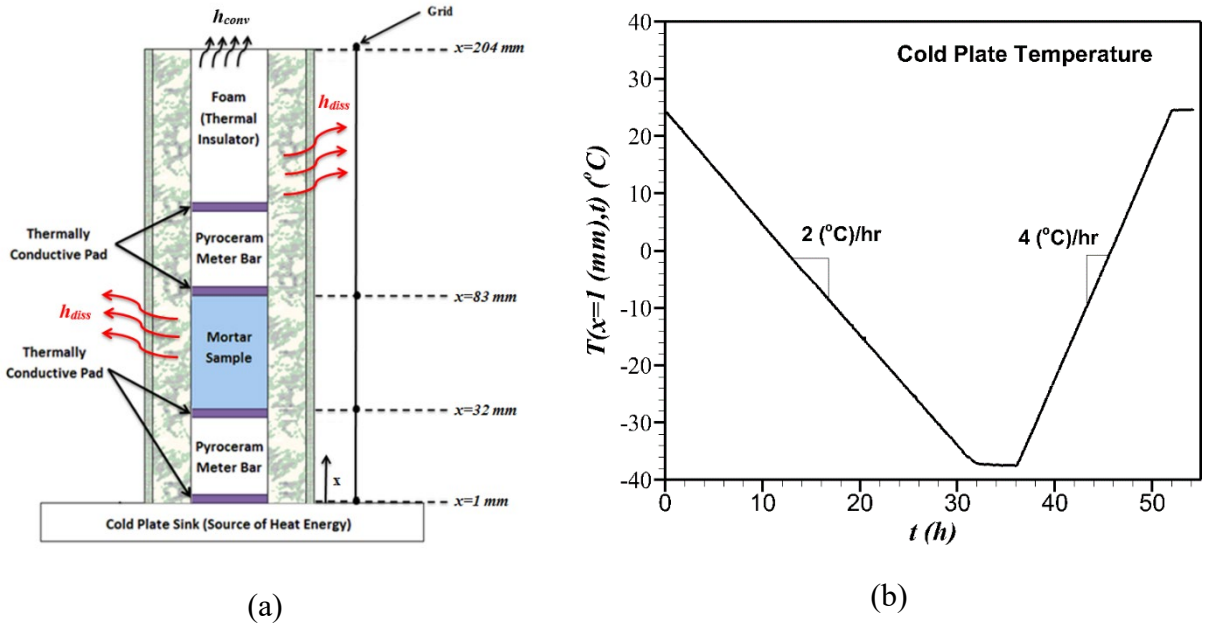

Figure 52. (a) Configuration of LGCC Experimental Apparatus and Imposed Boundary Conditions with Adapted Finite Difference Grids and (b) Temperature Profile at the Bottom of Experiment, T (x=1, t)

An appropriate grid size, Δx of 1 (mm), and time step size, Δt of 0.05 (sec), are used to discretize the spatial and temporal domain of the experiment. A finite difference method was used. The initial temperature of the experimental setup is set as ambient temperature $T\ (x,\ t=0)$ = 24 (°C) and variable temperature history at the bottom of the LGCC experiment, $T\ (x = 1\ mm,\ t)$, shown in Figure 52(b). A heat convection coefficient, h_{conv} = 100 W/(m^2·K), is employed to account the heat energy transfer between the air and the foam on the top.

7.4.1 Sensitivity Analysis

The numerical study investigates the validity and sensitivity of the model to thermal properties of constituents of concrete as a composite. Five variables are important in this study and can significantly alter the thermal response in an LGCC experiment:

(1) the heat dissipation coefficient (h_{diss});

(2) thermal conductivity of the specimen (k_c), liquid PCM (k_{PL}), and solid PCM (k_{PS});
(3) density of the specimen (ρ_c), liquid PCM (ρ_{PL}), and solid PCM (ρ_{PS});
(4) specific heat capacity of the specimen ($c^P{}_c$), liquid PCM ($c^P{}_{PL}$), and solid PCM ($c^P{}_{PS}$); and
(5) the amount of latent heat release/absorption ΔH_f.

The variation of those five thermal properties can alter the thermal response of concrete, as shown in Equation 4. Three effective parameters of k_c, ρ_c, and $c^P{}_c$ determine the rate of heat diffusion through the specimen, whereas two properties of h_{diss} and ΔH_f control the rate of heat energy exchange with environment and rate of heat energy generation during phase transformation of PCM, respectively. Therefore, the sensitivity of numerical results to the variation of these parameters is investigated and the optimum parameters are employed to be compared with experimental data in the following subsections.

7.4.2 Dissipation Coefficient, h_{diss}

The influence of h_{diss} can control the rate of heat energy exchange between the experimental system and the environment. In the analysis of h_{diss}, the concrete specimen is considered to contain no PCM to assess the influence of the variation of heat dissipation parameter on the thermal response. Figure 53(a) and (b) show the variation in the heat flow and the temperature profile of a concrete specimen in an LGCC experiment exposed to four different h_{diss}, correspondingly. Figure 53(a) illustrates more inclined heat flow contour as the heat energy dissipation increases due to heat transfer rise between the experimental setup and the environment. Figure 53(b) indicates that the difference between the temperatures of the bottom surface of specimen and ambient can be reduced as the h_{diss} is augmented.

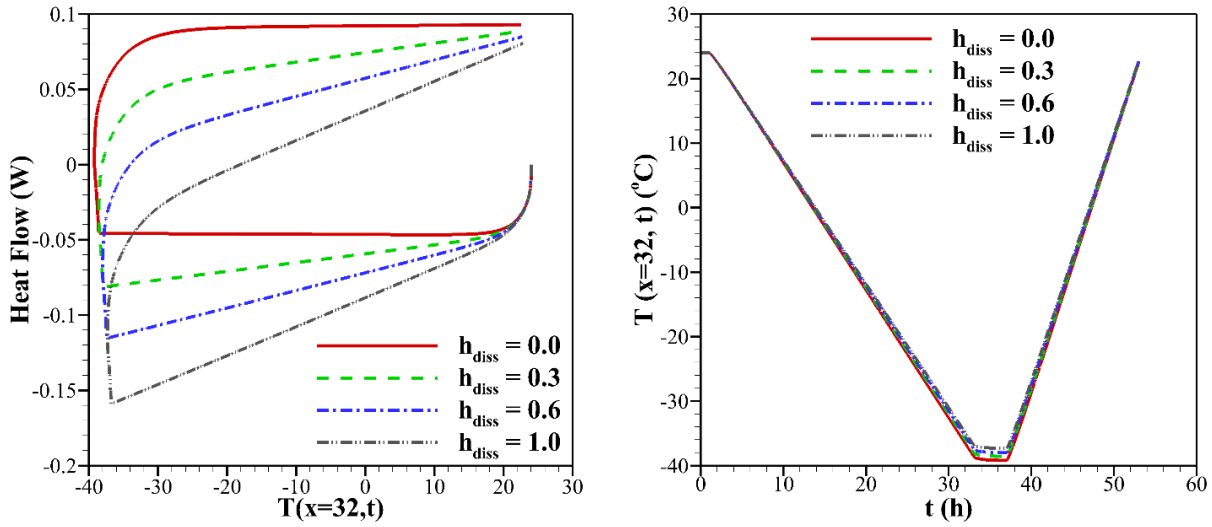

(a) (b)

Figure 53. Thermal Behavior Assessment of Concrete Specimens Exposed to Various h_{diss} in Terms of (a) Heat Flow Profile and (b) Temperature Profile

7.4.3 Thermal Properties of Concrete, k_c, ρ_c, and c_c^p

Three thermal properties of dry concrete were examined to assess how they influence the effective thermal response (i.e., heat flow) shown in Figure 54. The thermal properties were chosen based on the recommended values in Table 21. Figure 54(a) shows that the increase of thermal conductivity of the dry specimen can cause an increase in the heat flow of the specimen due to Fourier's law of heat transfer. The increase in the density and specific heat capacity of the dry specimen can result in an increase in the amount of heat energy that is required to change the temperature of the specimen, thereby reducing the amount of heat flow shown in Figure 54(b) and (c).

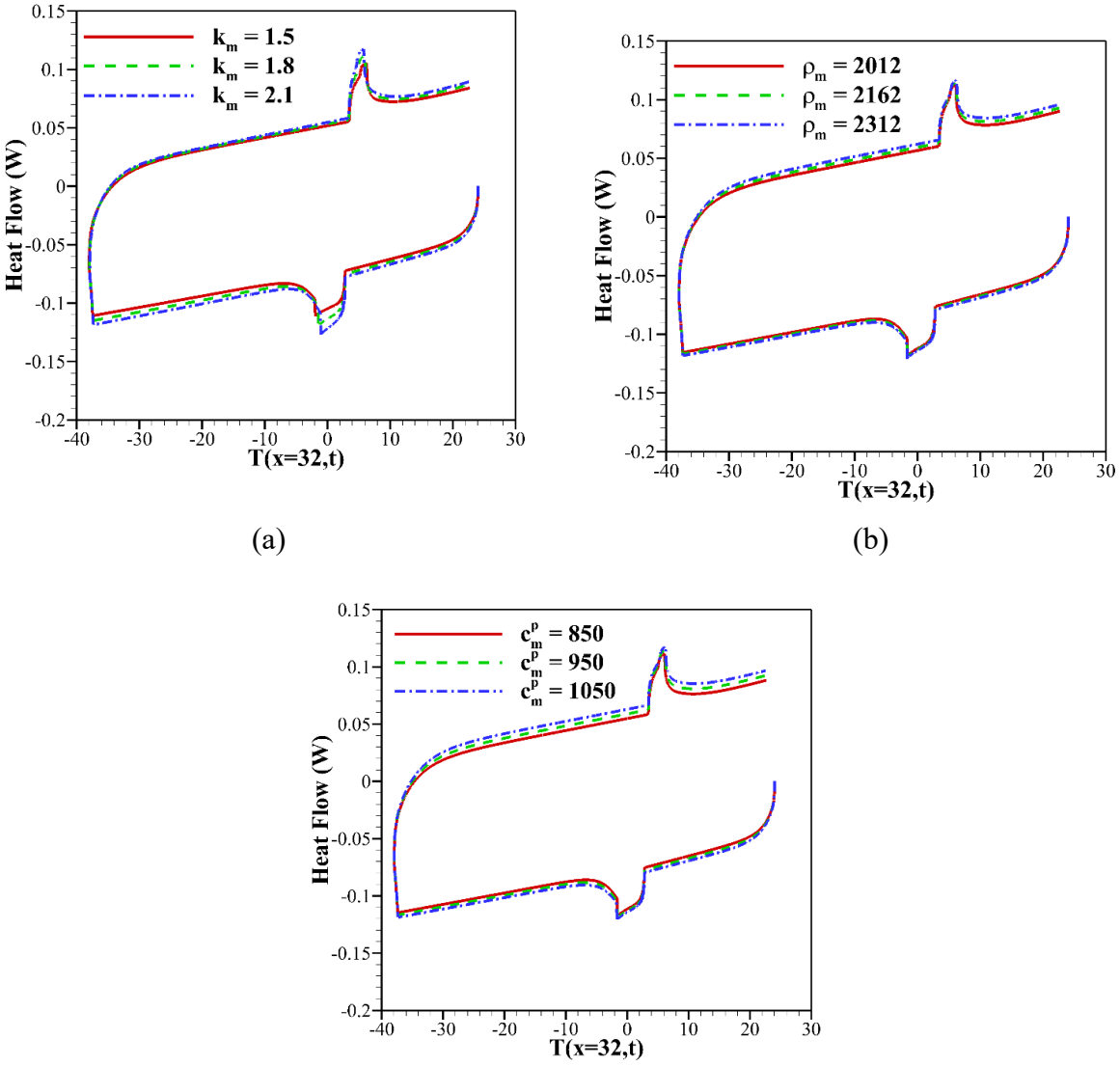

(a) (b)

(c)

Figure 54. Thermal Behavior Assessment of Concrete Specimens with (a) Various Thermal Conductivity k_m, (b) Various Density ρ_m, and (c) Various Specific Heat Capacity $c^p{}_m$

7.4.3.1 Thermal Properties of Paraffin, k_{LP},k_{SP}, and ΔH_f

The numerical analysis determines that only three thermal properties of PCM, k_{LP},k_{SP}, and ΔH_f, can substantially vary the effective thermal response, and the role of ρ_{LP}, ρ_{SP}, c_{LP}^{P}, c_{SP}^{P} can be neglected. The effect of thermal properties of PCM, k_{LP}, k_{SP}, and ΔH_f, are displayed in Figure 55. Figure 55(a) shows that the increase of thermal conductivity of liquid paraffin can cause an increase in the heat flow of the specimen due to Fourier's law of heat transfer. It is also observed that this thermal property can only influence the thermal response before the initiation of freezing of PCM and after the melting of the entire PCM. Figure 55(b) shows the increase of thermal conductivity of solid paraffin can cause an increase in the heat flow of the specimen at the initial moment of freezing of PCM and before the melting of the entire PCM. The heat generation term, ΔH_f, can alter the thermal behavior of a specimen during phase transformation of PCM by controlling the rate of latent heat release/absorption shown in Figure 55(c).

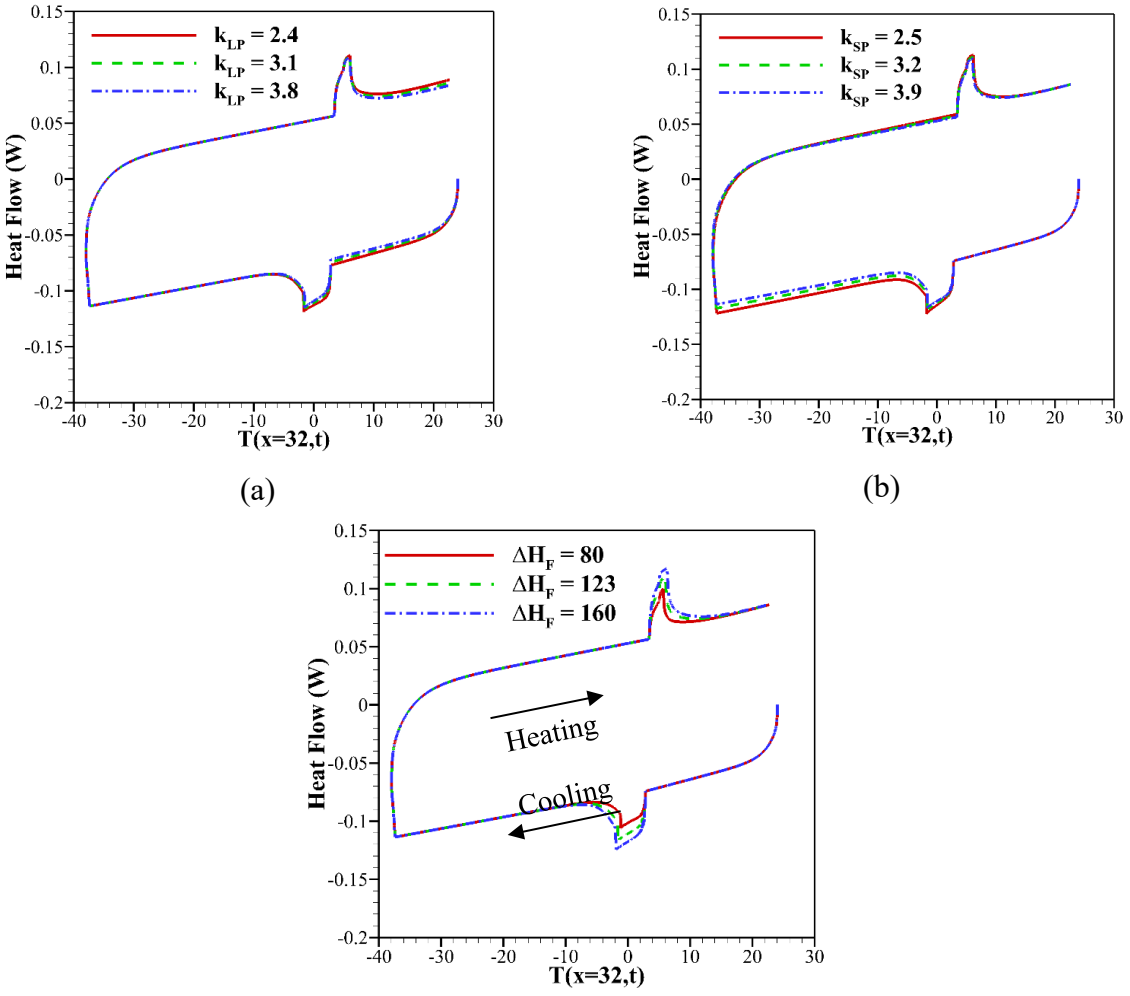

Figure 55. Thermal Behavior Assessment of Concrete Specimens with (a) Various Thermal Conductivity of Liquid Paraffin k_{LP}, (b) Various Thermal Conductivity of Solid Paraffin k_{SP}, and (c) Various Latent Heat of Fusion of Paraffin ΔH_F

7.4.4 Numerical Results for LGCC

Two numerical models, with either an instantaneous or gradual phase transformation of the PCM, were assessed during this study. The experimental and numerical results for the thermal behavior of the concrete specimen containing paraffin oil as PCM are shown in Figure 56. The coefficient of the heat dissipation to the environment, h_{diss}, and the coefficient of heat dissipation during the phase transformation action, $h_{diss\text{-}enth}$, were assumed to be constant values of 0.7 ($W/m^2.^oK$) and 40%–60%, correspondingly. Thermal properties of the constituents of the concrete specimen are shown in Table 22. Figure 56(a) and (b) indicate both the numerical and experimental temperature profiles for the saturated concrete specimen at the top and bottom layers in the LGCC experiment setup (i.e., x = 83 mm and x = 32 mm), respectively.

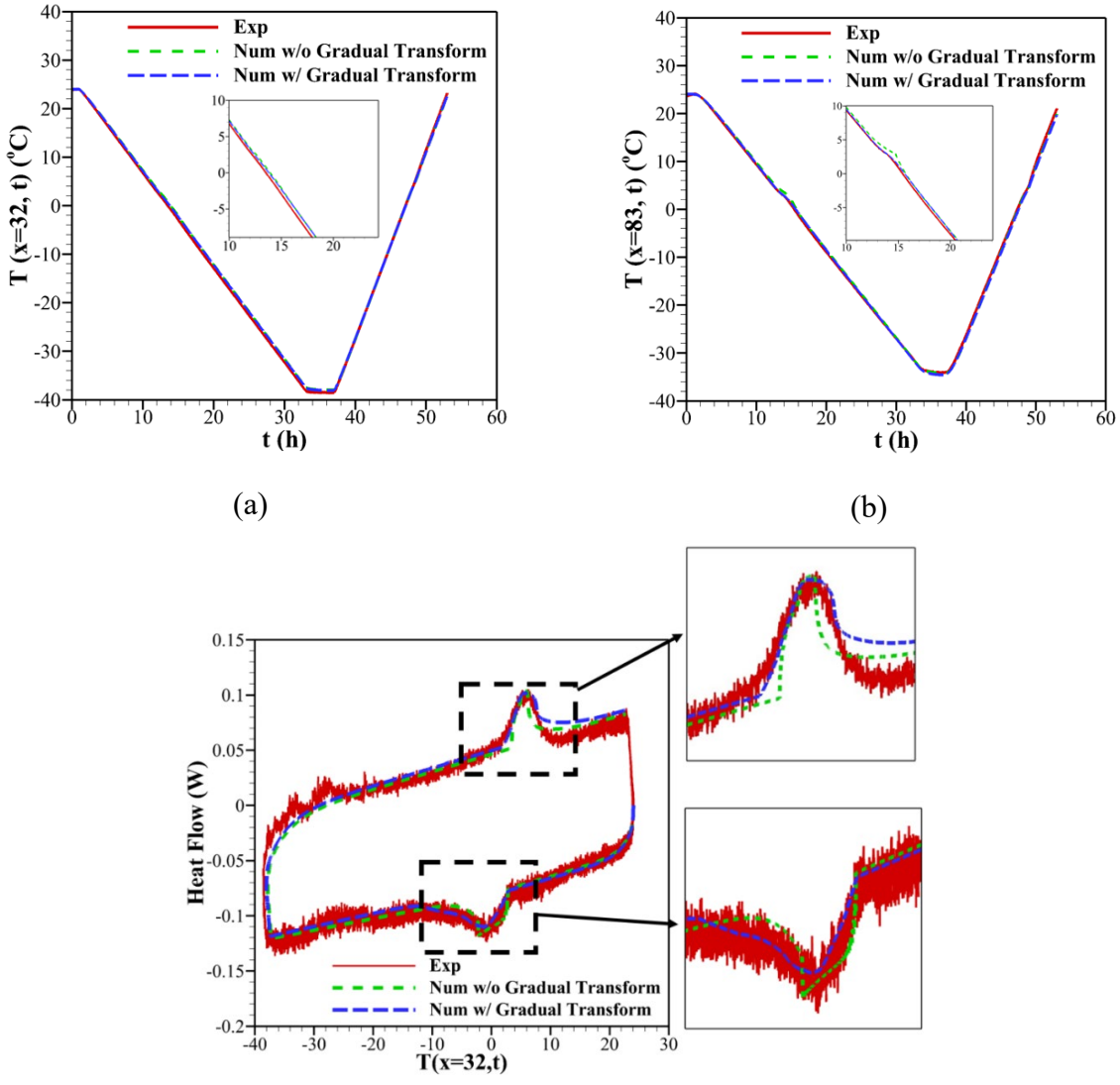

Figure 56. Experimental and Numerical Results of Concrete Specimen Containing Paraffin Oil in Terms of (a) Temperature Profile at the Bottom Surface T (x=32, t), (b) Temperature Profile at the Top Surface T(x=83, t), and (c) Heat Flow

Table 22. Thermal Properties of Constituents of Concrete Specimen

Material	k (W/(m·K))	ρ (kg/m^3)	C^p (kJ/(kg·K))
Dry concrete	1.78	2,100	900
Water	0.52	998	4,183
Liquid paraffin	3.1	800	2,820
Solid paraffin	3.9	865	2,604

Although an insignificant variation of temperature profile was observed for two models at the bottom surface (i.e., x = 32 mm), a nearly instantaneous temperature rise that occurred at the moment of freezing could be observed for the model with the assumption of instantaneous phase transformation. In contrast, a more gradual temperature change could be observed for the model with consideration of gradual phase transformation.

Figure 56(c) shows the heat flow obtained using the numerical simulation to evaluate the role of latent heat rate and compared to the experimental data. The formation of solid paraffin in the LWAs results in an exothermic peak, which is representative of the latent heat release during a cooling cycle. In the first approach, the exothermic peak is considered to occur at T_f and subsequently ceases when the entire amount of latent heat has been emitted to the surroundings. The endothermic peak begins as a gradual process at T_m, until the entire formed solid PCM melts inside the frozen pores. Conversely, the exothermic peak is extended to the end of the cooling cycle (-8 °C) due to a gradual process of phase transformation inside the LWAs in the latter model. For the case of melting, the endothermic peak is considered to occur gradually as a function of temperature.

Therefore, the melting curve extends progressively to T_m, due to the gradual rate of heat of fusion shown in Figure 56(b). In conclusion, a gradual phase transformation of PCM can reasonably be considered during the freezing and melting processes, which show an improvement on the simulation of heat flow response of the concrete specimen shown in Figure 56(c).

7.5 CONFIGURATION OF NUMERICAL SIMULATION IN LARGE-SCALE SLAB EXPERIMENT

To assess the validity of the numerical model for the concrete specimens, the temperature profile was simulated at various depths and compared with the experimental data. Two types of experimental data were used: (1) reference concrete specimens without PCM, and (2) concrete specimens with LWA that has been impregnated with PCM (paraffin).

The experiment consisted of a one-dimensional heat transfer problem. The large-scale slab was exposed to an ambient temperature at the top of the sample, and the foam and wood materials on the sides provided thermal insulation to minimize horizontal heat dissipation (Figure 57(a)). Eight thermocouples were located to track the temperature profile along the depth of slab (group of “M” in green). The experimental result also denotes a relatively small difference between the temperature of computational nodes of the concrete on the side (group of “S” in blue) and the computational nodes located between foam and wood (group of “O” in orange). This negligible reduction in the temperature occurs due to the extremely low thermal conductivity of foam. Since the heat dissipation coefficient was small, h_{diss} can be neglected. Similar to the LGCC

experiment, a heat dissipation coefficient during phase transformation, $h_{diss\text{-}enth}$, was employed to simulate the energy dissipation in the experimental system, which is estimated at about 50% heat loss.

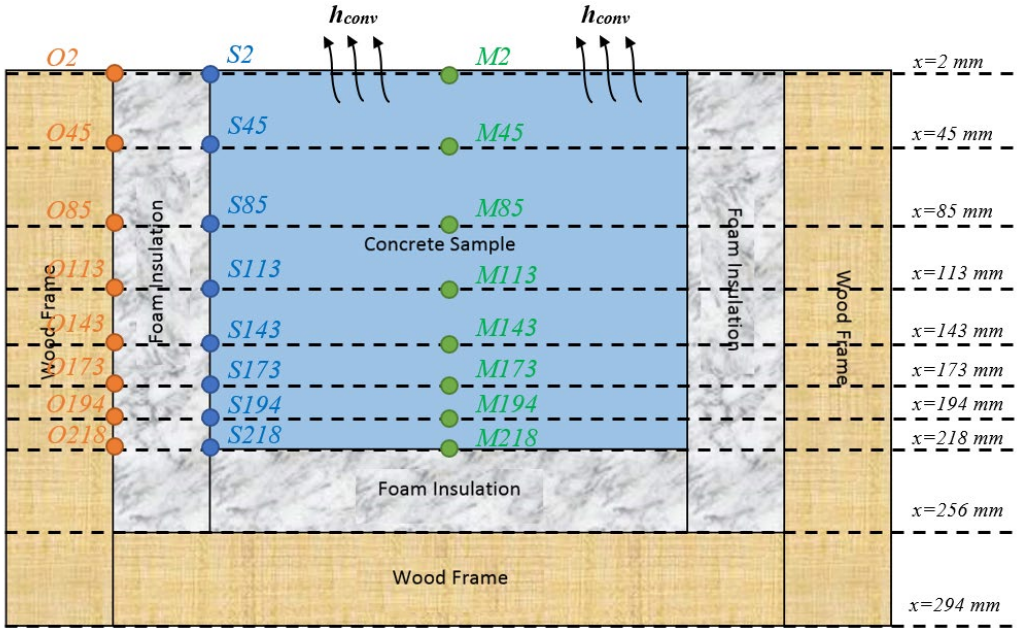

(a)

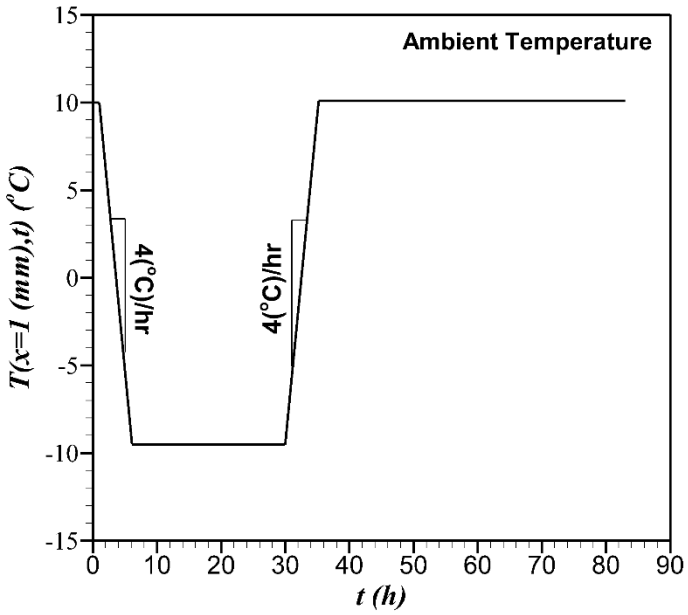

(b)

Figure 57. (a) Large-Scale Concrete Slab Experiment and Imposed Boundary Conditions with Adapted Finite Difference Grids and (b) Temperature Profile of Ambient at the Top of Experiment, T (x=1, t)

The first step in the numerical approach is to discretize the experimental setup by a finite difference method using an appropriate grid spacing size, Δx of 1 (mm) and time step, Δt of 0.05 (sec). The initial temperature of the entire experimental setup was set equal to the ambient temperature $T(x, t = 0) = 10$ (°C) as displayed in Figure 57(b). One cooling and heating thermal cycle is applied at the top of the concrete slab, $T(x = 1 \text{ mm}, t)$ (see Figure 57(a)). A heat convection coefficient, $h_{conv} = 20 \pm 3$ W/(m^2·K), was measured using the amount of heat transfer between the air and the top surface of the specimen for this chamber.

7.5.1 Numerical Results for Reference Concrete Slab without PCM

This section examines the thermal response of the reference concrete slab with no LWA that was impregnated with PCM. Figure 58 shows the experimental and numerical results for the temperature contour of concrete slabs that were exposed to one cycle of heating and cooling. The thermal properties of concrete slabs were assumed to be equal to thermal properties of the concrete specimen in the LGCC experiment (see Table 22).

Figure 58(a) shows the temperature contour of the concrete slab along the depth (i.e., 0 mm and 216 mm value; the y-axis denotes the bottom and top surfaces of slab) throughout the experiment. The temperature range was set between -10 °C and +10 °C. The contour range was set between -10 °C and +10 °C. Figure 58(b) shows the absolute temperature variation between experimental and numerical results. The range of temperature was set between 0 °C and +2 °C to increase the resolution of the temperature difference. The maximum temperature variation between experimental and numerical results is displayed in Table 23.

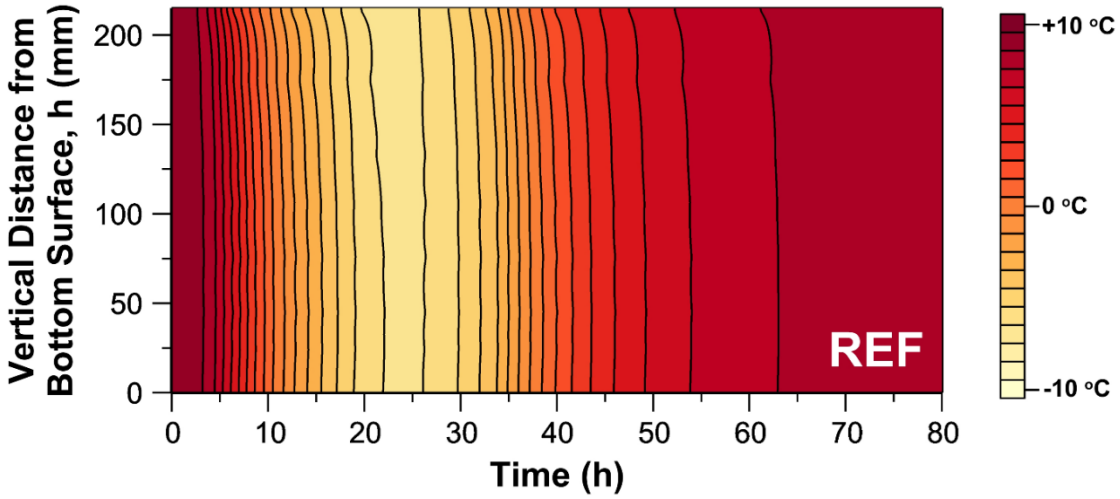

(a)

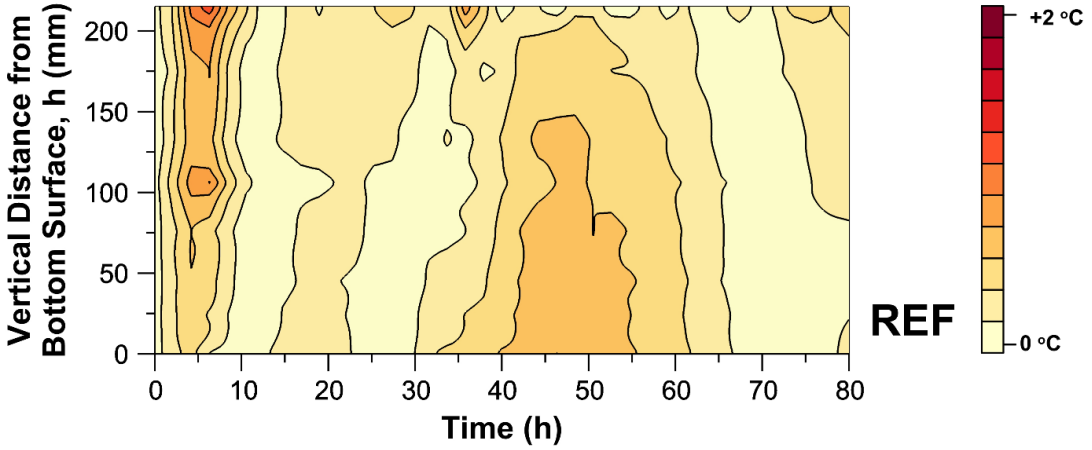

(b)

Figure 58. (a) Numerical Results of the Temperature Contour in Concrete Specimen with no PCM (paraffin) and (b) Absolute Difference in the Temperature of Experimental and Numerical Results for Concrete Specimen with no PCM (paraffin)

Table 23. Maximum Temperature Variation of Concrete Slab with No Impregnated PCM (as shown in Figure 58)

Material	*2mm*	*45mm*	*85mm*	*113mm*	*143mm*	*173mm*	*194mm*	*216mm*
Maximum temperature (°C)	1.275	0.900	0.797	1.168	0.858	0.813	0.794	0.845

7.5.2 Numerical Results for Large-scale Concrete Slab with PCM

The role of PCM in the LWA on the thermal behavior of the concrete slab is also investigated. The process of solidification/melting of the paraffin (PCM) absorbed into the LWAs is considered. The phase transformation of PCM is observed to occur between the temperatures of 4 °C to 5.04 °C. Figure 59 shows the experimental and numerical results for the temperature contour of concrete slabs containing paraffin in LWAs that were exposed to one freeze-thaw thermal cycle. The thermal properties of paraffin are shown in Table 22. Figure 59(a) indicates the temperature contour of concrete slab along the depth (i.e., 0 mm and 216 mm value; the y-axis denotes the bottom and top surfaces of slab) throughout the experiment. The temperature range was set between -10 °C and +10 °C. The contour range was set between -10 °C and +10 °C. Figure 59(b) shows the contour to absolute temperature variation between experimental data and numerical results. The temperature range was set between -2 °C and +2 °C as shown in Figure 59(b) to increase the resolution of the temperature difference. The maximum temperature variation between experimental and numerical results is displayed in Table 24.

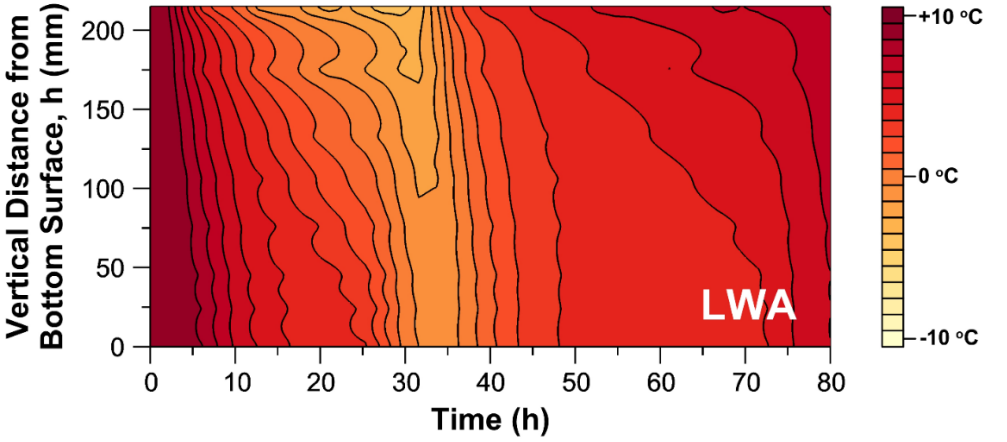

(a)

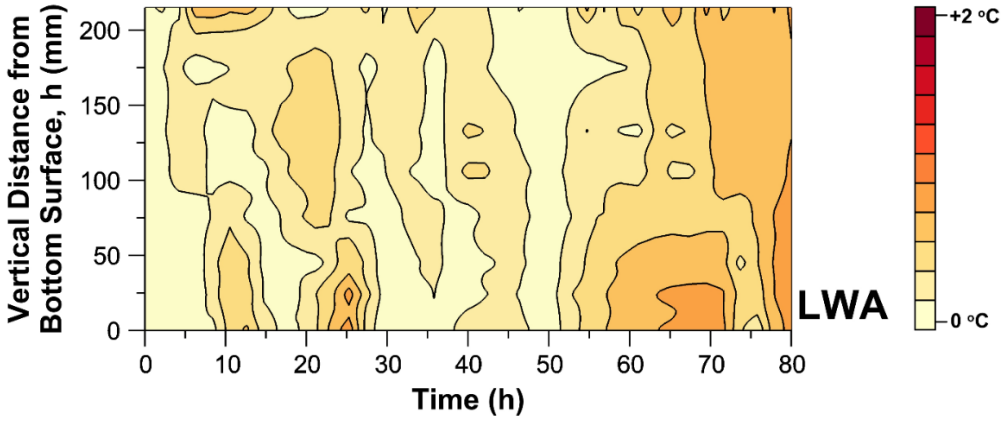

(b)

Figure 59. (a) Numerical Results of the Temperature Contour in Concrete Specimen Containing PCM (paraffin) and (b) Difference of Experimental Data and Numerical Results for Concrete Specimen Containing PCM (paraffin)

Table 24. Maximum Temperature Variation of Concrete Slab with Impregnated PCM (as shown in Figure 59)

Depths	*2mm*	*45mm*	*85mm*	*113mm*	*143mm*	*173mm*	*194mm*	*216mm*
Maximum temperature (°C)	1.289	0.933	0.932	1.001	1.064	1.081	1.108	1.176

Figure 60 shows the role of PCM on the temperature contour within concrete slabs exposed to one cycle of cooling and heating (see Figure 57(b)). The solution inside the pores begins to freeze at a temperature below -5 ^{o}C, at which the concrete is susceptible to damage produced by freeze-thaw action (Esmaeeli et al., 2016). In this study, it was assumed that freezing of solution happens at a temperature below 0 °C, visualized using white contour and where the temperature of concrete above 0 °C is visualized using color contour. Figure 60(a) displays the temperature profile of the concrete slab without the PCM (reference specimen), which is more likely to undergo ice formation inside the pores, thereby causing damage to the concrete specimen. However, a significant reduction in time of existence of formed ice in the pores is predicted in the concrete slab with the PCM as displayed in Figure 60(b). At the top surface (x = 1 mm), the time at which formed ice existed was predicted to be about 25.7 and 22.1 hours in the concrete pavements without and with the PCM, respectively. As a result, the time period at which the ice existed at the top surface of the pavement is reduced by about 3.6 hours. At the bottom surface (x = 216 mm), the time at which formed ice existed was predicted to be about 25.5 and 4.5 hours in the concrete pavements without and with the PCM, respectively. As a result, the time period at which the ice existed at the bottom surface of pavement was considerably reduced by about 21 hours, which implies that concrete pavements containing the PCM are less susceptible to ice formation and deterioration.

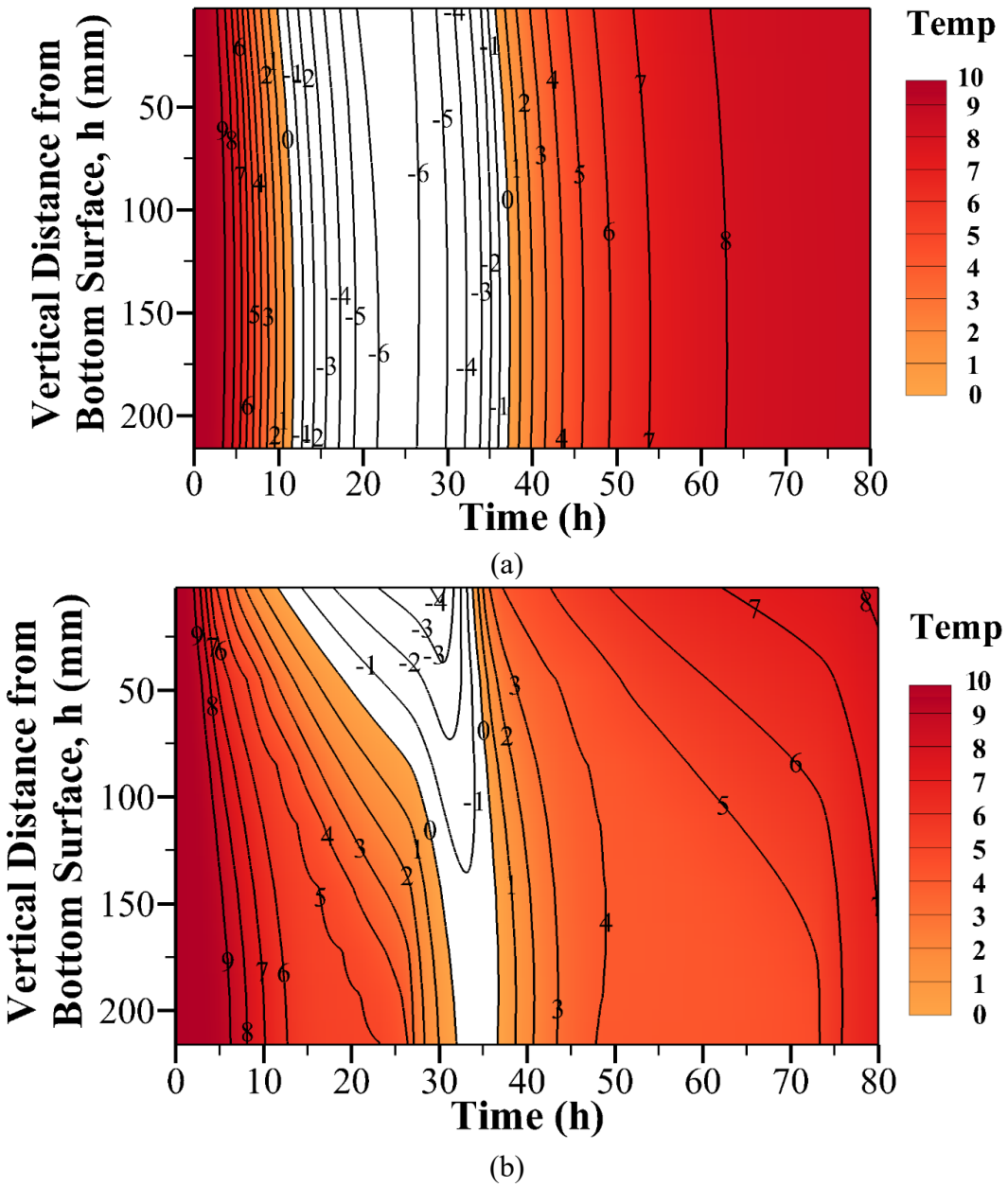

Figure 60. Numerical Results of the Temperature Contour (white color represents the temperature below 0 °C) in Concrete Specimens (a) Without LWA Containing the PCM (reference slab) and (b) With LWA Containing the PCM

7.6 PREDICTION OF THERMAL PERFORMANCE REAL-SCALE CONCRETE CONTAINING PCM

This section discusses the role of the PCM on the concrete pavement temperature during cold seasons in different international airports. Minneapolis-St. Paul International Airport (very cold weather condition), Indianapolis International Airport (cold weather condition), Atlantic City International Airport (moderate weather condition), and Portland International Airport (fairly warm weather condition) were selected for this study.

The thermal boundary conditions of real-scale concrete pavement were similar to those used in the large-scale slab experiment. The temperature histories of the four airports between the dates of October 15, 2015, to April 15, 2016, were used as the thermal boundary conditions at the top of pavement in this simulation (Farnam, Krafcik, Liston et al., 2016). A heat convection coefficient, h_{conv} = 100 W/(m^2·°K), was employed to simulate the heat transfer between the air and the top surface of the pavement (Incropera et al., 2007).

7.6.1 Minneapolis-St. Paul International Airport

Minneapolis-St. Paul International Airport is located in a zone with a very severe cold weather history. The average temperature history obtained shows that the concrete pavements are exposed to the water freezing condition (temperature below 0 °C) for 72 days annually in this location. The initial temperature of the entire experimental setup was set to the initial ambient temperature as displayed in Figure 61(a).

Ambient temperature history serves as heat sink term at the top side of concrete pavement. The one-dimensional finite difference method was employed to predict the temperature of concrete pavement at three different depths (i.e., 1 mm, 25 mm (1 inch), and 50 mm (2 inches)). The red line denotes the events when the pavement temperature reached 0 °C, thereby creating the water freezing condition. The phase transformation of the PCM begins at the temperature range of 4 °C and 5.04 °C. Therefore, the heat release/absorption results in maintaining the pavement temperature above 0 °C for a relatively longer time (see Figure 61).

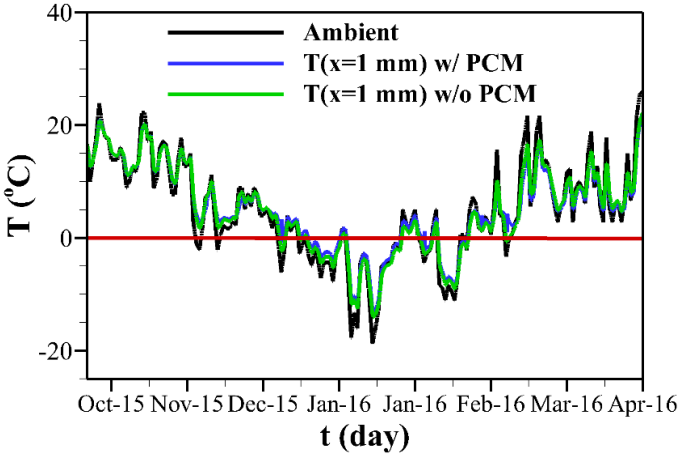

(a)

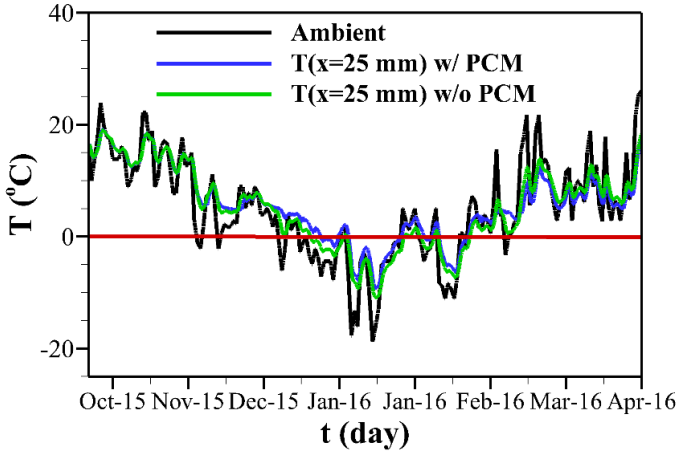

(b)

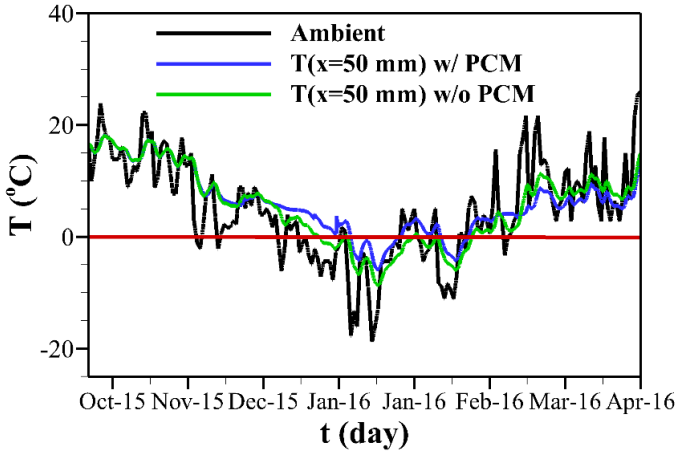

(c)

Figure 61. Temperature Prediction of PCM in Minneapolis-St. Paul International Airport at Depths of (a) 1mm, (b) 25mm, and (c) 50mm

7.6.2 Indianapolis International Airport

Indianapolis International Airport is located in a zone with a cold weather history. The average temperature history obtained shows that the concrete pavements are exposed to the water freezing condition (temperature below 0 °C) for 34 days in this location. The initial temperature of the entire experimental setup was set to the ambient temperature as displayed in Figure 62(a). Ambient temperature history serves as heat sink term at the top side of concrete pavement. The one-dimensional finite difference method was employed to predict the temperature of concrete pavement at three different depths (i.e., 1 mm, 25 mm (1 inch), and 50 mm (2 inches)). The red line denotes the events when pavement temperature reached 0 °C, thereby creating the water freezing condition. The phase transformation of the PCM began between of 4 °C and 5.04 °C. Therefore, the heat release/absorption results in maintaining the pavement temperature above 0 °C for a relatively longer time (see Figure 62).

Figure 62(a) shows the temperature response of the top layer of concrete pavement (x=1 mm) in concrete pavements with and without the PCM. It was observed that temperature stays at a respectively higher degree in the concrete pavement with the PCM when the temperature of the layer drops below 5.04 °C (comparing the blue line to the green line in the figure). It is predicted that this temperature difference between two concrete pavements, with and without PCM, incrementally increases at the lower depths (x = 25, 50 mm), as shown in Figure 62(b) and (c). The water freezing times predicted for two concrete pavements are compared in Figure 63.

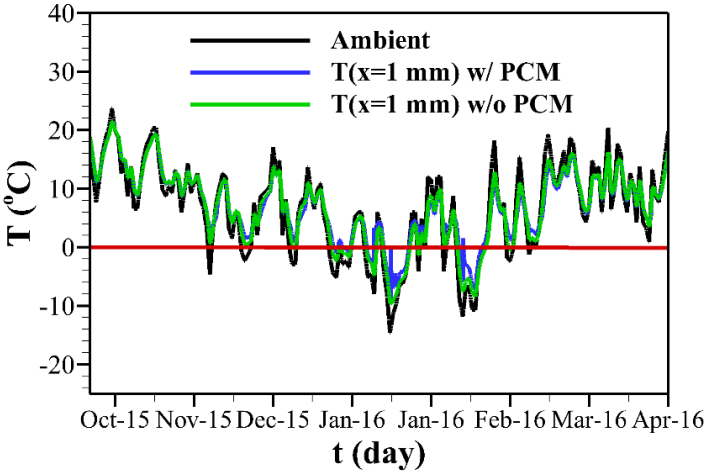

(a)

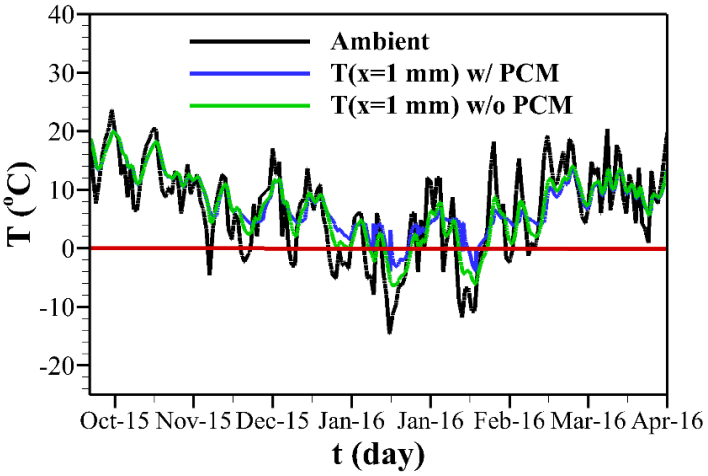

(b)

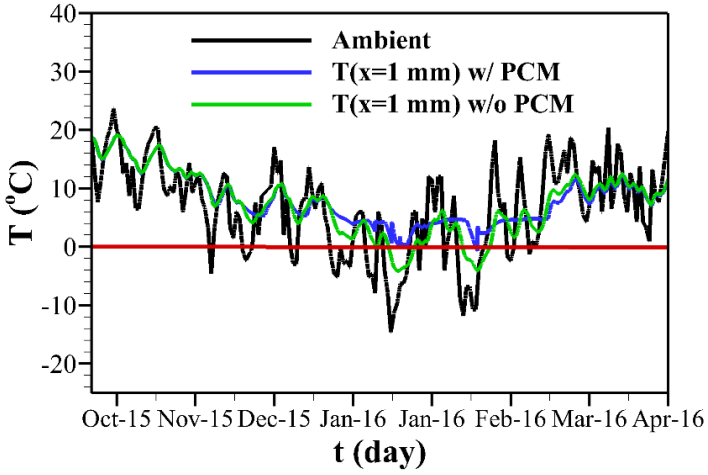

(c)

Figure 62. Temperature Prediction of PCM in Indianapolis International Airport at Depths of (a) 1mm, (b) 25mm, and (c) 50mm

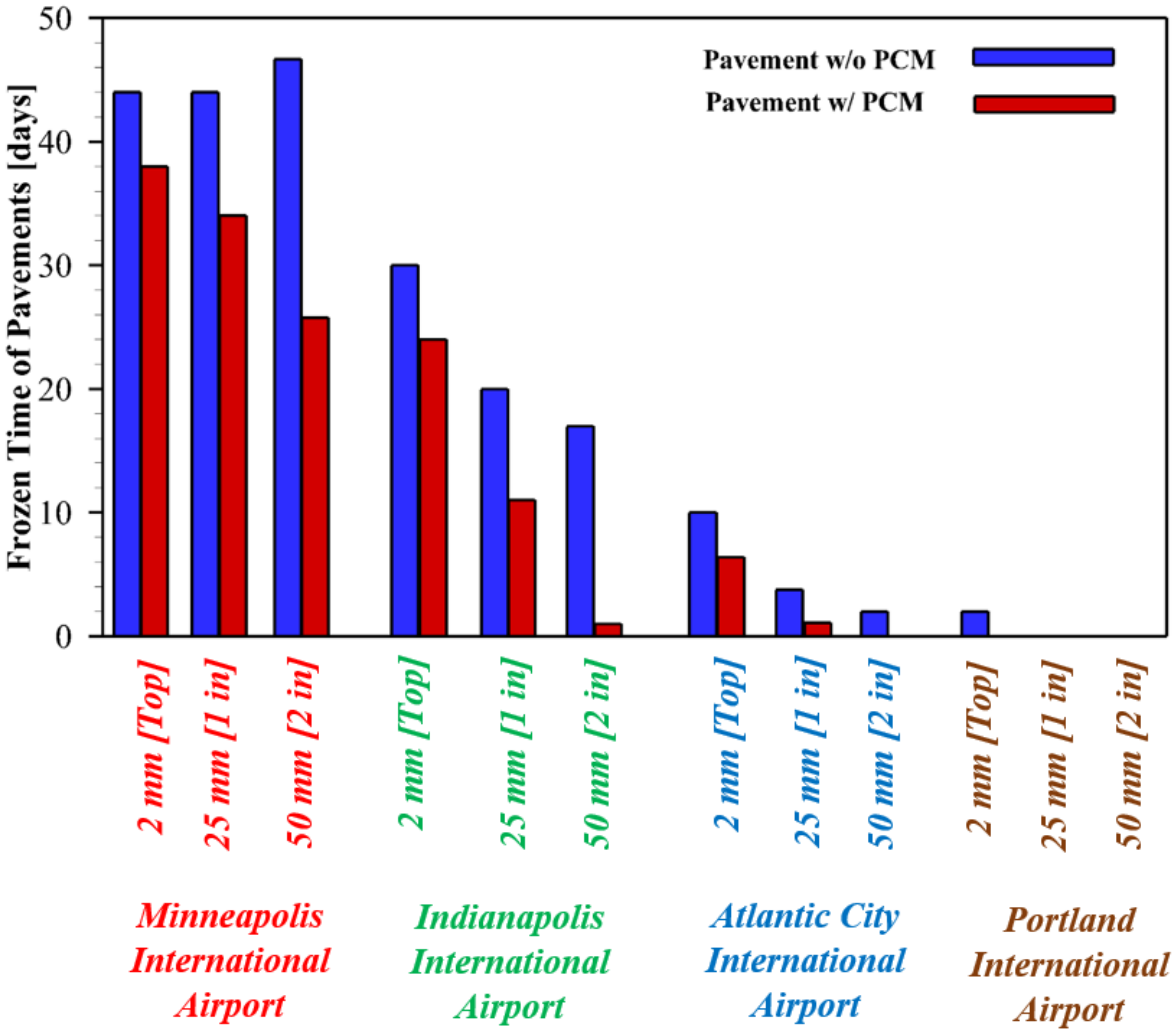

Figure 63. Numerical Prediction of the Time Period That Pavement at Various Depth Experiences 0 °C in Four Different Airports

7.6.3 Atlantic City International Airport

Atlantic City International Airport is located in a temperate zone with a moderate weather history. The average temperature history obtained shows that the concrete pavements are exposed to the water freezing condition (temperature below 0 °C) for 22 days in this location. The initial temperature of the entire experimental setup was set to the ambient temperature, as shown in Figure 64(a). Ambient temperature history serves as heat sink term at the top side of concrete pavement. The one-dimensional finite difference method was employed to predict the concrete pavement temperature at three different depths (i.e., 1 mm, 25 mm (1 inch), and 50 mm (2 inches)). The red line denotes the events when pavement temperature reached 0 °C, thereby creating the water freezing condition. The phase transformation of the PCM occurred between of 4 °C and 5.04 °C. Therefore, the heat release/absorption results in maintaining the pavement temperature above 0 °C for a relatively longer time (see Figure 64).

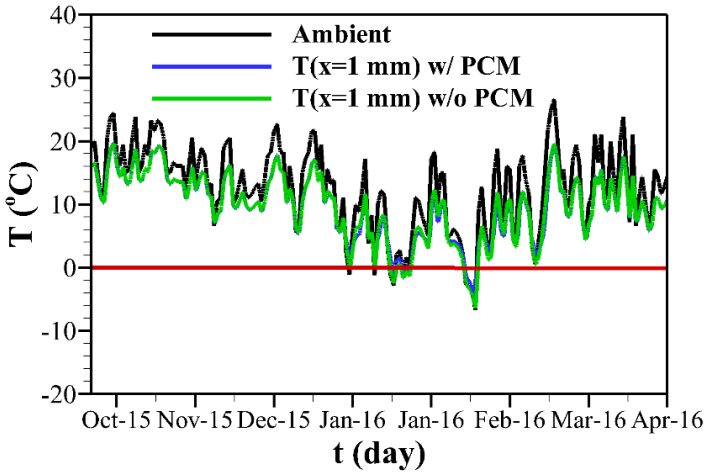

(a)

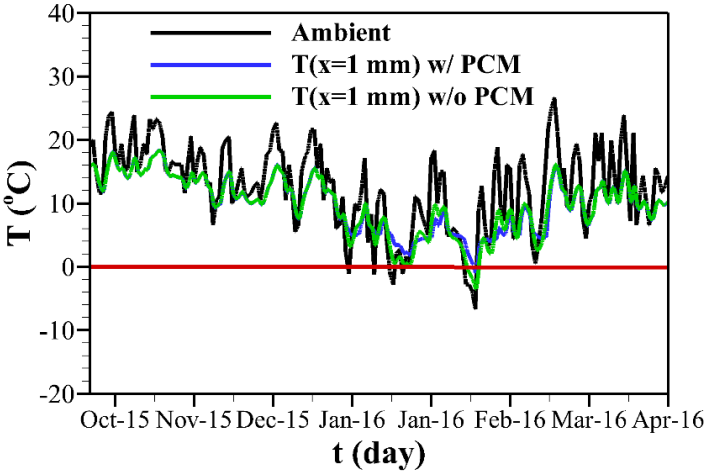

(b)

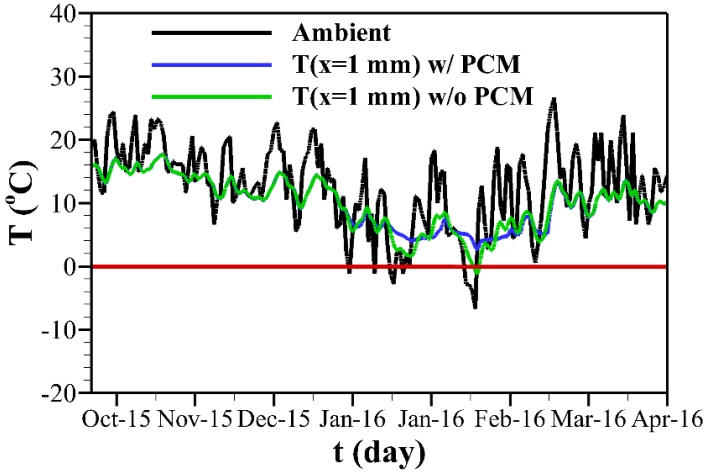

(c)

Figure 64. Temperature Prediction of PCM in Atlantic City International Airport at Depths of (a) 1mm, (b) 25mm, and (c) 50mm

Figure 64(a) shows the temperature response of the top layer of concrete pavement (x=1 mm) in concrete pavements with and without the PCM. It was observed that temperature respectively stays at higher degree in the concrete pavement with the PCM when the temperature of layer drops below 5.04 °C (comparing the blue line to the green line in the figure). It was predicted that this temperature difference between two concrete pavements with and without PCM incrementally increases at the lower depths (x=25, 50 mm), as shown in Figure 64(b) and (c).

7.6.4 Portland International Airport

Portland International Airport is located in a temperate zone with a relatively warm weather history. The average temperature history obtained shows that the concrete pavements are exposed to the water freezing condition (temperature below 0 °C) for only 2 days in this location. The initial temperature of the entire experimental setup was set to the initial ambient temperature, as shown in Figure 65(a). Ambient temperature history serves as heat sink term at the top side of concrete pavement. The one-dimensional finite difference method was employed to predict the temperature of concrete pavement at three different depths (i.e., 1 mm, 25 mm (1 inch), and 50 mm (2 inches)). The red line in Figure 65 denotes the events when temperature pavement reaches to 0 °C, thereby creating the water freezing condition. The phase transformation of the PCM began between 4 °C and 5.04 °C. Therefore, the heat release/absorption results in maintaining the pavement temperature above 0 °C for a relatively longer time (see Figure 6().

Figure 65(a) shows the temperature response of the top layer of concrete pavement (x = 1 mm) in concrete pavements with and without the PCM. It was observed that temperature stays at higher degree in the concrete pavement with the PCM respectively when the temperature of the layer drops below 5.04 °C (comparing the blue line to the green line in Figure 65). It was predicted that this temperature difference between two concrete pavements with and without PCM would increase incrementally at the lower depths (x=25, 50 mm), as shown in Figure 65(b) and (c).

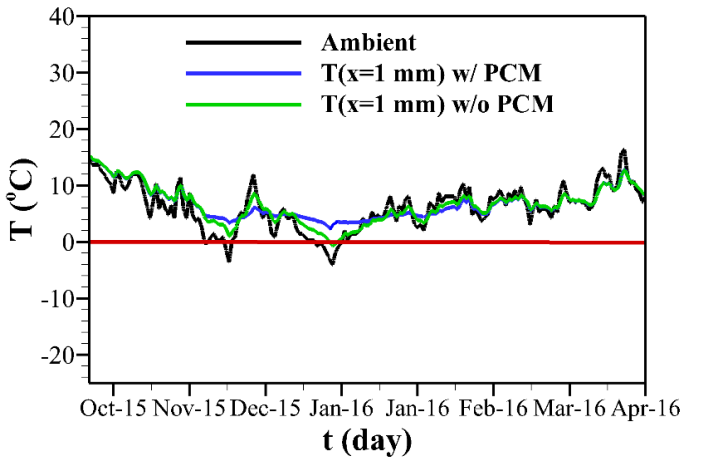

(a)

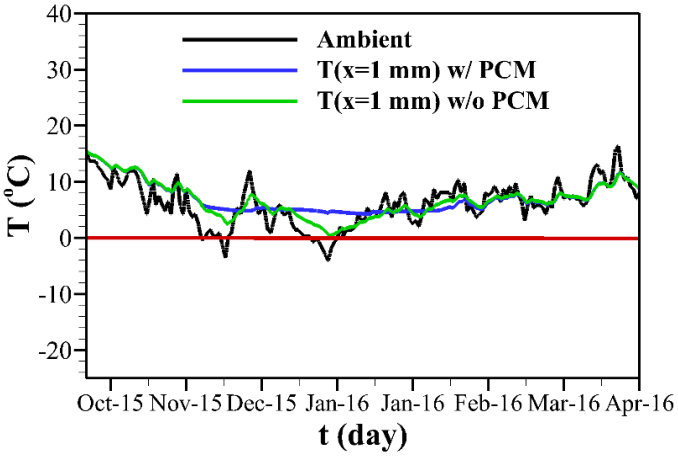

(b)

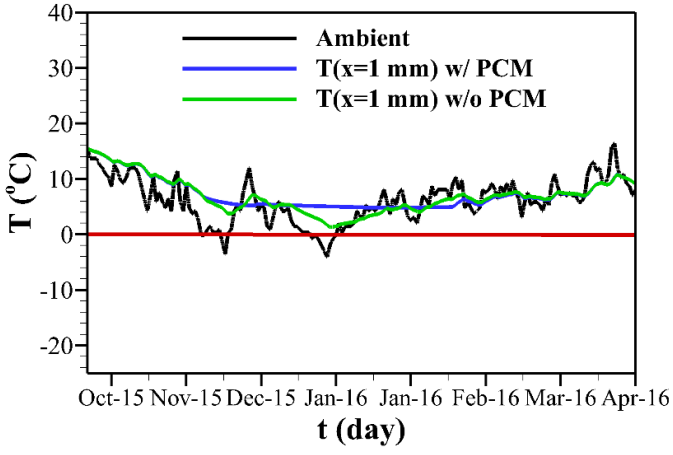

(c)

Figure 65. Temperature Prediction of PCM in Portland International Airport at Depths of (a) 1 mm, (b) 25 mm, and (c) 50 mm

7.6.5 Frozen Depth of Concrete Pavements at Different Airports

When the temperature of a layer decreases to 5.04 °C, the impregnated liquid PCM within LWA begins freezing. The ice formation continues until the temperature reaches 4 °C. In contrast, the formed solid PCM begins to melt when temperature increases to 4 °C. The formed solid PCM continues to melt until the temperature reaches 5.04 °C, at which the process of melting completely terminates. In conclusion, the solid PCM exists at a temperature below 5.04 °C, which can represent the frozen state of the PCM in the concrete pavements.

Figure 66 shows the frozen state of PCM in the pavement between October 15, 2015, and April 15, 2016, at four different airports. Figure 66(a) shows the frozen condition through the depth of pavement of PCM at Minneapolis-St. Paul International Airport. The white shading represents the frozen (solid) PCM, and the black shading represents the unfrozen (liquid) PCM. It was observed that the solid PCM began at the beginning of December and continued until the beginning of March (3 months). During this time period, the formation of solid PCM released latent heat to keep the temperature above 0 °C and reduced the risk of the water freezing in the pavement. It was predicted that the entire pavement (x = 216 mm) would undergo freezing of PCM from the middle of December until the beginning of February. During this time period, the whole amount of PCMs is activated to participate in releasing the heat energy to maximize the performance of the pavement in passive heating.

Figure 66(b) shows the frozen condition of PCM through the depth of pavement at Indianapolis International Airport. The white shading represents the frozen (solid) PCM, and the black shading represents the unfrozen (liquid) PCM. It was observed that the solid PCM began to form at the beginning of December and continued until the middle of February (2.5 months). During this time period, the formation of solid PCM released latent heat to keep the temperature above 0 °C and reduced the risk of the water freezing in the pavement. It was predicted that 95% of the pavement (x=204 mm) would undergo freezing of PCM.

Figure 66(c) shows the frozen condition of PCM through the depth of pavement at Atlantic City International Airport. The white shading represents the frozen (solid) PCM, and the black shading represents the unfrozen (liquid) PCM. It was observed that the solid PCM began to form at the beginning of January and continued until the beginning of February (1 month). During this time period, the formation of solid PCM released latent heat to keep the temperature above 0 °C and reduced the risk of the water freezing in the pavement. It was predicted that almost 48% of the pavement (x=103 mm) would undergo freezing of PCM.

Figure 66(d) shows the frozen condition of PCM through the depth of pavement at Portland International Airport. The white shading represents the frozen (solid) PCM, and the black shading represents the unfrozen (liquid) PCM. It was observed that the solid PCM began to form at the beginning of December and continues until the beginning of February (2 months). During this time period, the formation of solid PCM released latent heat to keep the temperature above 0 °C and reduced the risk of the water freezing in the pavement.

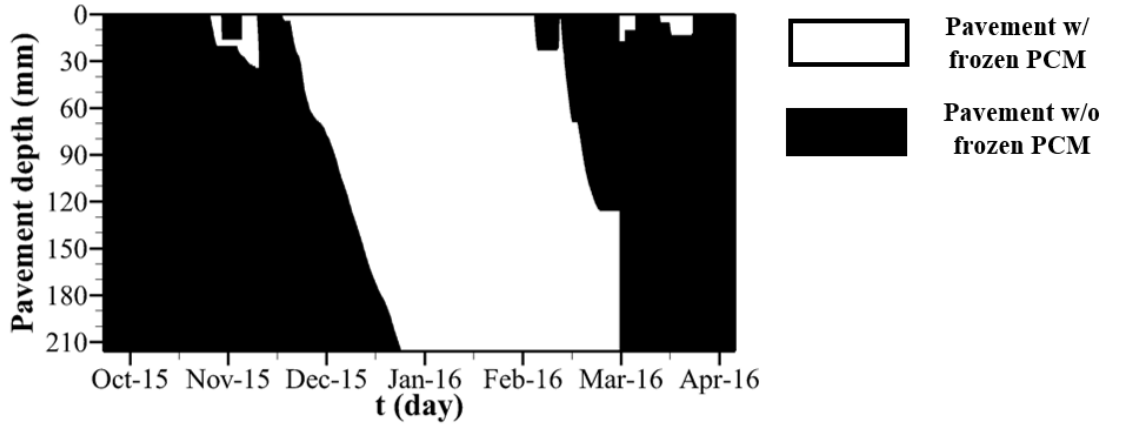
Pavement depth (mm)
0
30
60
90
120
150
180
210
Oct-15
Nov-15
Dec-15
Jan-16
Feb-16
Mar-16
Apr-16
t (day)
Pavement w/ frozen PCM
Pavement w/o frozen PCM

(a)

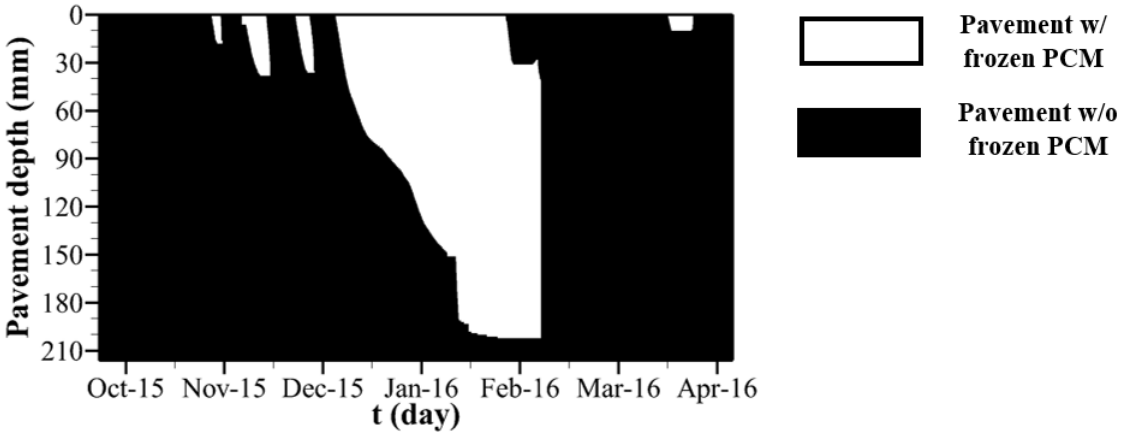
Pavement depth (mm)
0
30
60
90
120
150
180
210
Oct-15
Nov-15
Dec-15
Jan-16
Feb-16
Mar-16
Apr-16
t (day)
Pavement w/ frozen PCM
Pavement w/o frozen PCM

(b)

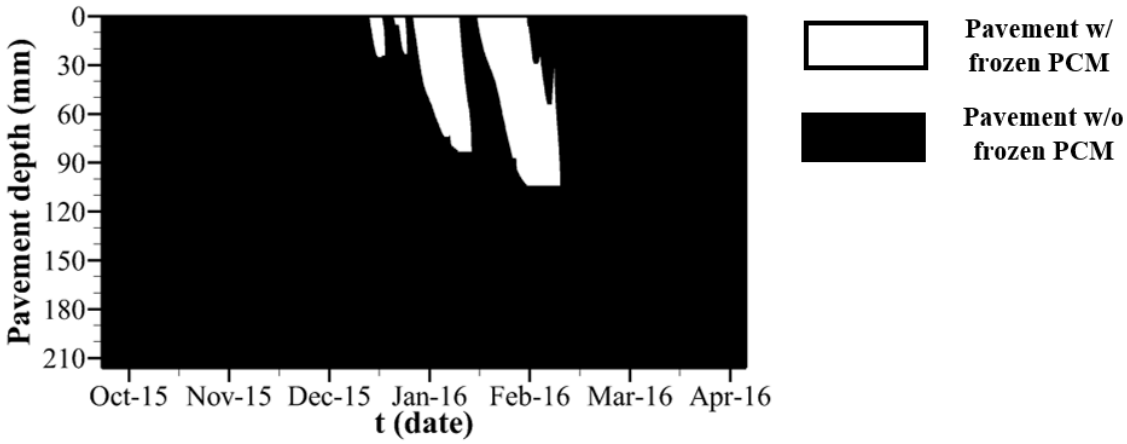
Pavement depth (mm)
0
30
60
90
120
150
180
210
Oct-15
Nov-15
Dec-15
Jan-16
Feb-16
Mar-16
Apr-16
t (date)
Pavement w/ frozen PCM
Pavement w/o frozen PCM

(c)

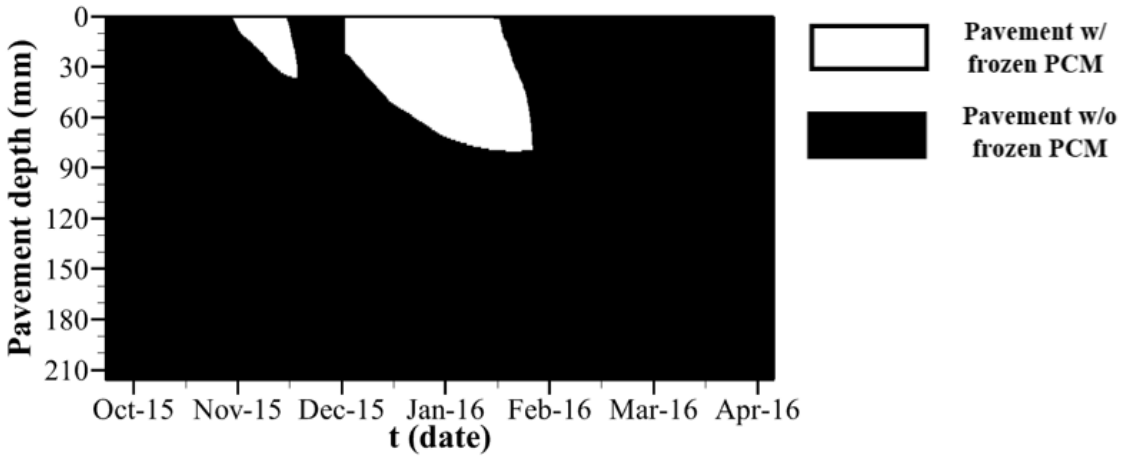

(d)

Figure 66. Numerical Results of Effective Depth of Concrete Pavement That Incorporated Paraffin Can Experience Phase Transformation during 6 months at (a) Minneapolis-St. Paul International Airport, (b) Indianapolis International Airport, (c) Atlantic City International Airport, and (d) Portland International Airport

The goals of this simulation were to predict the thermal behavior of pavements exposed to 6 months of cold weather and to assess the role of PCM in reduction of susceptibility to water freezing condition. To accomplish these goals, the frozen time of pavements was determined by calculating the time period at which the temperature of three different layers (x = 1 mm, 25 mm, and 50 mm) drops below 0 °C and increases the risk of ice formation. Figure 63 and Table 25 display the frozen time of pavements with and without PCM at four different airports. It was observed that the reduction in number of frozen days was considerable for two airports: Minneapolis-St. Paul and Indianapolis International Airports. This was likely due to relatively severe cold weather at these two locations. In Minneapolis-St. Paul, the pavement is expected to experience the water freezing condition for 6 days at 1-mm depth, 10 days at 25-mm depth, and 21 days at 50-mm depth. Similarly, it is expected that the pavement would experience 6 days less time of freezing at 1-mm depth, 9 days less at 25-mm depth, and 16 days less at 50-mm depth. However, less significant reduction in frozen time is predicted for Atlantic City and Portland International Airports because these airports are exposed to relatively moderate weather; they only experience water freezing conditions for 10 and 2 days, respectively. In Atlantic City International Airport, it was determined that the pavement only experiences 3 days less time of freezing at 1-mm, 2 days less at 25 mm, and 2 days less at 50 mm. Similarly, the pavement only experiences freezing of PCM for 2 days at 1-mm depth, and no solid PCM was predicted to form at 25-mm and 50-mm depths.

Table 25. Reduction in Frozen Time (days) of Pavement at Three Depths using PCM in Four Airports (as shown in Figure 65)

Airport	*Depth*	*1 mm*	*25 mm*	*50 mm*
Minneapolis-St. Paul	w/o PCM	44	44	46.6
	w/ PCM	38	34	25.7
	Reduction in time	6	10	20.9
Indianapolis	w/o PCM	30	20	17
	w/ PCM	24	11	1
	Reduction in time	6	9	16
Atlantic City	w/o PCM	10	3.7	2.0
	w/ PCM	6.4	1.1	0.0
	Reduction in time	3.6	2.6	2.0
Portland	w/o PCM	2.0	0.0	2.0
	w/ PCM	0.0	0.0	0.0
	Reduction in time	0.0	0.0	0.0

As shown in Figure 65(c) and (d), the number of the days at which the solid PCM exists at Portland International Airport is greater than at Atlantic City International Airport (white contour displays the formed solid PCM in the slab). However, the number of the days at which the top layers are susceptible to freezing (temperature below 0 °C) is greater at Atlantic City International Airport, where the imposed ambient temperature drops down to a minimum temperature of -6 °C to -7 °C, whereas, at Portland International Airport, the imposed ambient temperature reduces to a minimum temperature of -1 °C.

7.7 SUMMARY

This section presents the developed one-dimensional finite difference numerical model to determine the potential performance of a concrete that contains LWAs impregnated with PCMs. The model was used to predict the thermal behavior (i.e., temperature profile and heat flow) of concrete exposed to cooling and heating thermal cycles. The phase diagram of bulk PCM is used to calculate the quantity of the PCM that undergoes phase transformation, thereby estimating the amount of released/absorbed energy. Two sets of experiments were compared to the numerical results: (1) the LGCC test with an applied temperature range of +24 °C to -40 °C, and (2) large-scale slab test with an applied temperature range of +10 °C to -10 °C. In the LGCC experiment, it was determined that consideration of a gradual process of phase trnasformation for the PCM can lead to a promising agreement between experimental data and numerical results. As a result, this assumption is considered in large-scale slab experiments at which maximum absolute temperature differences of 1.275 °C and 1.289 °C are obtained for concrete slabs without and with the PCM, respectively. Finally, the role of PCM on the reduction of time at which the concrete pavement is susceptible to water freezing condition was studied from October 15, 2015 to April 15, 2016. The numerical results showed that the concrete pavement can significantly experience a shorter time of ice formation at three depths of 2 mm, 25 mm, and 50 mm at both Minneapolis-St. Paul International and Indianapolis International Airports. Due to relatively moderate weather conditions in Atlantic City International and Portland International Airports, the concrete pavements are less susceptible to ice formation during the 6-month period.

8. CONCLUSIONS

This report discusses the potential use of Phase Change Materials (PCMs) in airfield concrete pavements to store heat that can be used to reduce ice formation and snow accumulation on the surface of the concrete pavement. This work mainly attempts to (1) determine the most desirable properties of the PCM-concrete composite, (2) determine the PCM materials to use and to determine how these PCMs can be manufactured, and (3) evaluate the performance of pavements containing PCM.

This study promotes understanding of how PCMs can be incorporated in concrete pavement to revolutionize anti-icing/snow-removal practices in airfield concrete pavement technologies. This study also shows that PCM incorporation in concrete pavement can be used to melt ice and snow, thereby decreasing the needs to use classical snow/ice removal methods such as snow plowing or deicing salt treatment.

The main conclusions of this study are as follows.

- Several types of PCMs were examined including vegetable-based (fatty acids and methyl esters) and petroleum-based (paraffin oil) PCMs. The thermal properties of PCMs are evaluated. The temperature of the liquid-solid phase transition was determined, and the latent heat absorbed or released during the phase change was measured. The thermal properties of PCMs can be changed by altering the compositions to remain in the desired temperature range for concrete pavement anti-icing applications.

- Binary mixtures of fatty acid methyl esters and paraffin oil provide desirable thermal properties for use as low temperature PCMs to improve anti-icing practices. Specifically, methyl laurate + methyl myristate and methyl laurate + methyl palmitate binary mixtures at their eutectic compositions are promising sustainable PCMs with melting temperatures of 0.21 °C and 2.4 °C and the latent heat of fusion of 174.3 $J \cdot g^{-1}$ and 166.5$\cdot J\ g^{-1}$, respectively.

- Phase diagrams were developed for binary mixtures of fatty acid methyl esters that can provide valuable information about the thermal properties at a range of methyl ester compositions. This information can be used in mathematical model development for simulating the anti-icing behaviors of these PCMs in concrete.

- Different approaches were evaluated to incorporate PCMs in concrete for effective use to reduce ice and snow without damaging the concrete pavement. This study used two methods: (1) using LWAs containing PCM and (2) using embedded pipes filled with PCM. The embedded pipes seem to be less practical in real application because of their complexity. However, for proof of concept, embedded pipes allow the PCM to be more easily incorporated into the pavement materials in the laboratory. Both LWAs and embedded pipes were found to be effective in incorporating PCMs and storing energy in concrete to melt ice and snow.

- The inclusion of the PCM in LWA can be used as a technology to incorporate PCMs in concrete pavement. Several LWAs were examined and PCMs can absorb sufficient amount, and PCM-impregnated LWA can be used to make concrete. This method is more feasible in practice to incorporate PCMs in concrete compared to using embedded pipes. Further research

is needed to compare the economic aspects of using different methods to incorporate PCMs in the concrete pavement.

- Chemical and physical durability aspects of incorporating PCMs in concrete were also assessed. When the PCM was stored in LWA and placed in the concrete, some PCMs (for example methyl laurate) reacted with cementitious materials creating cracking and damage in concrete. Embedded pipes were found to be more effective than LWA in eliminating the reaction by preventing concrete-PCM interactions.

- PCM was incorporated in large-scale concrete slabs to melt snow/ice during cooling events. Again, two methods were used to incorporate PCM into concrete slabs: (a) placing the PCM in LWA and using the LWA containing PCM to make the concrete slab, and (b) placing the PCM in embedded pipes that were fabricated inside the concrete slabs during concrete casting. Both approaches showed promising capabilities to melt snow/ice on the surface of the concrete slabs. However, the capability of snow melting in the slabs with embedded pipes containing PCMs could substantially decrease when the concrete slab is exposed to an ambient temperature near or below the freezing temperature of PCM before a snow event. When the PCM was placed in the LWA, a gradual heat release (due to pore size effect) was observed that can be used in a wide range of temperature variation and the snow-melting capability remains relatively beneficial.

- Other factors should be investigated on a large-scale to further understand the effect of using PCMs in concrete for snow melting and for concrete performance. Some of the factors are durability of concrete pavement, skid resistance for transportation safety, and long-term stability of PCMs in concrete pavements.

- A one-dimensional finite difference numerical model was developed to predict the macroscopic freeze-thaw behavior in concrete. The thermal response of the concrete was estimated using this model, and it was used to predict the thermal behavior (i.e., temperature profile and heat flow) of concrete exposed to cooling and heating thermal cycles. The computational results were compared to and verified with the experimental ones. This model can be used to simulate PCM incorporation in concrete pavemenet applications.

- Using the developed model, the thermal response of concrete pavements containing PCMs was simulated at four U.S. airports (Minneapolis-St. Paul, Indianapolis, Atlantic City, and Portland) to determine the optimum performance of PCMs in various weather (i.e., temperature conditions). It was found that incorporating PCMs in concrete pavement can be very effective in reducing the number of freezing events in concrete pavement. This model can be used to predict the thermal behavior of pavement containing PCM at different locations in the United States. Further, numerical research needs to be done to evaluate the snow-melting capibilty of pavement containing PCM.

In general, this study has helped to (1) determine the most desirable properties of the PCM-concrete composite, (2) determine the PCM materials to use and to determine how these PCMs can be manufactured, (3) determine the methodology that can be used to incorporate PCM into concrete pavement, (4) evaluate the performance of pavements containing PCM, and (5) predict and optimize the thermal behavior of concrete pavement containing PCM in different

environmental conditions using the developed numerical model. This study also shows that PCM can be used to melt snow/ice on pavement, thereby decreasing the needs to use classical snow/ice removal methods such as snow plowing or deicing salt treatment.

9. REFERENCES

Abhat, A. (1983). Low temperature latent heat thermal energy storage: Heat storage materials. *Solar Energy*, *30*(4), 313–332. https://doi.org/10.1016/0038-092X(83)90186-X

Andersson, K., Allard, B., Bengtsson, M., & Magnusson, B. (1989). Chemical composition of cement pore solutions. *Cement and Concrete Research*, *19*(3), 327–332. https://doi.org/10.1016/0008-8846(89)90022-7

Askeland, D. R., & Pradeep, P. P. (2003). *The science and engineering of materials* (4th ed.). Cengage.

ASTM International. (2009). *Standard test method for pulse velocity through concrete* (ASTM C597-09). https://www.astm.org/c0597-09.html

ASTM International. (2012). *Standard practice for mechanical mixing of hydraulic cement pastes and mortars of plastic consistency* (ASTM 305-12). https://www.astm.org/c0305-12.html

ASTM International. (2013a). *Standard test method for compressive strength of hydraulic cement mortars (using 2-in. or [50-mm] cube specimens)* (ASTM C109/C109M). https://www.astm.org/c0109_c0109m-13.html

ASTM International. (2013b). *Standard test method for sieve analysis of fine and coarse aggregates* (ASTM C136/C136M-19). https://www.astm.org/c0136_c0136m-19.html

ASTM International. (2013c). *Standard test method for thermal conductivity of solids by means of the guarded-comparative-longitudinal heat flow technique* (ASTM E1225-09). https://www.astm.org/e1225-09.html

ASTM International. (2017). *Standard test method for thermal transmission properties of thermally conductive electrical insulation materials* (ASTM D5470-12). https://www.astm.org/d5470-12.html

Bentz, D. (2000). *A computer model to predict the surface temperature and time-of-wetness of concrete pavements and bridge decks* (NISTIR-6551). National Institute of Standards and Technology. https://www.nist.gov/publications/computer-model-predict-surface-temperature-and-time-wetness-concrete-pavements-and

Bentz, D. P. & Turpin, R. (2007). Potential applications of phase change materials in concrete technology. *Cement and Concrete Composites*, *29*(7), 527–532. https://doi.org/10.1016/j.cemconcomp.2007.04.007

Bentz, D., Peltz, M., Duran-Herrera, A., Valdez, P., & Juarez, C. A. (2010). Thermal properties of high-volume fly ash mortars and concretes. *Journal of Building Physics*, *34*(3), 263–275. https://doi.org/10.1177/1744259110376613

Beddoe, R., & Setzer, M. (1988). A low-temperature DSC investigation of hardened cement paste subjected to chloride action. *Cement and Concrete Research*, *18*(2), 249–256. https://doi.org/10.1016/0008-8846(88)90009-9

Bo, G., Biao, M., and Fang, Q. (2011, May 20–22). *Application of asphalt pavement with phase change materials to mitigate urban heat island effect*. 2011 International Symposium on Water Resource and Environmental Protection, Xi'an, China. https://doi.org/10.1109/ISWREP.2011.5893749

British Standards Institution. (2011), *Fat and oil derivatives—Fatty Acid Methyl Esters (FAME)—Determination of ester and linolenic acid methyl ester contents* (British Implementation of European Standards Document BS EN: 14103:2011).

Brun, M., Lallemand, A., Quinson, J-F., Eyraud, C. (1977). A new method for the simultaneous determination of the size and shape of pores: the thermoporometry. *Thermochimica Acta*, *21*(1), 59–88. https://doi.org/10.1016/0040-6031(77)85122-8

Cai, H., & Liu, X. (1998). Freeze-thaw durability of concrete: ice formation process in pores. *Cement and Concrete Research*, *28*(9), 1281–1287. https://doi.org/10.1016/S0008-8846(98)00103-3

Callister, W. D., & Rethwisch, D. (2009). *Materials science and engineering: An introduction* (8th ed.). John Wiley & Sons.

Campbell-Allen, D., & Thorne, C. P. (1963). The thermal conductivity of concrete. *Magazine of Concrete Research*, *15*(43), 39–48. https://doi.org/10.1680/macr.1963.15.43.39

Carareto, N. D. D., Costa, M. C., Rolemberg, M. P., Krähenbühl, M. A., & Meirelles, A. J. A. (2011). The solid–liquid phase diagrams of binary mixtures of even saturated fatty alcohols. *Fluid Phase Equilibria*, *303*(2), 191.e1–191.e8. https://doi.org/10.1016/j.fluid.2011.01.028

Carareto, N. D. D., dos Santos, A. O., Rolemberg, M. P., Cardoso, L.P., Costa, M. C., & Meirelles, A. J. A. (2014). On the solid–liquid phase diagrams of binary mixtures of even saturated fatty alcohols: systems exhibiting peritectic reaction. *Thermochimica Acta*, *589*, 137–147. https://doi.org/10.1016/j.tca.2014.05.022

Castro, J., Bentz, D., & Weiss, J. (2011). Effect of sample conditioning on the water absorption of concrete. *Cement and Concrete Composites*, *33*(8), 805–813. https://doi.org/10.1016/j.cemconcomp.2011.05.007

Castro, J., Keiser, L., Golias, M., & Weiss, J. (2011, November). Absorption and desorption properties of fine lightweight aggregate for application to internally cured concrete mixtures, *Cement and Concrete Composites*, *33*(10), 1001–1008. https://doi.org/10.1016/j.cemconcomp.2011.07.006

Chen, Z., Cao, L., Shan, F., & Fang, G. (2013). Preparation and characteristics of microencapsulated stearic acid as composite thermal energy storage material in buildings. *Energy and Buildings*, *62*, 469–474. https://doi.org/10.1016/j.enbuild.2013.03.025

Chernik, G. (1995). Phase equilibria in phospholipid-water systems. *Advances in Colloid and Interface Science*, *61*, 65–129. https://doi.org/10.1016/0001-8686(95)00262-O

Choi, W.-C., Khil, B.-S., Chae, Y.-S., Liang, Q.-B., & Yun, H.-D. (2014). Feasibility of using phase change materials to control the heat of hydration in massive concrete structures. *The Scientific World Journal*, *2014*, 1–6. https://doi.org/10.1155/2014/781393

Cocu, X., Nicaise, D., & Rachidi, S. (2010, February). *The use of phase change materials to delay pavement freezing*. XIII International Winter Road Congress, PIARC, Quebec, Canada.

Costa, M., Buddhi, D., & Oliva, A. (1998). Numerical simulation of a latent heat thermal energy storage system with enhanced heat conduction. *Energy Conversion and Management*, *39*(3–4), 319–330. https://doi.org/10.1016/S0196-8904(96)00193-8

Costa, M. C., Rolemberg, M. P., Boros, L. A. D., Krähenbühl, M. A., de Oliveira, M. G., & Meirelles, A. J. A. (2007). Solid−liquid equilibrium of binary fatty acid mixtures. *Journal of Chemical and Engineering Data*, *52*(1), 30–36. https://doi.org/10.1021/je060146z

Costa, M. C., Sardo, M., Rolemberg, M. P., Coutinho, J. A. P., Meirelles, A. J. A., Ribeiro-Claro, P., & Krähenbühl, M. A. (2009a). The solid-liquid phase diagrams of binary mixtures of consecutive, even saturated fatty acids. *Chemistry and Physics of Lipids*, *160*(2), 85–97. https://doi.org/10.1016/j.chemphyslip.2009.05.004

Costa, M. C., Sardo, M., Rolemberg, M. P., Ribeiro-Claro, P., Meirelles, A. J. A., Coutinho, J. A. P., & Krähenbühl, M. A. (2009b). The solid-liquid phase diagrams of binary mixtures of consecutive, even saturated fatty acids: differing by four carbon atoms. *Chemistry and Physics of Lipids*, *157*(1), 40–50. https://doi.org/10.1016/j.chemphyslip.2008.09.006

Costa, M. C., Rolemberg, M. P., Meirelles, A. J. A., Coutinho, J. A. P., & Krähenbühl, M. A. (2009). The solid–liquid phase diagrams of binary mixtures of even saturated fatty acids differing by six carbon atoms. *Thermochimica Acta*, *496*(1–2), 30–37. https://doi.org/10.1016/j.tca.2009.06.018

Costa, M. C., Boros, L. A. D., Coutinho, J. A. P., Krähenbühl, M. A., & Meirelles, A. P. (2011). Low-temperature behavior of biodiesel: solid-liquid phase diagrams of binary mixtures composed of fatty acid methyl esters. *Energy & Fuels*. *25*(7), 3244–3250. https://doi.org/10.1021/ef2004199

Daian, J-F. (1988). Condensation and isothermal water transfer in cement mortar Part I—Pore size distribution, equilibrium water condensation and imbibition. *Transport in Porous Media*, *3*, 563–589. https://doi.org/10.1007/BF00959103

Debenedetti, P. & Stanley, H. E. (2003). Supercooled and glassy water. *Physics Today*, *56*(6), 40–46. https://doi.org/10.1063/1.1595053

Dunn, R. O. (2008, October). Crystallization behavior of fatty acid methyl esters. *Journal of the American Oil Chemists' Society*, *85*(10), 961–972. https://doi.org/10.1007/s11746-008-1279-x

Dunn, R. O. (2012) Effects of high-melting methyl esters on crystallization properties of fatty acid methyl ester mixtures. *Transactions of the American Society of Agricultural and Biological Engineers*, *55*(2), 637–646. https://doi.org/10.13031/2013.41365

Esmaeeli, H. S., Farnam, Y., Bentz, D., Zavattieri, P. D., & Weiss, J. (2016). Numerical simulation of the freeze-thaw behavior of mortar containing deicing salt solution. *Materials and Structures*, *50*. https://doi.org/10.1617/s11527-016-0964-8

Farnam, Y. (2015). Damage development, phase changes, transport properties, and freeze-thaw performance of cementitious materials exposed to chloride based salts (Publication No. AAT 3735806) [Doctoral dissertation, Purdue University]. ProQuest Dissertations and Theses. https://www.proquest.com/openview/638a81db310b3628170ee14fa4679e6f/1?pq-origsite=gscholar&cbl=18750&diss=y

Farnam, Y., Bentz, D., Hampton, A., & Weiss, J. (2014, January 1). Acoustic emission and low-temperature calorimetry study of freeze and thaw behavior in cementitious materials exposed to sodium chloride salt. *Journal of the Transportation Research Board*, *2441*(1), 81–90. https://doi.org/10.3141/2441-11

Farnam, Y., Bentz, D., Sakulich, A., Flynn, D., & Weiss, D. (2014, June 23) Measuring freeze and thaw damage in mortars containing deicing salt using a low-temperature longitudinal guarded comparative calorimeter and acoustic emission. *Advances in Civil Engineering Materials*, *3*(1). https://doi.org/10.1520/ACEM20130095

Farnam, Y., Dick, S., Wiese, A., Davis, J., Bentz, D., & Weiss, J. (2015). The influence of calcium chloride deicing salt on phase changes and damage development in cementitious materials. *Cement and Concrete Composites*, *64*, 1–15. https://doi.org/10.1016/j.cemconcomp.2015.09.006

Farnam, Y., Esmaeeli, H. S., Bentz, D., & Zavattieri, P. (2015, June 1–3). Experimental and numerical investigation on the effect of cooling/heating rate on the freeze-thaw behavior of mortar containing deicing salt solution [Conference paper]. *International Conference on the Regeneration and Conservation of Concrete Structures*. Nagasaki, Japan. https://www.researchgate.net/publication/280738964_Experimental_and_Numerical_Investigation_on_the_Effect_of_CoolingHeating_Rate_on_the_Freeze-Thaw_Behavior_of_Mortar_Containing_Deicing_Salt_Solution

Farnam, Y., Geiker, M. R., Bentz, D., & Weiss, J. (2015). Acoustic emission waveform characterization of crack origin and mode in fractured and ASR damaged concrete. *Cement and Concrete Composites*, *60*, 135–145. https://doi.org/10.1016/j.cemconcomp.2015.04.008

Farnam, Y., Todak, H., Spragg, R., & Weiss, J. (2015). Electrical response of mortar with different degrees of saturation and deicing salt solutions during freezing and thawing. *Cement and Concrete Composites*, *59*, 49–59. https://doi.org/10.1016/j.cemconcomp.2015.03.003

Farnam, Y., Wiese, A., Bentz, D., Davis, J., & Weiss, J. (2015). Damage development in cementitious materials exposed to magnesium chloride deicing salt. *Construction and Building Materials*, *93*, 384–392. https://doi.org/10.1016/j.conbuildmat.2015.06.004

Farnam, Y., Krafcik, M., Liston, L., Washington, T., Erk, K., Tao, B., & Weiss, J. (2016). Evaluating the use of phase change materials in concrete pavement to melt ice and snow. *Journal of Materials in Civil Engineering*, *28*(4). https://doi.org/10.1061/(ASCE)MT.1943-5533.0001439

Farnam, Y., Villani, C., Washington, T., Spence, M., Jain, J., and Weiss, J. (2016). Performance of carbonated calcium silicate based cement pastes and mortars exposed to NaCl and $MgCl_2$ deicing salt. *Construction and Building Materials*, *111*, 63–71. https://doi.org/10.1016/j.conbuildmat.2016.02.098

Fernandes, F., Manari, S., Aguayo, M., Santos, K., Oey, T., Wei, Z., Falzone, G. Neithalath, N., & Sant, G. (2014). On the feasibility of using phase change materials (PCMs) to mitigate thermal cracking in cementitious materials. *Cement and Concrete Composites*, *51*, 14–26. https://doi.org/10.1016/j.cemconcomp.2014.03.003

Fletcher, N. H. (2010). *The chemical physics of ice*. Cambridge University Press.

Foon, C. S., Liang, Y. C., Mat Dian, N. L. H., May, C. Y., Hock, C. C., & Ngan, M. A. (2006). Crystallisation and melting behavior of methyl esters of palm oil. *American Journal of Applied Sciences*, *3*(5). 1859–1863. http://dx.doi.org/10.3844/ajassp.2006.1859.1863

Fukai, J., Hamada, Y., Morozumi, Y., Miyatake, O. (2003). Improvement of thermal characteristics of latent heat thermal energy storage units using carbon-fiber brushes: experiments and modeling. *International Journal of Heat and Mass Transfer*, *46*(23), 4513–4525. https://doi.org/10.1016/S0017-9310(03)00290-4

Gamsjäger, H., Lorimer, J. W., Scharlin, P., & Shaw, D. G. (2008). Glossary of terms related to solubility (IUPAC Recommendations 2008). *Pure and Applied Chemistry*, *80*(2), 233–276. https://doi.org/10.1351/pac200880020233

Gong, Z-X., & Mujumdar, A. S. (1997). Finite-element analysis of cyclic heat transfer in a shell-and-tube latent heat energy storage exchanger. *Applied Thermal Engineering*, *17*(6), 583–591. https://doi.org/10.1016/S1359-4311(96)00054-3

Gunstone, F. D. (2008). *Oils and fats in the food industry*. Wiley-Blackwell.

Hamada, Y., Ohtsu, W., & Fukai, J. (2003). Thermal response in thermal energy storage material around heat transfer tubes: effect of additives on heat transfer rates. *Solar Energy*, *75*(4), 317–328. https://doi.org/10.1016/j.solener.2003.07.028

Han, B., Choi, J. H., Dantzig, J. A., & Bischof, J. C. (2006). A quantitative analysis on latent heat of an aqueous binary mixture. *Cryobiology*, *52*(1), 146–51. https://doi.org/10.1016/j.cryobiol.2005.09.007

Hawes, D. W., Banu, D., & Feldman, D. (1992, July). The stability of phase change materials in concrete. *Solar Energy Materials and Solar Cells*, *27*(2), 103–118. https://doi.org/10.1016/0927-0248(92)90113-4

Hawes, D. W. & Feldman, D. (1992, July). Absorption of phase change materials in concrete. *Solar Energy Materials and Solar Cells*, *27*(2), 91–101. https://doi.org/10.1016/0927-0248(92)90112-3

Haynes, W. M. (Ed.) (2013). *CRC Handbook of Chemistry and Physics: A Ready-Reference Book of Chemical and Physical Data* (94th Edition). Taylor & Francis.

Hembade, L., Neithalath, N., & Rajan, S. D. (2014). Understanding the energy implications of phase-change materials in concrete walls through finite-element analysis. *Journal of Energy Engineering*, *140*(1). https://doi.org/10.1061/(ASCE)EY.1943-7897.0000146

Henkensiefken, R., Bentz, D., Nantung, T., & Weiss, J. (2009). Volume change and cracking in internally cured mixtures made with saturated lightweight aggregate under sealed and unsealed conditions. *Cement and Concrete Composites*, *31*(7), 427–437. https://doi.org/10.1016/j.cemconcomp.2009.04.003

Hibbert, S. E., Markatos, N. C., & Voller, V. R. (1988). Computer simulation of moving-interface, convective, phase-change processes. *International Journal of Heat and Mass Transfer*, *31*(9), 1785–1795. https://doi.org/10.1016/0017-9310(88)90193-7

Hilsenrath, J., Beckett, C. W., Benedict, W. S., Fano, L., Hoge, H. J., Masi, J. F., Nuttall, R. L., Touloukian, T. S., Woolley, H. W., &King, C. V. (1956). Tables of thermal properties of gases. *Journal of the Electrochemical Society*, *103*(5), 124C. https://doi.org/10.1149/1.2430297

Inoue, T., Hisatsugu, Y., Yamamoto, R., & Suzuki, M. (2004, February). Solid–liquid phase behavior of binary fatty acid mixtures: 1. Oleic acid/stearic acid and oleic acid/behenic acid mixtures. *Chemistry and Physics of Lipids*, *127*(2), 143–152. https://doi.org/10.1016/j.chemphyslip.2003.09.014

Inoue, T., Hisatsugu, Y., Ishikawa, R., Suzuki, M. (2004, February). Solid–liquid phase behavior of binary fatty acid mixtures: 2. Mixtures of oleic acid with lauric acid, myristic acid, and palmitic acid. *Chemistry and Physics of Lipids*. *127*(2), 161–173. https://doi.org/10.1016/j.chemphyslip.2003.10.013

Inoue, T., Hisatsugu, Y., Suzuki, M., Wang, Z., & Zheng, L. (2004, December). Solid-liquid phase behavior of binary fatty acid mixtures: 3. Mixtures of oleic acid with capric acid (decanoic acid) and caprylic acid (octanoic acid). *Chemistry and Physics of Lipids*, *132*(2), 225–34. https://doi.org/10.1016/j.chemphyslip.2004.07.004

Incropera, F. P., DeWitt, D. P., Bergman, T. L., & Lavine, A. S. (2006). *Fundamentals of heat and mass transfer* (6th ed.). John Wiley & Sons.

Ismail, K. A. R., & Abugderah, M. M. (2000). Performance of a thermal storage system of the vertical tube type. *Energy Conversion and Management*, *41*(11), 1165–1190. https://doi.org/10.1016/S0196-8904(99)00140-5

Ismail, K. A. R., Da Silva, M. (2003). Numerical solution of the phase change problem around a horizontal cylinder in the presence of natural convection in the melt region. International *Journal of Heat and Mass Transfer*, *46*(10), 1791–1799. https://doi.org/10.1016/S0017-9310(02)00487-8

Jones, W., Farnam, Y., Imbrock, P., Spiro, J., Villani, C., Olek, J., Golias, M. & Weiss, J. (2013). *An overview of joint deterioration in concrete pavement: mechanisms, solution properties, and sealers*. Purdue University, West Lafayette, IN. https://doi.org/10.5703/1288284315339

Kalnæs, S. E., & Jelle, B. P. (2015). Phase change materials for building applications: a state-of-the-art review and future research opportunities. *Energy and Buildings*, *94*, 150–176. https://doi.org/10.1016/j.enbuild.2015.02.023

Karaipekli, A., & Sarı, A. (2008). Capric–myristic acid/expanded perlite composite as form-stable phase change material for latent heat thermal energy storage. *Renewable Energy*, *33*(12), 2599–2605. https://doi.org/10.1016/j.renene.2008.02.024

Kaufmann, J. (1999). Experimental identification of damage mechanisms in cementitious porous materials on phase transition of pore solution under deicing salt attack [Thesis, École Polytechnique Fédérale de Lausanne (EPFL)] Infoscience EPFL scientific publications. https://doi.org/10.5075/epfl-thesis-2037

Kumar, R., & Bhattacharjee, B. (2003). Porosity, pore size distribution and in situ strength of concrete. *Cement and Concrete Research*, *33*(1) 155–164. https://doi.org/10.1016/S0008-8846(02)00942-0

Kuznik, F., & Virgone, J. (2009). Experimental assessment of a phase change material for wall building use. *Applied Energy*, *86*(10), 2038–2046. https://doi.org/10.1016/j.apenergy.2009.01.004

Lane, G. A. (1989). Phase change thermal storage materials. In Guyer, C. (Ed.), *Handbook of Applied Thermal Design*. McGraw Hill.

Lecomte, D., & Mayer, D. (1985). Design method for sizing a latent heat store/heat exchanger in a thermal system. *Applied Energy*, *21*(1) 55–78. https://doi.org/10.1016/0306-2619(85)90074-1

Levy, O., & Stroud, D. (1997). Maxwell Garnett theory for mixtures of anisotropic inclusions: Application to conducting polymers. *Physical Review B*, *56*(13), 8035–8046. https://doi.org/10.1103/PhysRevB.56.8035

Li, W., Sun, W., & Jiang, J. (2011). Damage of concrete experiencing flexural fatigue load and closed freeze/thaw cycles simultaneously. *Construction and Building Materials*, *25*(5), 2604–2610. https://doi.org/10.1016/j.conbuildmat.2010.12.007

Li, W., Pour-Ghaz, M., Castro, J., & Weiss, J. (2012). Water absorption and critical degree of saturation relating to freeze-thaw damage in concrete pavement joints. *Journal of Materials in Civil Engineering*, *24*(3), 299–307. https://ascelibrary.org/doi/abs/10.1061/%28ASCE%29MT.1943-5533.0000383

Ling, T.C. & Poon, C.S. (2013, September). Use of phase change materials for thermal energy storage in concrete: An overview. *Construction and Building Materials*, *46*, 55–62. https://doi.org/10.1016/j.conbuildmat.2013.04.031

Liston, L. C., Krafcik, M., Farnam, Y., Tao, B., Erk, K., & Weiss, J. (2014, August 5–7). Toward the use of phase change materials (PCM) in concrete pavements: Evaluation of thermal properties of PCM [Conference paper]. *2014 FAA Worldwide Airport Technology Transfer Conference*, Galloway, NJ. https://trid.trb.org/view/1322605

Liston, L. C. (2015). Using mixtures of fatty acid methyl esters as phase change materials for concrete [Master's thesis, Purdue University]. Purdue E-Pubs. https://docs.lib.purdue.edu/open_access_theses/472/

Liston, L. C., Farnam, Y., Krafcik, M., Weiss, J., Erk, K., & Tao, B. Y. (2016). Binary mixtures of fatty acid methyl esters as phase change materials for low temperature applications. *Applied Thermal Engineering*, *96*, 501–507. https://doi.org/10.1016/j.applthermaleng.2015.11.007

Litvan, G. (1972). Phase transitions of adsorbates: IV, mechanism of frost action in hardened cement paste. *Journal of the American Ceramic Society*, *55*(1), 38–42. https://doi.org/10.1111/j.1151-2916.1972.tb13393.x

Litvan, G. (1976), Frost action in cement in the presence of de-icers. *Cement and Concrete Research*, *6*(3), 351–356. https://doi.org/10.1016/0008-8846(76)90097-1

Lockemann, C. A., & Schluender, E. U. (1993). Solid-liquid phase equilibria of mixtures of methyl myristate and methyl palmitate. *Journal of Chemical and Engineering Data*, *38*(3), 432–433. https://doi.org/10.1021/je00011a027

Marangoni, A. (2011, June) *The trouble with crystal polymorphism*. American Oil Chemists' Society (AOCS). https://www.aocs.org/stay-informed/inform-magazine/featured-articles/the-trouble-with-crystal-polymorphism-june-2011?SSO=True

Maximo, G. J., Carareto, N. D. D., Costa, M. C., dos Santos, A. O., Cardoso, L. P., Krähenbühl, M. A., & Meirellles, A. J. A. (2014). On the solid–liquid equilibrium of binary mixtures of fatty alcohols and fatty acids. *Fluid Phase Equilibria*, *366*, 88–98. https://doi.org/10.1016/j.fluid.2014.01.004

Mehta, P. K. & Monteiro, P. J. (2006). *Concrete: Microstructure, properties, and materials* (3rd ed.). McGraw-Hill.

Memon, S. A., Cui, H. Z., Zhang, H., & Xing, F. (2015). Utilization of macro encapsulated phase change materials for the development of thermal energy storage and structural lightweight aggregate concrete. *Applied Energy*, *139*, 43–55. https://doi.org/10.1016/j.apenergy.2014.11.022

Miller, A., Spragg, R., Antico, F., Ashraf, W., Barrett, T., Behnood, A, & Tian, Q. (2014, July 24–26). Determining the moisture content of pre-wetted lightweight aggregate: Assessing the variability of the paper towel and centrifuge methods. *Proceedings of the 4th International Conference on the Durability of Concrete Structures*, Purdue University Libraries Scholarly Publishing Services. 312–316. https://docs.lib.purdue.edu/icdcs/2014/materialscharacterization/4/

Mondal, S. (2008). Phase change materials for smart textiles—an overview. *Applied Thermal Engineering*, *28*(11–12), 1536–1550. https://doi.org/10.1016/j.applthermaleng.2007.08.009

Paterson, W. S. B. (1994). *The physics of glaciers* (3rd ed.). Elsevier.

Pigeon, M., &Pleau, R. (2010). *Durability of concrete in cold climates* (2nd ed.). CRC Press.

Pitzer, K. S., Peiper, J. C., & Busey, R. H. (1984). Thermodynamic properties of aqueous sodium chloride solutions. *Journal of Physical and Chemical Reference Data*, *13*(1), 1–102. https://doi.org/10.1063/1.555709

Powers, T. C. (1945). A working hypothesis for further studies of frost resistance of concrete. *American Concrete Institute*, *41*(1), 245–272. https://doi.org/10.14359/8684

Powers, T. C. (1958). *The physical structure and engineering properties of concrete*. Portland Cement Association.

Powers, T. C., & Willis, T. F. (1950). The air requirement of frost resistant concrete. *Highway Research Board*, *29*,184–211. https://onlinepubs.trb.org/Onlinepubs/hrbproceedings/29/29-010.pdf

Progelhof, R. C., Throne, J. L., & Ruetsch, R. R. (1976). Methods for predicting the thermal conductivity of composite systems: A review. *Polymer Engineering and Science*, *16*(9) 615–625. https://doi.org/10.1002/pen.760160905

Qian, Y., Farnam, Y., & Weiss, J. (2014). Using acoustic emission to quantify freeze-thaw damage of mortar saturated with NaCl solutions. *Proceedings of the 4th International Conference on the Durability of Concrete Structures*, Purdue University Libraries Scholarly Publishing Services, 32–37. https://doi.org.10.5703/1288284315379

Radjy, F. (1968). *A thermodynamic study of the system hardened cement paste and water and its dynamic mechanical response as a function of temperature* (Technical Report No. 90). Stanford University.

Radlinska, A., Rajabipour, F., Bucher, B., Henkensiefken, R., Sant, G., & Weiss, J. (2008). Shrinkage mitigation strategies in cementitious systems: A closer look at differences in sealed and unsealed behavior. *Transportation Research Record: Journal of the Transportation Research Board*, *2070*(1), 59–67. https://doi.org/10.3141/2070-08

Regin, A. F., Solanki, S. C., & Saini, J. S. (2008). Heat transfer characteristics of thermal energy storage system using PCM capsules: A review. *Renewable and Sustainable Energy Reviews*, *12*(9), 2438–2458. https://doi.org/10.1016/j.rser.2007.06.009

Rubinsky, B., & Cravahlo, E. G. (1981). A finite element method for the solution of one-dimensional phase change problems. *International Journal of Heat and Mass Transfer*, *24*(12), 1987–1989. https://doi.org/10.1016/0017-9310(81)90121-6

Sakulich, A.R. & Bentz, D.P. (2012a). Increasing the service life of bridge decks by incorporating phase-change materials to reduce freeze-thaw cycles, *Journal of Materials in Civil Engineering*, *24*(8), 1034–1042. https://doi.org/10.1061/(ASCE)MT.1943-5533.0000381

Sakulich, A. R. & Bentz, D. P. (2012b). Incorporation of phase change materials in cementitious systems via fine lightweight aggregate. *Construction and Building Materials*, *35*, 483–490. https://doi.org/10.1016/j.conbuildmat.2012.04.042

Scherer, G. W. (1999). Crystallization in pores. *Cement and Concrete Research* , 29(8), 1347–1358. https://doi.org/10.1016/S0008-8846(99)00002-2

Schmucki, E., Marty, C., Fierz, C., & Lehning, M. (2014). Evaluation of modelled snow depth and snow water equivalent at three contrasting sites in Switzerland using SNOWPACK simulations driven by different meteorological data input. *Cold Regions Science and Technology*, *99*, 27–37. https://doi.org/10.1016/j.coldregions.2013.12.004

Shamsundar, N., & Sparrow, E. M. (1975). Analysis of multidimensional conduction phase change via the enthalpy model. *Journal of Heat Transfer*, *97*(3), 333-340. https://doi.org/10.1115/1.3450375

Sharma, A., Tyagi, V. V., Chen, C. R., & Buddhi, D. (2009, February 1) Review on thermal energy storage with phase change materials and applications, *Renewable and Sustainable Energy Reviews*, *13*(2) 318–345. https://doi.org/10.1016/j.rser.2007.10.005

Shi, X., Fay, L., Peterson, M. M., & Yang, Y. (2010). Freeze–thaw damage and chemical change of a portland cement concrete in the presence of diluted deicers. *Materials and Structures*, *43*, 933–946. https://doi.org/10.1617/s11527-009-9557-0

Shi, X., Fay, L., Peterson, M. M., Berry, M., and Mooney, M. (2011). A FESEM/EDX investigation into how continuous deicer exposure affects the chemistry of Portland cement concrete. *Construction and Building Materials*, *25*(2), 957–966. https://doi.org/10.1016/j.conbuildmat.2010.06.086

Smith, W. F., & Hashemi, J. (2005). *Foundations of materials science and engineering* (4th ed.). McGraw-Hill.

Sourirajan, S., & Kennedy, G. C. (1962). The system H2O-NaCl at elevated temperatures and pressures. *American Journal of Science*, *260*(2), 115–141. https://doi.org/10.2475/ajs.260.2.115

Spragg, R. P., Castro, J., Li. W., Pour-Ghaz, M., Huang, P. -T., Weiss, J. (2011). Wetting and drying of concrete using aqueous solutions containing deicing salts. *Cement and Concrete Composites*, *33*(5), 535–542. https://doi.org/10.1016/j.cemconcomp.2011.02.009

Stoll, F., Drake, M. L., & Salyer, I. O. (1996). *Use of phase change materials to prevent overnight freezing of bridge decks* (NCHRP-94-ID022). Transportation Research Board. https://onlinepubs.trb.org/onlinepubs/archive/studies/idea/finalreports/highway/NCHRP022_Final_Report.pdf

Sun, Z. & Scherer, G. W. (2010a). Effect of air voids on salt scaling and internal freezing. *Cement and Concrete Research*, *40*(2), 260–270. https://doi.org/10.1016/j.cemconres.2009.09.027

Sun, Z., & Scherer, G. W. (2010b). Pore size and shape in mortar by thermoporometry. *Cement and Concrete Research*, *40*(5), 740–751. https://doi.org/10.1016/j.cemconres.2009.11.011

Sun, Z., & Scherer, G. W. (2010c). Measurement and simulation of dendritic growth of ice in cement paste. *Cement and Concrete Research*, *40*(9), 1393–1402. https://doi.org/10.1016/j.cemconres.2010.03.008

Sutter, L., Peterson, K., Julio-Betancourt, G., Hooton, D., Van Dam, T., and Smith, K. (2008). *The deleterious chemical effects of concentrated deicing solutions on Portland cement concrete* (SD2002-01). South Dakota Department of Transportation. https://pages.mtu.edu/~llsutter/SD_Final/pdf/FINAL_SD2002-01_Literature_Review.pdf

Thomas, L. C, (1993). *Heat transfer*. Prentice Hall.

Touloukian, Y. S . & DeWitt, D. P. (1970) *Thermophysical properties of matter—The TRPC Data Series, Volume 7: Thermal radiative properties: metallic elements and alloys.* IFI/Plenum Data. https://apps.dtic.mil/sti/pdfs/ADA951941.pdf

Tyagi, V. V., Kaushik, S. C., Tyagi, S. K., & Akiyama, T. (2011). Development of phase change materials based microencapsulated technology for buildings: A review. *Renewable and Sustainable Energy Reviews*, *15*(2), 1373–1391. https://doi.org/10.1016/j.rser.2010.10.006

Velraj, R., Seeniraj, R. V., Hafner, B., Faber, C., & Schwarzer, K. (1999). Heat transfer enhancement in a latent heat storage system. *Solar Energy*, *65*(3), 171–180. https://doi.org/10.1016/S0038-092X(98)00128-5

Velraj, R., & Pasupathy, A. V. (2006). Phase change material based thermal storage for energy conservation in building architecture. *International Energy Journal*, *7*(2), 147–159. https://www.researchgate.net/publication/228823294_Phase_Change_Material_based_thermal_storage_for_energy_conservation_in_building_architecture

Villani, C., Farnam, Y., Washington, T., Jain, J., & Weiss, J. (2015). Conventional Portland cement and carbonated calcium silicate-based carbonated cement systems: performance during freezing and thawing in the presence of calcium chloride deicing salts. *Journal of the Transportation Research Board*, *2508*(1). https://doi.org/10.3141/2508-06

Voet, D., Voet, J.G., &Pratt, C.W. (2015). *Fundamentals of biochemistry: life at the molecular level* (4th ed.). Wiley.

Voller, V. R., & Swaminathan, C. R. (1993). Treatment of discontinuous thermal conductivity in control-volume solutions of phase-change problems. *Numerical Heat Transfer, Part B: Fundamentals*, *24*(2), 161–180. https://doi.org/10.1080/10407799308955887

Whiffen, T. R., & Riffat, S. B. (2012). A review of PCM technology for thermal energy storage in the built environment: Part II. *International Journal of Low-Carbon Technologies*, *8*(3), 159–164. https://doi.org/10.1093/ijlct/cts021

Whiting, D. A., & Nagi, M. A. (1998). *Manual on control of air content in concrete*. Portland Cement Association.

Wilding, C. R. (1992). The performance of cement based systems. *Cement and Concrete Research*, *22*(2–3), 299–310. https://doi.org/10.1016/0008-8846(92)90069-8

Williams, R. J. J., & Aldao, C. M. (1983). Thermal conductivity of plastic foams. *Polymer Engineering and Science*, *23*(6), 293–298. https://doi.org/10.1002/pen.760230602

Yang, Z., Weiss, J., & Olek, J. (2006). Water transport in concrete damaged by tensile loading and freeze-thaw cycling. *Journal of Materials in Civil Engineering*, *18*(3), 424–434. https://doi.org/10.1061/(ASCE)0899-1561(2006)18:3(424)

Yoo, J., & Rubinsky, B. (2007). Numerical computation using finite elements for the moving interface in heat transfer problems with phase transformation. *Numerical Heat Transfer*, *6*(20), 209–222. https://doi.org/10.1080/01495728308963083

Young, J. F. (1988). Review of the pore structure of cement paste and concrete and its influence on permeability. *International Concrete Abstracts Portal*, *108*,1–18. https://doi.org/10.14359/2136

Zhang, D., Li, Z., Zhou, J., & Wu, K. (2004). Development of thermal energy storage concrete. *Cement and Concrete Research*, *34*(6), 927–934. https://doi.org/10.1016/j.cemconres.2003.10.022

Zhou, L-P., Wang, B-X., Peng, X-F., Du, X-Z., & Yang, Y-P. (2010), On the specific heat capacity of CuO nanofluid. *Advances in Mechanical Engineering*, *2*, 1–4. https://doi.org/10.1155/2010/172085

Zivkovic, B., & Fujii, I. (2001), An analysis of isothermal phase change of phase change material within rectangular and cylindrical containers. *Solar Energy*, *70*(1) 51–61. https://doi.org/10.1016/S0038-092X(00)00112-2